Technische Universität München
Department Chemie
Lehrstuhl II für Organische Chemie

# Cooperative Pulses
—
## Towards Global Pulse Sequence Optimization

**Michael Braun**

Vollständiger Abdruck der von der Fakultät Chemie der Technischen Universität München zur Erlangung des akademischen Grades eines

**Doktors der Naturwissenschaften**

genehmigten Dissertation

| | |
|---|---|
| Vorsitzender: | Univ.-Prof. Dr. B. Reif |
| Prüfer der Dissertation: | 1. Univ.-Prof. Dr. St. J. Glaser |
| | 2. Univ.-Prof. Dr. K.-O. Hinrichsen |

Die Dissertation wurde am **10.10.2011** bei der Technischen Universität München eingereicht und durch die Fakultät für Chemie am **21.11.2011** angenommen.

# Abstract

The present thesis deals with the concept of cooperative (COOP) pulses that are designed to cancel each other's imperfections and act in a cooperative manner. Multi-scan COOP pulses are applied in several scans and at the same position in a pulse sequence so that undesired signal contributions can be canceled. They complement and generalize phase cycles and difference spectroscopy. We experimentally demonstrate their advantages for broadband and band-selective pulses. Single-scan cooperative ($S^2$-COOP) pulses are applied at different positions of a pulse sequence in a single scan. They can be used to find generalized solutions for common building blocks in NMR spectroscopy. The advantage of the $S^2$-COOP approach is demonstrated in theory and experiment for NOESY-type frequency-labeling blocks. Optimal tracking is a generalization of the gradient ascent pulse engineering (GRAPE) algorithm which allows for the design of pulse sequences that steer the evolution of an ensemble of spin systems such that at defined points in time, a specific trajectory of the density operator is tracked as closely as possible. Optimal tracking has been used for the design of low-power heteronuclear decoupling sequences for *in vivo* applications. Here, we present the theory of cooperative tracking representing a generalization of optimal tracking and multi-scan COOP pulses. Cooperative tracking pulses, multi-scan and single-scan COOP pulses can be efficiently optimized with extended versions of the GRAPE algorithm.

# Zusammenfassung

Die vorliegende Arbeit behandelt das Konzept kooperativer (COOP) Pulse, die dazu ausgelegt sind, ihre Imperfektionen gegenseitig auszugleichen und auf kooperative Weise zu wirken. Multi-Scan COOP Pulse werden in mehreren Scans an der gleichen Stelle einer Pulssequenz eingesetzt, sodass sich unerwünschte Signalbeiträge gegenseitig aufheben können. Sie ergänzen und verallgemeinern Phasenzyklen und Differenzspektroskopie. In Experimenten zeigen wir ihre Vorteile als breitbandige und bandselektive Pulse. Single-Scan-kooperative ($S^2$-COOP) Pulse werden an verschiedenen Positionen einer Pulssequenz in einem Scan eingesetzt. Sie können dazu verwendet werden, um verallgemeinerte Lösungen für gängige Bausteine in der NMR-Spektroskopie zu finden. Vorteile des $S^2$-COOP-Verfahrens werden theoretisch und experimentell anhand NOESY-artiger Evolutionssequenzen aufgezeigt. Optimal Tracking ist eine Verallgemeinerung des *gradient ascent pulse engineering* (GRAPE) Algorithmus', die es ermöglicht, Pulssequenzen zu entwickeln, die die Evolution eines Ensembles von Spinsystemen derart steuern, dass zu bestimmten Zeitpunkten einer spezifischen Trajektorie des Dichteoperators so genau wie möglich gefolgt wird. Mit Optimal Tracking wurden bereits heteronukleare Entkopplungssequenzen mit niedriger Leistung für *in vivo* Anwendungen entwickelt. Hier erläutern wir die Theorie des Cooperative Tracking, einer Verallgemeinerung von Optimal Tracking und multi-scan COOP Pulsen. Cooperative Tracking Pulse, multi-scan und single-scan COOP Pulse können mit erweiterten Versionen des GRAPE-Algorithmus' effizient optimiert werden.

# Eidesstattliche Versicherung

Ich versichere, dass ich die von mir vorgelegte Dissertation selbständig angefertigt, die benutzten Quellen und Hilfsmittel vollständig angegeben und die Stellen der Arbeit, die anderen Werken im Wortlaut oder dem Sinn nach entnommen sind, in jedem Einzelfall als Entlehnung kenntlich gemacht habe; dass diese Dissertation noch keiner anderen Fakultät oder Universität zur Prüfung vorgelegen hat; dass sie – abgesehen von unten angegebenen Teilpublikationen – noch nicht veröffentlicht worden ist sowie, dass ich eine solche Veröffentlichung vor Abschluss des Promotionsverfahrens nicht vornehmen werde. Die Bestimmungen dieser Promotionsordnung sind mir bekannt. Die von mir vorgelegte Dissertation ist von Herrn Prof. Dr. Steffen J. Glaser betreut worden.

**Publikationsliste:**

1. M. Lapert, Y. Zhang, M. Braun, S. J. Glaser, D. Sugny, Singular extremals for the time-optimal control of dissipative spin ½ particles, Phys. Rev. Lett. 104 (2010) 083001.

2. E. Assémat, M. Lapert, Y. Zhang, M. Braun, S. J. Glaser, D. Sugny, Simultaneous time-optimal control of the inversion of two spin ½ particles, Phys. Rev. A 82 (2010) 013415.

3. M. Braun, S. J. Glaser, Cooperative pulses, J. Magn. Reson. 207 (2010) 114-123.

4. M. Lapert, Y. Zhang, M. Braun, S. J. Glaser, D. Sugny, Geometric versus numerical optimal control of a dissipative spin ½ particle, Phys. Rev. A 82 (2010) 063418.

5. Y. Zhang, M. Lapert, D. Sugny, M. Braun, S. J. Glaser, Time-optimal control of spin ½ particles in the presence of radiation damping and relaxation, J. Chem. Phys. 134 (2011) 054103.

6. T. E. Skinner, M. Braun, K. Woelk, N. I. Gershenzon, S. J. Glaser, Design and application of robust rf pulses for toroid cavity NMR spectroscopy, J. Magn. Reson. 209 (2011) 282-290.

# Danksagung

Ich danke Herrn Professor Dr. Steffen J. Glaser dafür, dass er mir die Gelegenheit gab, dieses spannende und ergiebige Thema zu bearbeiten. Als hervorragender Betreuer ist er stets zur Diskussion bereit, vermag zu motivieren wie kein anderer und gewährt die notwendige Freiheit.

Ich danke meinen Eltern, deren unermüdlicher Einsatz mir das Chemiestudium wesentlich erleichtert hat.

Mein besonderer Dank gilt meiner Freundin Anna, die mir immer wieder Kraft, Zuversicht und Liebe schenkt.

Ebenso gilt mein Dank allen Mitgliedern des AK Glaser, die zu vielen bereichernden Erfahrungen beigetragen haben.

Schließlich möchte ich noch all jenen danken, die durch ihren Einsatz die Aufrechterhaltung von Forschung und Lehre ermöglichen.

# Contents

# 1 Introduction

> **Wünschelrute**
> Schläft ein Lied in allen Dingen
> Die da träumen fort und fort
> Und die Welt hebt an zu singen
> Triffst du nur das Zauberwort
>
> Joseph von Eichendorff

In most interpretations of the above poem, its themes are poetry, chant and the magic of speech. An interpretation from a different perspective – thoughts are free – might show how the poetry of nature becomes conceivable by scientific methods. Seen from a very special point of view, it is the nuclear magnetic resonance (NMR) spectroscopist who hits the world (or the nuclear spins in it) with his magic words (or radio-frequency (rf) pulses) upon which a secret tune (free induction decay, FID) can be heard, a tune which hitherto has been fast asleep and now unravels the secrets of the world beyond our senses. Is it not tempting to make the world sing? But as beautiful as it may be, the art of spin manipulation using rf pulses is not free from pitfalls. Undesired side-effects might be bothersome at first. But only when they get bothersome enough to incite us to get rid of them and we are successful in developing a method which lifts the problem will we find – again – beauty and elegance.

As soon as Fourier-transform (FT) NMR was introduced [1], rectangular rf pulses became the central tool in NMR spectroscopy. An rf pulse is called "rectangular" or "square" when its amplitude and phase are constant during the entire pulse duration. Rectangular pulses are simple, their experimental implementation is straightforward and they perform well within a certain parameter range. However, their applicability is limited due to their imperfections. E.g. off-resonance effects are well known [1] and limit the offset range that is covered by a rectangular pulse of finite duration.

In order to compensate for undesired pulse imperfections composite (i.e. with constant amplitudes but variable phases) [2–5] and shaped (i.e. with both phases and amplitudes being varied) [6,7] pulses were developed. Among the class of shaped pulses, adiabatic pulses [7–9] are among the best performing inversion pulses even if they tend to have rather long durations. The ways in which these pulses have been developed often rely on symmetry principles, analytical insights into spin dynamics and intuition. Although many composite and shaped pulses produce very good results, the traditional art of pulse design very likely reached its limits as the complexity of the problems that need to be solved have increased.

Fortunately, pulse design was lifted to a new level with help from optimal control theory [10]. The latter was mainly developed in the course of the United States and Soviet spaceflight programs and found applications in various fields ranging from engineering to economics. In the field of NMR pulse design, optimal control theory forms the foundation of gradient ascent pulse engineering (GRAPE) [11] which is a fast and efficient algorithm for the numerical optimization of shaped rf pulses. With the help of GRAPE, the *art* of pulse design has been transformed into a *science* [12]: GRAPE has made it possible to explore the physical limits of pulse performance [13–15]. Excitation pulses that are robust with respect to offset frequency [16] and rf-field inhomogeneity [17] (or, to some extent, even both [18]) have been developed with an unprecedented quality. In addition, broadband excitation and inversion pulses with restricted rf amplitude [19] or restricted rf power [14], minimized [20] or linear [21] phase dispersion have been presented. Relaxation-optimized excitation pulses have been developed as well [22]. Not only can excitation and inversion pulses representing point-to-point (PP) transformations be designed, but it is possible to find high-quality 90° and 180° universal rotation (UR) [11,17,23] pulses as well. Also, selective pulses with highly complicated excitation patterns that are at the same time dependent on the rf field strength and the offset frequency, so-called pattern pulses, can be designed [24]. GRAPE-designed pulses have become part of the standard software package for Bruker spectrometers TOPSPIN [25]. GRAPE is stretching its arms like an octopus [26] into all related fields: liquid-state NMR [11,13–24] and solid-state NMR [27–29], *in vivo* spectroscopy [30], EPR, quantum information processing [31] and MRI [32], just to name the most important. Recently, the convergence properties of GRAPE have been improved by exploiting second-order information [33, 34] which can be efficiently approximated using the limited-memory Broyden-Fletcher-Goldfarb-Shanno (l-BFGS) quasi-Newton algorithm [35]. (GRAPE is not the only numerical pulse optimization algorithm: so-called Krotov methods [36] can be of comparable performance with respect to GRAPE [34]. Analytical solutions for problems of pulse design have been provided as well but currently they are restricted to special cases [37–42].)

All the above examples represent cases where GRAPE is used to create single and isolated transfers. However, most NMR experiments rely on pulse sequences with many different transfer steps. Stand-alone pulses for the necessary transfers can be designed using GRAPE and replace the former pulses [43]. However, remaining pulse imperfections might accumulate during the sequence and reduce the overall experimental quality despite a good performance of the individual pulses. The problem of error accumulation can be alleviated by several methods. One of them is to keep track of the magnetization during a pulse sequence or a pulse train that is to be optimized: with the so-called optimal tracking algorithm [44], not only a single, isolated transfer or rotation but an arbitrary number of successive transfers can be designed. The advantage of this approach lies in the fact that, for a later transfer, there is no assumption about the initial state it is acting upon. Instead, the initial state of all (but the first) pulses are defined by the outcome of the precedent pulse. Thus, the possible deviations from ideal behavior of a precedent pulse are handed over to the subsequent pulse so that error compensation is possible. If the signal is recorded at the end of a pulse sequence imperfections of individual pulses are irrelevant if these imperfections cancel in the course of the pulse sequence. In addition, the rf amplitudes at a given time slice have an influence on the following trajectory of the density operator and therefore on all following tracking points. This is taken into account by the tracking algorithm: all following tracking points have an influence on the rf parameters of each earlier time slice. Optimal tracking has been successfully applied to the problem of low-power decoupling for *in vivo* applications [44]. However, optimal tracking is not limited to decoupling but can in principle be applied to many different pulse sequences.

Most NMR experiments rely on pulse sequences with many different pulses. In addition, in multi-scan experiments the overall signal is obtained by averaging the signals obtained from each scan. Imperfections in individual scans are irrelevant if these imperfections cancel in the total accumulated signal. Phase cycling [45–48] is routinely used for the suppression of artifacts or unwanted signals: In each scan, a sequence of identical pulses is repeated, except for a systematic phase variation of the pulses (and the receiver). However, it is not only possible to just change the overall phase of a given pulse in subsequent scans, but also to cycle through a set of pulses which can be of any shape. We refer to this class of *coop*eratively acting pulses as COOP pulses [49] which can be efficiently optimized using an adapted version of the GRAPE algorithm. In contrast to the version of the COOP pulse approach where a *single transfer* is optimized by taking advantage of error cancelation between *several scans*, it is – as with optimal tracking – possible to optimize *several transfers* in a *single scan*. We dub this modified COOP approach single-scan COOP ($S^2$-COOP) which makes it possible to further improve the performance of pulse sequences.

So far, the main restriction of GRAPE consisted in the fact that only isolated stand-alone pulses could be optimized. With GRAPE we have been able to find pulses that compensate their own imperfections to a very high degree. With optimal tracking and the concept of cooperative pulses we command two powerful methods that open up a new dimension in pulse sequence design. Now we are able to develop pulses that do not only compensate *their own* but at equal measure *each other's* imperfections, hence act in a cooperative manner.

The present thesis discusses how the properties of COOP pulses can be applied to common problems in NMR spectroscopy:

- **Chapter 2:** COOP pulses in several scans, so-called COOP cycles, are applied at the *same position* in *several scans* and carry out a *single transfer*. Possible applications consist of excitation with minimized phase errors, band-selective excitation and inversion and the suppression of solvent signals.

- **Chapter 3**: COOP pulses in a single scan, so-called $S^2$-COOP pulses, are applied at *different positions* in a *single scan* and carry out *different transfers*. Here, we discuss the optimization of a frequency-labeling block consisting of two pulses separated by a variable delay. Sequences of this kind are needed for various NMR experiments, e.g NOESY [50, 51], INEPT-blocks [52], Ramsey experiments [53] and others.

- **Chapter 4**: We show in theory how the two methods of optimal tracking and COOP pulses for several scans can be combined. The presented method is particularly interesting for the design of heteronuclear decoupling sequences.

The shaped pulses presented in this thesis have been optimized using an extended version of the OCTOPUS optimization software [26] in combination with IPOPT, an implementation of the l-BFGS algorithm [54].

# 2 Multi-scan cooperative pulses

In this chapter, we introduce the concept of cooperative (COOP) pulses which are designed to compensate each other's imperfections. In multi-scan experiments, COOP pulses can cancel undesired signal contributions, complementing and generalizing phase cycles. COOP pulses can be efficiently optimized using an extended version of the optimal control based gradient ascent pulse engineering (GRAPE) algorithm. The advantage of the COOP approach is experimentally demonstrated for broadband and band-selective pulses.

## 2.1 Introduction

In addition to simple rectangular rf pulses with constant amplitudes and phases, composite and shaped pulses [3–6] are powerful tools for the manipulation of spins in modern NMR spectroscopy and imaging. In practice, both composite and shaped pulses are implemented as a sequence of rectangular pulses (with different amplitudes and phases) and in the following, we will use the generic term "pulse" for both composite or shaped pulses. Only recently has it become possible to explore the physical limits of pulse performance [13–15] using methods from optimal control theory [10]. For example, for a given maximum rf amplitude and a desired bandwidth and robustness with respect to rf inhomogeneity, there exists a minimum pulse duration $T^*$ that is required to achieve a desired average fidelity or performance index. It is not possible for a pulse to compensate *its own* imperfections to the desired degree if the pulse duration is shorter than $T^*$. Here, we show that pulse durations can be further reduced by allowing pulses to compensate *each other's* imperfections. We refer to this class of *coop*eratively acting pulses as COOP pulses. In multi-scan experiments, for example, imperfections in individual scans are irrelevant if these imperfections cancel in the total accumulated signal. In many multi-scan experiments, phase cycles [45–48] are routinely used for the suppression of artifacts or unwanted signals: In each scan, a sequence of identical pulses is repeated, except for a systematic phase variation of the pulses (and the receiver). Here, we demonstrate that it is possible to improve the performance of pulse sequences by not only changing the overall phase of a given pulse in subsequent scans, but by cycling through a set of carefully designed COOP pulses which are in general not identical. Highly compensating COOP cycles can be efficiently optimized using an adapted version of the optimal-control-based gradient ascent pulse engineering (GRAPE) algorithm [11,55].

## 2.2 Theory

Before describing the algorithm for the simultaneous optimization of a set of COOP pulses, we briefly review the standard optimal-control based gradient ascent algorithm for the optimization of a single (shaped or composite) pulse.

### 2.2.1 Single pulse optimization

Suppose for a given initial magnetization vector $\boldsymbol{M}(0)$ we want to find a pulse of duration $T$ that optimizes a defined performance index or quality factor $\Phi$, which depends only on the final magnetization vector $\boldsymbol{M}(T)$. In the case of an excitation pulse, for example, we start with $z$ magnetization, i.e. $\boldsymbol{M}(0) = (0,0,1)^\top$, and a simple quality factor could be defined as the $x$ component of the final magnetization [16]. A given pulse is fully characterized by the time-dependent $x$ and $y$ components $\nu_x(t) = -\gamma B_{rf,x}(t)/2\pi$ and $\nu_y(t) = -\gamma B_{rf,y}(t)/2\pi$ (or alternatively by the total rf amplitude $\nu_{rf}(t) = \sqrt{\nu_x^2(t) + \nu_y^2(t)}$ and rf phase $\varphi(t) = \tan^{-1}\{\nu_y(t))/\nu_x(t)\}$).

We can improve the pulse if we know how the quality factor $\Phi$ responds when the controls $\nu_x(t)$ and $\nu_y(t)$ are varied, i.e. if we know the gradients $\delta\Phi/\delta\nu_x(t)$ and $\delta\Phi/\delta\nu_y(t)$. These gradients can be approximated using finite differences.

The same high-dimensional gradients $\delta\Phi/\delta\nu_x(t)$ and $\delta\Phi/\delta\nu_y(t)$ can efficiently be calculated to first order based on principles of optimal control theory [10,11,16,55,56]. This approach requires calculation of the trajectories of the magnetization vector $\boldsymbol{M}(t)$, and of the so-called costate vector $\boldsymbol{\lambda}(t)$, for $0 \leq t \leq T$ [10,11,16,18–20,22,24,55,56]. The desired gradients are approximated to first order by the $x$ and $y$ components of the cross product $\boldsymbol{M}(t) \times \boldsymbol{\lambda}(t)$ [16,19,20]:

$$\frac{\delta\Phi}{\delta\nu_x(t)} = M_y(t)\lambda_z(t) - M_z(t)\lambda_y(t), \tag{2.1}$$

$$\frac{\delta\Phi}{\delta\nu_y(t)} = M_z(t)\lambda_x(t) - M_x(t)\lambda_z(t). \tag{2.2}$$

For a spin with offset $\nu_{off}$, the effective field vector $\nu_e(t)$ is defined as

$$\boldsymbol{\nu}_e(t) = (\nu_x(t), \nu_y(t), \nu_{off})^\top \tag{2.3}$$

and starting from the initial magnetization vector $\boldsymbol{M}(0) = \boldsymbol{M}_i$, the trajectory of the magnetization vector $\boldsymbol{M}(t)$ can be calculated by solving the Bloch equations

$$\dot{\boldsymbol{M}}(t) = 2\pi\boldsymbol{\nu}_e(t) \times \boldsymbol{M}(t). \tag{2.4}$$

Here, for simplicity we assume that relaxation effects can be neglected, however if necessary they can be taken into account in a straightforward way [11,22].

If the pulse performance $\Phi$ depends only on the magnetization vector $\boldsymbol{M}(T)$ at the end of the pulse, the costate vector $\boldsymbol{\lambda}(T)$ is given by $\partial\Phi/\partial\boldsymbol{M}(T)$ [16], i.e. the three components of the costate vector $\boldsymbol{\lambda}(T) = (\lambda_x(T), \lambda_y(T), \lambda_z(T))^\top$ are

$$\lambda_x(T) = \frac{\partial\Phi}{\partial M_x(T)}, \quad \lambda_y(T) = \frac{\partial\Phi}{\partial M_y(T)}, \quad \lambda_z(T) = \frac{\partial\Phi}{\partial M_z(T)}. \tag{2.5}$$

For example, if the quality factor is simply the projection of the final magnetization vector onto a desired target state $\boldsymbol{F}$, i.e.

$$\Phi_a = M_x(T)F_x + M_y(T)F_y + M_z(T)F_z, \tag{2.6}$$

the final costate vector is simply $\boldsymbol{\lambda}(T) = \boldsymbol{F}$ [16]. On the other hand, if the quality to reach a target state $\boldsymbol{F}$ is defined as [20]

$$\Phi_b = 1 - a_1(M_x(T) - F_x)^2 - a_2(M_y(T) - F_y)^2 - a_3(M_z(T) - F_z)^2, \tag{2.7}$$

the resulting final costate vector is given by $\boldsymbol{\lambda}(T) = -(2a_1(M_x - F_x), 2a_2(M_y - F_y), 2a_3(M_z - F_z))^\top$. Here $a_1$, $a_2$ and $a_3$ represent the relative weights given to the desired match of the $x$, $y$, and $z$ components of the magnetization vector and the target state.

The equation of motion for the costate vector has the same form as the Bloch equations (cf. Eq. 2.4) [16,19,20,22], i.e.

$$\dot{\boldsymbol{\lambda}}(t) = 2\pi \boldsymbol{\nu}_e(t) \times \boldsymbol{\lambda}(t), \tag{2.8}$$

and by propagating $\boldsymbol{\lambda}(T)$ backward in time, we obtain $\boldsymbol{\lambda}(t)$ for $0 \leq t \leq T$.

Robustness with respect to offset and rf inhomogeneity can be achieved by averaging the gradients over all offsets $\nu_{off}$ and rf scaling factors $s$ of interest [11,16]. Starting from an initial pulse with rf amplitudes $\nu_x(t)$ and $\nu_y(t)$, the pulse performance can be optimized by following this averaged gradient. In the simplest approach, the gradient information can be used in steepest ascent algorithms, but faster convergence can often be found using conjugate gradient or efficient quasi-Newton methods [54] that are also based on the gradients $\delta\Phi/\delta\nu_x(t)$ and $\delta\Phi/\delta\nu_y(t)$.

### 2.2.2 Optimization of COOP pulses

Now we consider a set of $N$ individual pulses $P^{(j)}$ of duration $T$ with rf amplitudes $\nu_x^{(j)}(t)$ and $\nu_y^{(j)}(t)$ for $j \in \{1, 2, \ldots, N\}$. For a given initial state $\boldsymbol{M}^{(1)}(0) = \boldsymbol{M}^{(2)}(0) = \cdots = \boldsymbol{M}^{(N)}(0) = \boldsymbol{M}_i$, the corresponding $N$ trajectories $\boldsymbol{M}^{(j)}(t)$ of the magnetization vectors under the pulses $P^{(j)}$ can be calculated for $0 \leq t \leq T$ using the Bloch equations. If the quality factor $\Phi$ depends only on the final magnetization vectors $\boldsymbol{M}^{(j)}(T)$, the components of the costate vectors $\boldsymbol{\lambda}^{(j)}(T)$ are given by

$$\lambda_x^{(j)}(T) = \frac{\partial\Phi}{\partial M_x^{(j)}(T)}, \quad \lambda_y^{(j)}(T) = \frac{\partial\Phi}{\partial M_y^{(j)}(T)}, \quad \lambda_z^{(j)}(T) = \frac{\partial\Phi}{\partial M_z^{(j)}(T)} \tag{2.9}$$

and the $N$ trajectories $\boldsymbol{\lambda}^{(j)}(t)$ can be calculated for $0 \leq t \leq T$ using the equation of motion of the costate vectors in analogy to Eq. 2.8. The gradient of the quality factor $\Phi$ with respect to the controls $\nu_x^{(j)}(t)$ and $\nu_y^{(j)}(t)$ is given by the $x$ and $y$ components of the vectors $\boldsymbol{M}^{(j)}(t) \times \boldsymbol{\lambda}^{(j)}(t)$

[16]:

$$\frac{\delta\Phi}{\delta v_x^{(j)}(t)} = M_y^{(j)}(t)\lambda_z^{(j)}(t) - M_z^{(j)}(t)\lambda_y^{(j)}(t), \tag{2.10}$$

$$\frac{\delta\Phi}{\delta v_y^{(j)}(t)} = M_z^{(j)}(t)\lambda_x^{(j)}(t) - M_x^{(j)}(t)\lambda_z^{(j)}(t). \tag{2.11}$$

For example, consider the optimization of COOP excitation pulses with minimal overall phase error. If applied in successive scans, the real and imaginary parts of the accumulated signal $S_x+\mathrm{i}S_y$ are proportional to the $x$ and $y$ components of the average magnetization vector

$$\overline{\boldsymbol{M}}(T) = \frac{1}{N}\sum_{j=1}^{N}\boldsymbol{M}^{(j)}(T). \tag{2.12}$$

The goal is to maximize $\overline{M}_x(T)$ and to minimize $\overline{M}_y(T)$ in order to minimize the phase error of the accumulated signal, while $\overline{M}_z(T)$ is irrelevant. This goal can be quantified by

$$\Phi_c = 1 - (1-\overline{M}_x(T))^2 - a\,\overline{M}_y(T)^2, \tag{2.13}$$

which is a generalization of the quality factor $\Phi_b$ (cf. Eq. 2.7), where $\boldsymbol{M}(T)$ is replaced by $\overline{\boldsymbol{M}}(T)$, with $\boldsymbol{F} = (1,0,0)^\top$, $a_1 = 1$, $a_2 = a$, and $a_3 = 0$. Here, the relative weight given to the deviation of $\overline{M}_x$ and $\overline{M}_y$ from the target values $F_x = 1$ and $F_y = 0$ can be adjusted by the parameter $a$. According to Eq. 2.9, the costate vectors $\boldsymbol{\lambda}^{(j)}(T)$ are given by

$$\boldsymbol{\lambda}^{(j)}(T) = \frac{2}{N}(1-\overline{M}_x(T), -a\,\overline{M}_y(T), 0)^\top, \tag{2.14}$$

which is independent of $j$, i.e. all costate vectors are identical at the end of the pulse ($\boldsymbol{\lambda}^{(1)}(T) = \boldsymbol{\lambda}^{(2)}(T) = \cdots = \boldsymbol{\lambda}^{(N)}(T)$) and depend on the average magnetization vector $\overline{\boldsymbol{M}}(T)$. However, the back propagation of the costates under the different pulses $P^{(j)}$ results in different trajectories $\boldsymbol{\lambda}^{(j)}(t)$ for $0 \le t < T$.

With the trajectories $\boldsymbol{M}^{(j)}(t)$ and $\boldsymbol{\lambda}^{(j)}(t)$, the gradients (Eqs. 2.10, 2.11) can be efficiently calculated, providing a powerful means for the simultaneous optimization of a set of mutually compensating COOP pulses. In the following, illustrative examples will be given to demonstrate the COOP approach. Experiments were performed on Bruker AV 250 and AV III 600 spectrometers using a sample of $\approx$ 1% $H_2O$ in $D_2O$ doped with copper sulfate.

## 2.3 Examples

### 2.3.1 Total elimination of magnetization

As a first illustrative example, we consider the problem of completely eliminating *all* components of the average magnetization vector, i.e. $\overline{M}_x = \overline{M}_y = \overline{M}_z = 0$ in the absence of $B_0$ gradients, $B_1$ inhomogeneity and relaxation effects, starting from $z$ magnetization. Clearly, this cannot be accomplished by a single pulse and at least two scans are required to achieve this goal. We optimized COOP cycles consisting of two or three individual pulses, using the quality factor

$$\Phi_{elim} = 1 - \overline{M}_x(T)^2 - \overline{M}_y(T)^2 - \overline{M}_z(T)^2. \tag{2.15}$$

For the simplest case of a single spin on resonance, the extended GRAPE algorithm finds the intuitive solution of two rectangular 90° pulses with a relative phase-shift of 180°. Similarly, the optimization of a three-step COOP cycle yields three 90° pulses with phase differences of 120° and 240° as expected (data not shown), demonstrating that the algorithm is able to "rediscover" simple phase cycles. If the elimination of magnetization is desired not only for the on-resonance case but for a finite range of offsets and limited rf amplitudes, the optimal solution is not clear *a priori*. For an offset range of $\pm 10$ kHz and a maximum rf amplitude of 10 kHz we optimized a two-step COOP cycle, consisting of two individual pulses with a duration of 50 $\mu$s each. For each individual pulse a different random pulse shape was created at the start of the optimization and no symmetry constraints were imposed. Fig. 2.1 shows the optimized pulse shapes, the final magnetization components after each individual pulse and the components of the average final magnetization vector as a function of offset. The two-step COOP cycle efficiently eliminates the average magnetization vector as expected. Here, the optimal solution consists of two saturation pulses that are identical up to an overall phase shift of 180°. Each individual saturation pulse brings the magnetization vector to the transverse plane and hence eliminates the $z$ component in each scan with high fidelity for the desired range of offsets. The remaining transverse magnetization components are then averaged to zero by repeating the saturation pulse with a phase shift of 180°. This solution is not unexpected and a single saturation pulse could have been optimized and phase cycled with the same result. However, initially it was by no means clear if this is in fact the best possible strategy. As the COOP approach is not limited to a restricted set of solutions (e.g. pairs of saturation pulses), it is also able to find unexpected solutions if they exist, as will be shown in the next examples.

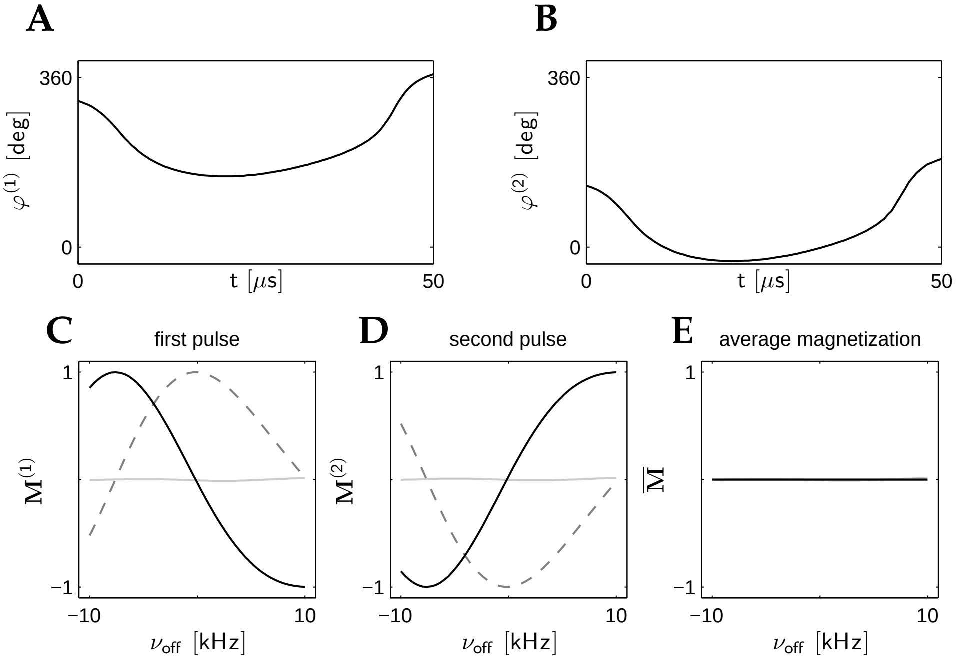

Figure 2.1: Two-step COOP cycle for the complete elimination of the average magnetization vector $\overline{\boldsymbol{M}}$ for offsets in the range of ±10 kHz for a constant rf amplitude $\nu_{rf} = 10$ kHz and a pulse duration of 50 $\mu$s. A and B show the phase modulations $\varphi^{(1)}(t)$ and $\varphi^{(2)}(t)$, simulated offset-profiles of $\boldsymbol{M}^{(1)}(T)$, $\boldsymbol{M}^{(2)}(T)$ and $\overline{\boldsymbol{M}}(T)$ are drawn in C, D and E. The $x$, $y$ and $z$ components are plotted as solid black, dashed gray and solid gray curves, respectively.

### 2.3.2 Band-selective excitation pulses

As a second example, we consider band-selective COOP pulses that excite magnetization in a defined offset range and simultaneously eliminate the average magnetization vector in other offset ranges. We use the quality factor $\Phi_b$ (Eq. 2.7) for various offset-dependent target states $\boldsymbol{F}(\nu_{off})$. Here we consider the example where $\boldsymbol{F}(\nu_{off}) = (1,0,0)^\top$ for $|\nu_{off}| \leq$ 2 kHz (the "pass band") and $\boldsymbol{F}(\nu_{off}) = (0,0,0)^\top$ for 2 kHz $< |\nu_{off}| \leq$ 10 kHz (the "stop band") . The pulse duration $T$ and the maximum rf amplitude $\nu_{rf}^{max}$ were set to 500 $\mu s$ and 10 kHz, respectively. In contrast to the first example, in this case the COOP optimization yields two different pulses that are not simply related by an overall phase shift (Fig. 2.2). Figure 2.2 also shows the simulated and experimental final magnetization components created by the individual pulses and the average magnetization vector. While the response of the individual COOP pulses appears to be erratic, the cancelation of the undesired terms is almost perfect. An excellent match is found between experimental (gray) and simulated (black) data.

For comparison, Fig. 2.3 shows the results of a conventional approach based on two individually optimized pulses: a broadband pulse with a target state $\boldsymbol{F}_1(\nu_{off}) = (1,0,0)^\top$ for $|\nu_{off}| \leq$ 10 kHz and a band-selective pulse with $\boldsymbol{F}_2(\nu_{off}) = (1,0,0)^\top$ for $|\nu_{off}| \leq$ 2 kHz and $\boldsymbol{F}_2(\nu_{off}) = (-1,0,0)^\top$ for 2 kHz $< |\nu_{off}| \leq$ 10 kHz. These pulses also yield the desired average magnetization profile. Very good suppression of the $x$ component is achieved by this approach in the stop band. However, large residual $y$ and $z$ components of the average magnetization vector of more than 40% remain in the vicinity of the transition regions at ±2 kHz (see Fig. 2.3). In contrast, using the the COOP approach, the undesired $y$ and $z$ components can be almost completely suppressed in the pass band, the stop band as well as in the transition region (cf. Fig. 2.2).

Similar results were found for band-selective inversion pulses and different ranges of pass and stop bands (data not shown). It is interesting to note that in the case of band-selective inversion (and complete elimination of the average magnetization vector in the stop band), the COOP approach resulted in two very similar pulses with a relative phase shift of 180°. In this case, the target profile of the average magnetization vector can be approached by a pulse that inverts the magnetization in the pass band and brings it into the transverse plane in the stop band. By repeating the pulse with a phase shift of 180°, all transverse magnetization components are perfectly canceled. Hence in this case, the COOP approach yields a solution that could also be constructed using a conventional optimization of a single pulse combined with a phase cycle.

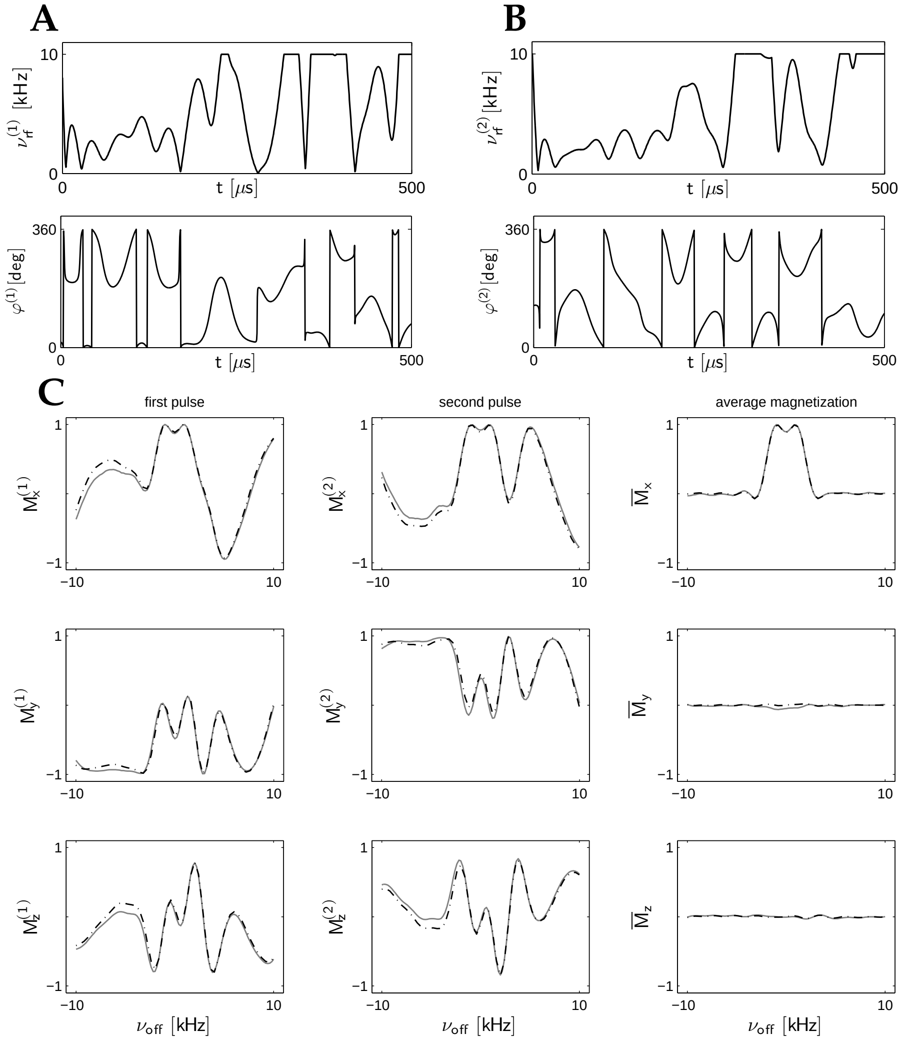

Figure 2.2: Two-step COOP cycle for band-selective excitation and saturation. The rf amplitudes $\nu_{rf}^{(j)}(t)$ and phases $\varphi^{(j)}(t)$ for the two COOP pulses are shown in A and B. Simulated (black, dash-dotted curves) and experimental (gray, solid curves) components of $\boldsymbol{M}^{(1)}(T)$, $\boldsymbol{M}^{(2)}(T)$ and $\overline{\boldsymbol{M}}(T)$ are shown in C.

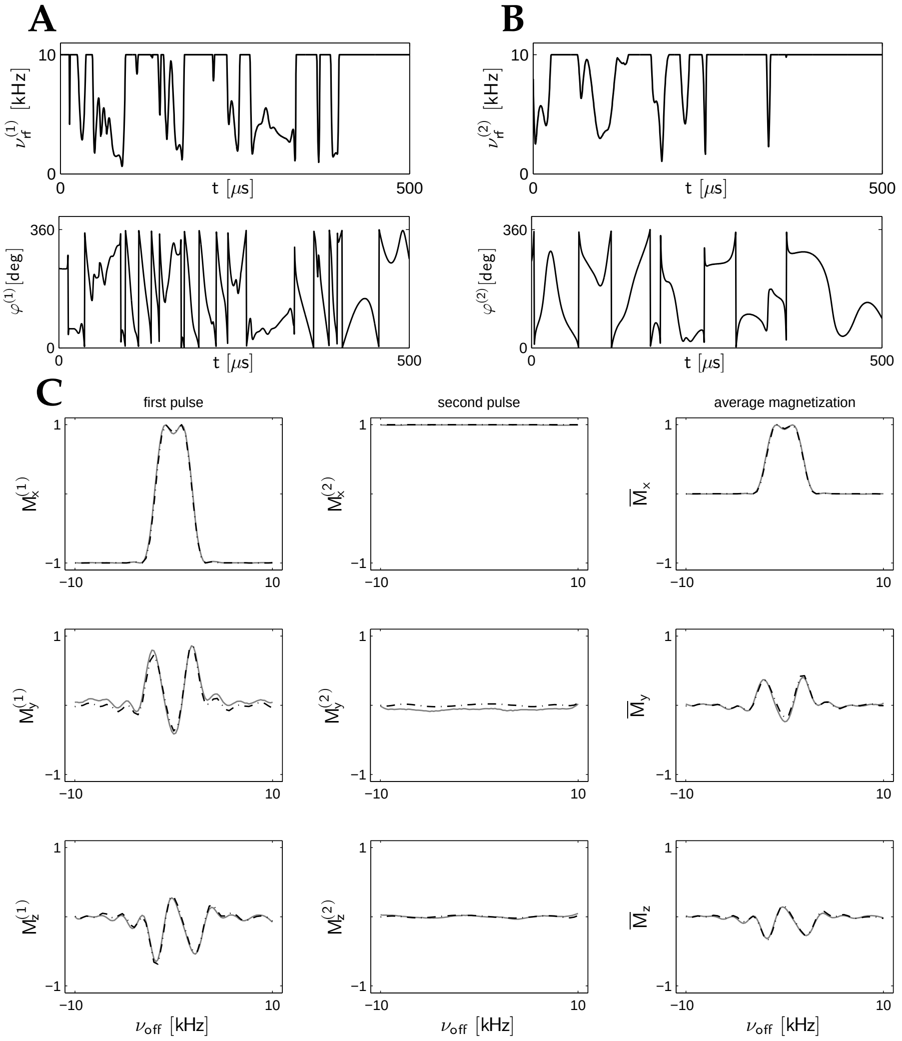

Figure 2.3: Two conventional pulses that were independently optimized for band-selective and broadband excitation, respectively. The rf amplitudes $\nu_{rf}(t)$ and phases $\varphi(t)$ for each individual pulse are shown in A and B. Simulated (black, dash-dotted curves) and experimental (gray, solid curves) components of $\boldsymbol{M}^{(1)}(T)$, $\boldsymbol{M}^{(2)}(T)$ and $\overline{\boldsymbol{M}}(T)$ are shown in C.

However, it was by no means obvious before that this approach yields the optimal solution, which is in fact very different from the naive approach of combining individually optimized pulses for band-selective and broadband inversion.

### 2.3.3 Broadband excitation of $x$ magnetization with minimum phase error

Here we ask the question of whether the duration of broadband excitation pulses can be reduced using the COOP approach. In order to avoid phase errors in the resulting spectrum, a single pulse for broadband excitation of $x$ magnetization is not allowed to create significant $y$ components in the desired offset range. In contrast, the creation of relatively large $y$ components $|M_y^{(j)}(T)|$ by the individual members of a cycle of COOP excitation pulses is acceptable, provided $|\overline{M}_y(T)|$ is small (and $\overline{M}_x(T)$ is large). This provides additional degrees of freedom in the optimization.

As a concrete example, we consider the optimal excitation of $x$ magnetization with minimal phase errors in an offset range of ±20 kHz with a maximum rf amplitude of $\nu_{rf}^{max} = 17.5$ kHz [16,19,20] and a robustness with respect to variations of the rf amplitude of ±5%. For this problem, the duration of efficient optimal control based pulses could be reduced from 2 ms [16] to 500 $\mu$s [19] by generalizing the algorithm to take rf limit limits into account during the optimization. Subsequently, the pulse duration could be reduced even further to only 125 $\mu$s [20] by using a quality factor similar to $\Phi_c$ (Eq. 2.13) for $N = 1$ that is better adapted to the problem of excitation with minimal phase errors than quality factors based on $\Phi_a$ (Eq. 2.6).

For the same specifications, we optimized a single pulse ($N = 1$) and COOP cycles ($N > 1$) using the quality factor $\Phi_c$ (Eq. 2.13). The numerically determined quality factor $\Phi_c$ (Eq. 2.13 with $a = 1$) of the single 125 $\mu$s long pulse from [20] is $\Phi_c$ =0.999852. The gradient of the quality factor for the COOP pulse optimization can be efficiently approximated to first order using Eqs. 2.10 – 2.11, where $\lambda^{(j)}(T)$ is given by Eq. 2.14. For example, for a three-step COOP cycle, a comparable quality factor ($\Phi_c = 0.999856$) can be achieved with a reduced duration of only 100 $\mu$s of each individual pulse. Hence, in this case it is possible to reduce the duration of excitation pulses by an additional 20% without loss in pulse performance using the COOP approach. The $x$ component of the excited average magnetization vector is about 0.99, and the phase error is less than 0.4° for the entire offset range of 40 kHz.

In order to explore the performance limit of even shorter pulses, we also optimized single and COOP pulses with a duration of $T = 50\ \mu$s, which is only 3.5 times longer than the duration of a hard 90° pulse for an rf amplitude of 17.5 kHz. Fig. 2.4 shows the achieved quality factors for a single pulse ($N = 1$) and for COOP cycles with $N$ between 2 and 6. The optimized pulses for $N = 1$, 2, and 3 are shown in Fig. 2.5. All pulses have constant amplitude, taking full advantage of the maximum allowed rf amplitude of $\nu_{rf}^{max}$ =17.5 kHz. The optimal single pulse ($N = 1$) shown in Fig. 2.5 A is purely phase-alternating with phases $\pm\pi/2$. This class of phase-alternating pulses implies the following symmetry relations for the $x$ and $y$ components of the excited magnetization vectors at offsets $\pm\nu$ [4]:

$$M_x(\nu) = M_x(-\nu), \tag{2.16}$$

$$M_y(\nu) = -M_y(-\nu). \tag{2.17}$$

(In additon, $M_z(\nu) = M_z(-\nu)$, however, this is not relevant here, as $\Phi_c$ has no explicit $M_z$ dependence, cf. Eq. 2.13.) The symmetry relations for the $x$ and the $y$ components of the final magnetization vectors match the symmetry of the problem: Maximum $M_x(\nu)$ is desired both for positive offsets (between 0 and 20 kHz) and for negative offsets (between 0 and $-20$ kHz), and, according to Eq. 2.16, a large $M_x(\nu)$ implies an equally large $M_x(-\nu)$. In addition, $|M_y|(\nu) \approx 0$ is desired both for positive and negative offsets, and, according to Eq. 2.17, a small $|M_y|(\nu)$ at frequency $\nu$ implies an equally small $|M_y|(-\nu)$.

In contrast to the case $N = 1$, the individual COOP pulses for $N = 2$ shown in Fig. 2.5 B are not phase-alternating but have smooth phase modulations. However, the phase modulations are not independent but are related by phase inversion and an additional phase shift by $\pi$:

$$\varphi^{(2)}(t) = -\varphi^{(1)}(t) + \pi, \tag{2.18}$$

corresponding to a reflection of the phase around $\pi/2$. (In terms of the $x$ and $y$ components of the rf amplitudes, this relation corresponds to

$\nu_x^{(2)} = -\nu_x^{(1)}$ and $\nu_y^{(2)} = \nu_y^{(1)}$.) Applying well-known principles of pulse sequence analysis [4], it is straightforward to show that Eq. 2.18 implies the following symmetry relations between the transverse components of the excited magnetization vectors after the first and second pulse:

$$M_x^{(2)}(\nu) = M_x^{(1)}(-\nu), \tag{2.19}$$

$$M_y^{(2)}(\nu) = -M_y^{(1)}(-\nu) \tag{2.20}$$

(and in addition $M_z^{(2)}(\nu) = M_z^{(1)}(-\nu)$). As a direct consequence of Eqs. 2.19 and 2.20, the transverse components of the average magnetization vector after the two-step COOP cycle are related by

$$\overline{M}_x(\nu) = \overline{M}_x(-\nu), \tag{2.21}$$

$$\overline{M}_y(\nu) = -\overline{M}_y(-\nu). \tag{2.22}$$

which is analogous to the relations in Eqs. 2.16 and 2.17 for a single phase-alternating pulse and which matches the symmetry of the problem as discussed above. The symmetry relations for the average transverse magnetization components (Eqs. 2.21 and 2.22) can always be realized if the $N$-step COOP cycle consists of symmetry-related pulse pairs (with phase relations corresponding to Eq. 2.18) and/or phase-alternating pulses with phases $\pm\pi/2$. For example, the three-step COOP cycle consists of one symmetry-related pulse pair and one phase-alternating pulse (see Fig. 2.5 C). For $N = 4$, 5, and 6, we always find two symmetry-related pulse pairs and an according number of phase-alternating pulses.

Fig. 2.6 shows the location of the individual and of the average magnetization vectors in the $y$-$z$ plane after the three-step COOP cycle ($N = 3$) (cf. Fig. 2.5 C). The points denoted a, b, and c correspond to offsets of $-20$ kHz, 0 kHz and 20 kHz, respectively. Figs. 2.6 B and C illustrate the symmetry relations of Eqs. 2.16, 2.17 and of Eqs. 2.21, 2.22. Relatively large $y$ components of up to 40% are found for each individual pulse, illustrating the additional degrees of freedom gained by the COOP approach. However, the average magnetization vectors are located very close to the $x$-$z$ plane as shown in Fig. 2.6 E. In Fig. 2.6 F, the corners of the triangles represent the locations of the magnetization vectors after the individual pulses and the centers of the triangles indicate the location of the average magnetization vectors for offsets −20 kHz (a), 0 kHz (b) and 20 kHz (c), illustrating the averaging process. For comparison, Fig. 2.6 D also displays the location of the magnetization after the optimized single pulse (cf. Fig. 2.5 A).

A good match is found between the simulated and experimental performance of the COOP pulses, as demonstrated in Fig. 7, where the $x$ component and the phase of the average magnetization vector is shown for the optimized single pulse and for the COOP cycles with $N = 3$ and $N = 6$. For the single pulse, the excitation efficiency is below 92% for a large range of offsets, whereas for $N = 6$, the excitation efficiency approaches 95% for almost the entire offset range. At the same time, the largest phase error is reduced from about 8° to 5° at the extreme offsets and from about 3° to less than 1.3° for offsets between ±18 kHz.

In [20] we conjectured that for a single pulse a duration of 100 $\mu$s is a conservative lower limit for achieving better than 95% excitation efficiency and a phase error of no more than 4° in a relative bandwidth of $\Delta\nu_{off}/\nu_{rf}^{max} = 2.3$ and with rf tolerance of ±5%. With the COOP approach, we were able to push the lower limit on pulse length below 65 $\mu$s for $N = 6$ (data not shown).

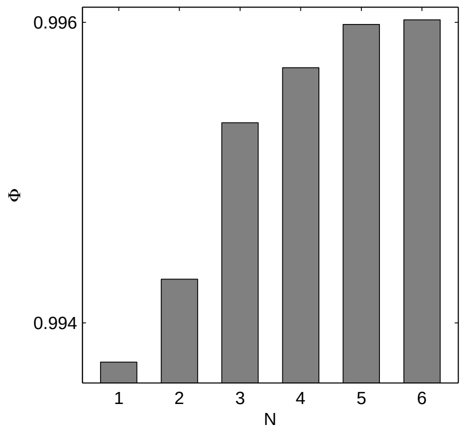

Figure 2.4: Quality factor $\Phi$ for excitation of $x$ magnetization with pulse durations of $T = 50$ $\mu$s as function of the number of COOP pulses $N$.

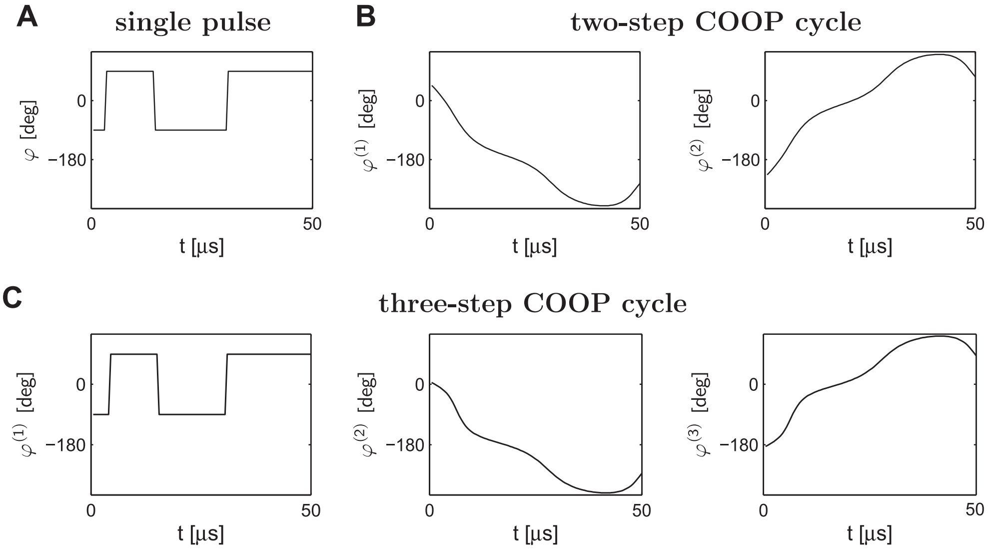

Figure 2.5: Excitation pulses with minimized phase errors with a duration of $T = 50$ $\mu$s: (A) conventional single pulse, (B) two-step COOP cycle ($N = 2$), (C) three-step COOP cycle ($N = 3$). For both pulse pairs with "smooth" phase modulation in B and C, the individual pulses are symmetry-related by $\varphi^{(j+1)}(t) = -\varphi^{(j)}(t) - \pi$ which is equivalent to Eq. 2.18.

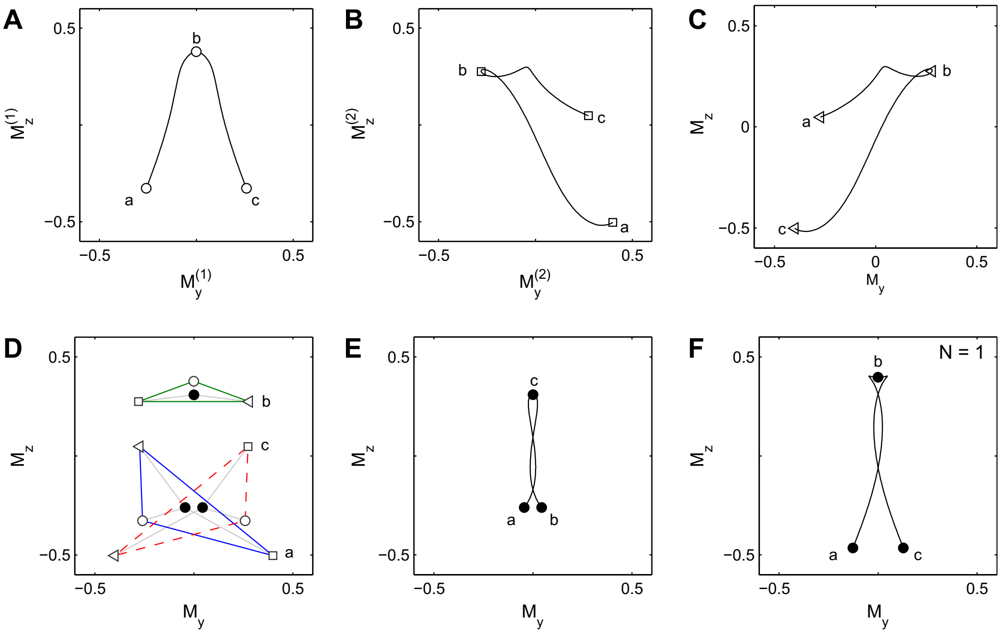

Figure 2.6: In A - C, the individual offset-profiles for a three-step COOP cycle ($N$ = 3) from Fig. 2.5 C are shown. The final states of $M_y^{(j)}(T)$ and $M_z^{(j)}(T)$ within an offset frequency range of ±20 kHz are displayed, where in each subplot, the offsets −20 kHz, 0 kHz and 20 kHz are indicated by symbols (open circles, squares and triangles) denoted a,b and c, respectively. For these three offsets, the $y$ and $z$ components of $\boldsymbol{M}^{(1)}(T)$, $\boldsymbol{M}^{(2)}(T)$ and $\boldsymbol{M}^{(3)}(T)$ (open symbols) and of $\overline{\boldsymbol{M}}(T)$ (solid discs) are shown in D, illustrating the cancelation of phase errors. Subplot E shows the location of the average magnetization vector $\overline{\boldsymbol{M}}(T)$ for the entire offset range of ±20 kHz. For comparison, the location of the magnetization vector $\boldsymbol{M}(T)$ for the single, conventionally optimized pulse ($N$ = 1, cf. Fig. 2.5 A) is shown in F.

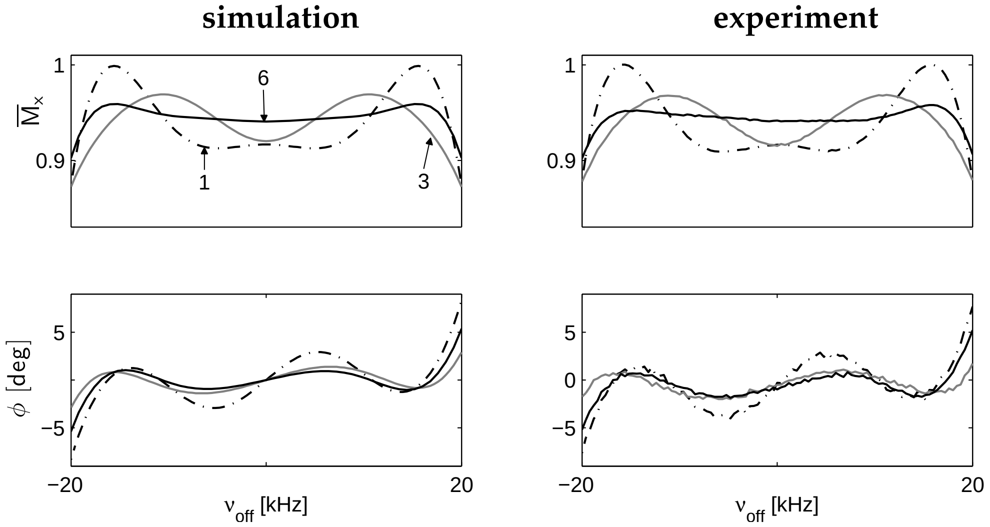

Figure 2.7: Simulated and experimental offset profiles for the average magnetization $\overline{M}_x(T)$ and the phase error $\phi(T)$ for a single pulse ($N = 1$, cf. Fig. 2.5 A) and COOP cycles with $N = 3$ (cf. Fig. 2.5 C) and $N = 6$.

### 2.3.4 Broadband excitation with linear offset dependence of phase

In the previous section the target was to create pulses with offset independent phase, i.e. pulses where no phase correction of first or higher order is necessary. As shown in [21], an even larger bandwidth can be achieved for so-called ICEBERG pulses that create transverse magnetization with a linear offset dependence of the phase. For example, for a simple rectangular 90° pulse, the resulting phase is almost linear for a large range of offsets and can be corrected by first-order phase correction. Fig. 2.8 shows the offset profile of the $x$ component of $\boldsymbol{M}_x(T)$ magnetization and the residual phase error after first-order phase correction with 2.9°/kHz for a rectangular 14.29 $\mu$s 90° pulse, corresponding to an rf amplitude of $\nu_{rf} = 17.5$ kHz. Over a range of ±50 kHz, the phase error is less than about 5°. However, for offset frequencies beyond ±30 kHz the excitation efficiency decreases rapidly.

We optimized a single pulse and a two-step COOP cycle ($N = 2$) with a duration of 60 $\mu$s each, a maximum rf amplitude 17.5 kHz, 5% rf inhomogeneity for a bandwidth of ±50 kHz allowing for the same first order phase correction of 2.9°/kHz as for the simple rectangular pulse. Simulated and experimental results are displayed in Fig. 2.8. The performance of the optimized single pulse is significantly better than the performance of the simple rectangular pulse with larger transverse magnetization of more than 90% (except for offsets near −50 kHz where the efficiency drops to about 80%) compared to 45% and comparable phase errors. However, the performance of the optimized COOP pulses shows a significant further improvement with an excitation efficiency of more than than 95% and phase errors of less than 2.4° over the entire offset range of ±50 kHz.

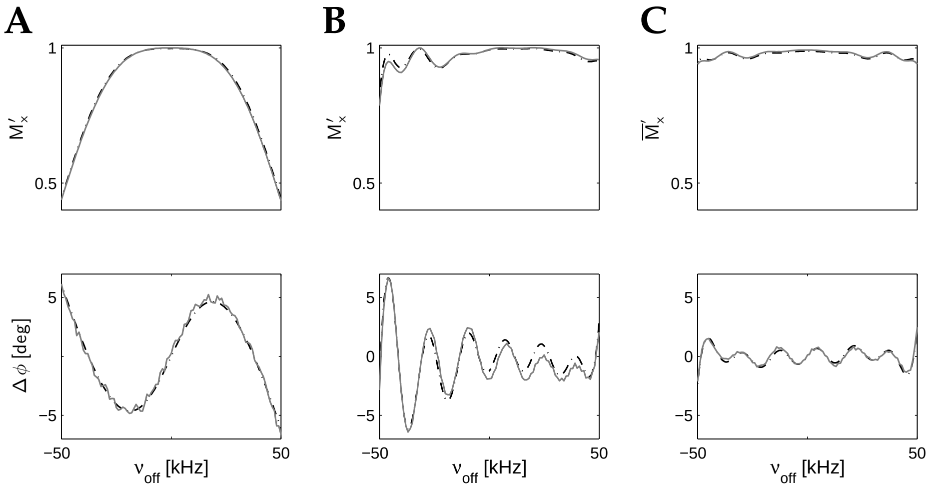

Figure 2.8: Offset profiles for $\overline{M}'_x$ and phase deviation $\Delta\phi$ for a single rectangular pulse (A), an optimized individual ICEBERG pulse [21] with $N = 1$ (B, cf. dash-dotted curve in Fig. 2.9) and a two-step COOP cycle ($N = 2$) (C, cf. solid curves in Fig. 2.9). $\overline{M}'_x$ is the $x$ component of $\overline{\boldsymbol{M}}(T)$ and $\Delta\phi$ is the residual phase error after a first-order phase correction of 2.9°/kHz. Solid gray and dash-dotted black curves represent experimental and simulated data.

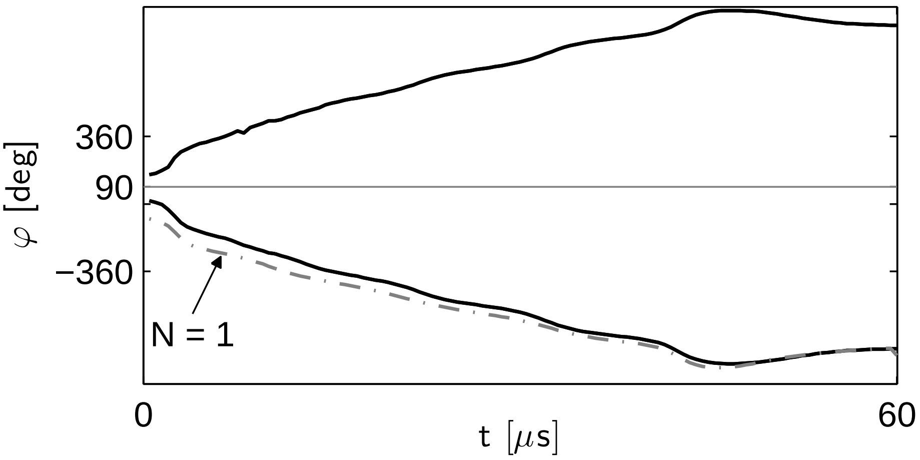

Figure 2.9: A single (dash-dotted gray curve) ICEBERG and a two-step ($N = 2$) COOP ICEBERG cycle (solid black curves). For the COOP pulse pair the symmetry relation from Eq. 2.18 is approximately fulfilled.

### 2.3.5 COOP WET pulses

The final example demonstrating the power of the COOP approach is motivated by the WET (water suppression enhanced through $T_1$ effects) solvent suppression sequence [57, 58]. In order to also suppress solvent signals in regions away from the center of the rf coil and therefore experiencing smaller rf amplitudes, pulses are required that act as broadband 90° pulses for the full rf amplitude but that do not excite the solvent signal in regions of the sample where the rf amplitude is significantly scaled down. One solution is based on a composite pulse, such as the $90^\circ_x 90^\circ_y 90^\circ_{-x} 90^\circ_{-y}$ pulse [58, 59], which is applied in every scan. However, in multi-scan experiments, improved performance was found if in three out of four scans a simple rectangular $90^\circ_x$ pulse is used and in one out of four scans a simple rectangular $270^\circ_{-x}$ pulse [58]. This set of four pulses ($90^\circ_x$, $90^\circ_x$, $90^\circ_x$, $270^\circ_{-x}$), which are applied in successive scans, was derived in [58] based on linear response theory, which however is strictly valid only for flip angles approaching zero. In contrast, the COOP approach introduced here allows us to develop an optimized cycle of COOP pulses for this task, taking into account the full non-linear spins dynamics.

To illustrate this, we optimized COOP pulses with an excitation pattern [24] as a function of offset $\nu_{off}$ and rf scaling factor $s$ that is adapted to the problem (see Fig. 2.10). For rf scaling factors in the range $0.95 \leq s \leq 1.05$, the goal is to excite $x$ magnetization in an offset range of ±5 kHz with minimal phase error. For rf scaling factors in the range $0 \leq s \leq 0.6$, the goal is to minimize the transverse component $\overline{M}_\perp = (\overline{M}_x^2 + \overline{M}_y^2)^{1/2}$ of the average magnetization vector for a reduced range of offset (near the solvent resonance) of ±500 Hz. We assume initial $z$ magnetization and a maximum nominal rf amplitude of $\nu_{rf}^{max} = 20$ kHz.

Fig 2.10 and 2.11 show the performance of an optimized two-step COOP cycle ($N = 2$) with a duration T = 200 $\mu$s for each of the two individual COOP pulses. For comparison, we also show the performance of the composite pulse $90^\circ_x 90^\circ_y 90^\circ_{-x} 90^\circ_{-y}$ [59], of a sequence based on ($90^\circ_x$, $90^\circ_x$, $90^\circ_x$, $270^\circ_{-x}$) [58] and an optimized individual pulse ($N = 1$).

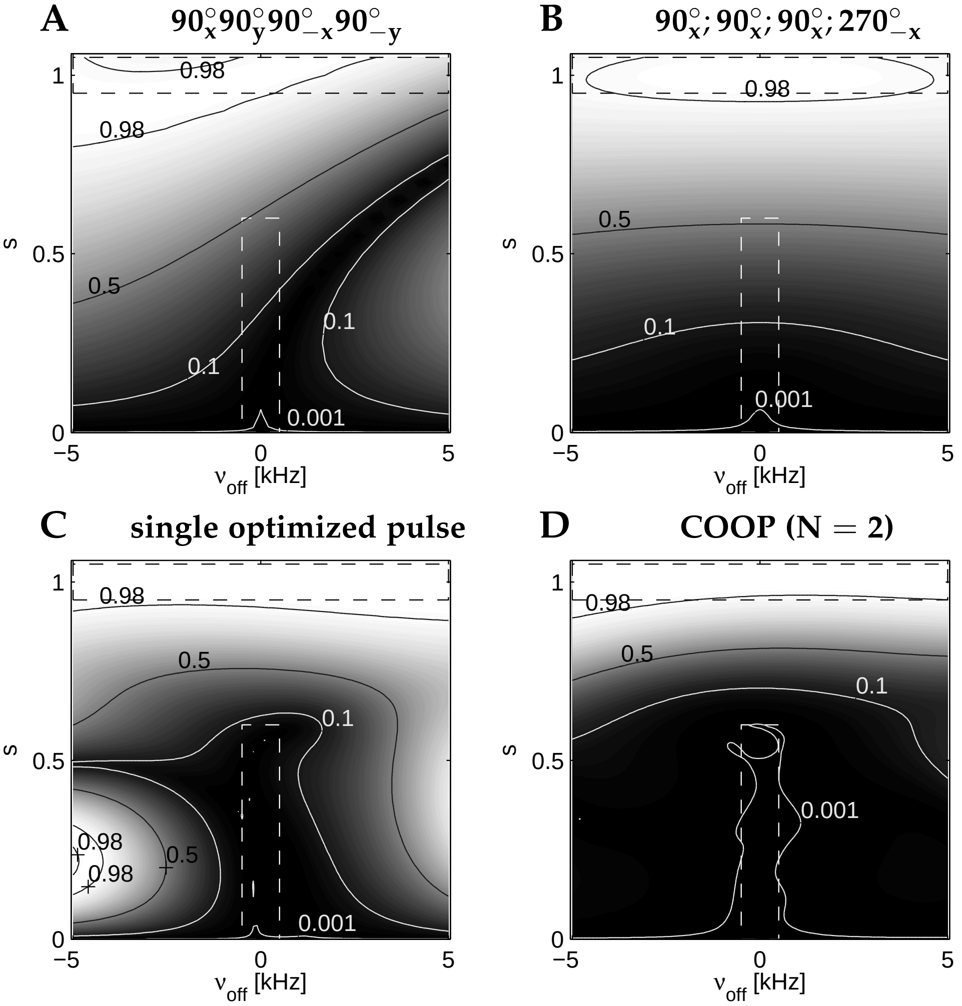

Figure 2.10: Comparison of the average transverse magnetization as a function of offset $\nu_{off}$ and rf scaling $s$ for a two-step cycle of COOP WET pulses (D, $N = 2$) with the $90^\circ_x 90^\circ_y 90^\circ_{-x} 90^\circ_{-y}$ composite pulse (A, [59]), the four-scan sequence based on $90^\circ_x; 90^\circ_x; 90^\circ_x; 270^\circ_{-x}$ (B, [58]) and an optimized individual pulse (C, $N = 1$). The areas for which optimal excitation and optimal suppression of transverse magnetization are desired are indicated by black and white dashed rectangles.

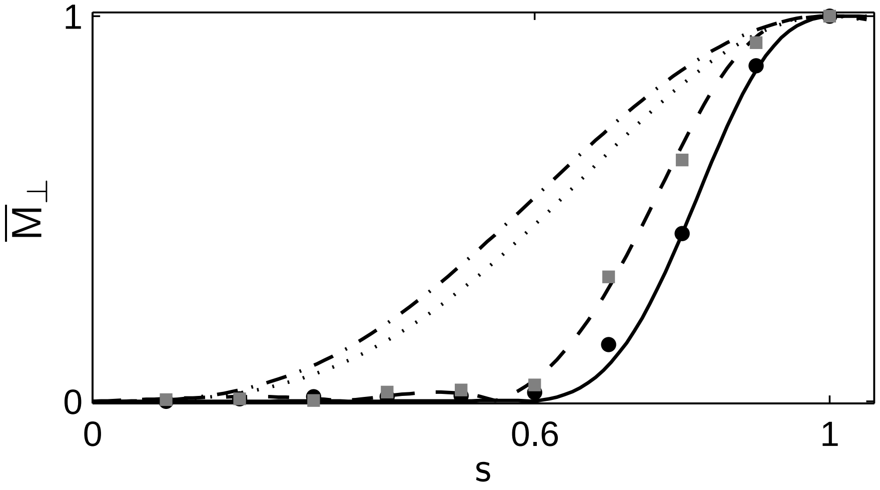

Figure 2.11: Slices from Fig. 2.10 A (dotted), B (dash-dotted), C (dashed) and D (solid curve) for the on resonance case. The gray squares and black discs represent experimental data for the conventionally optimized pulse and the two-step COOP WET cycle from Fig. 2.10 C and D, respectively.

## 2.4 Discussion and conclusion

In this chapter, we introduced the concept of simultaneously optimized pulses that act in a cooperative way, compensating each other's imperfections. Although for simplicity only examples involving uncoupled spins were considered, it is important to note that the COOP approach can also be applied to coupled spin systems. With the help of generalized optimal control based algorithms, such as the presented variant of the GRAPE (gradient ascent pulse engineering) algorithm, COOP pulses can be efficiently optimized.

Although the COOP approach is not limited to multi-scan experiments, here we focussed on applications where different members of a COOP cycle are used in different scans. In such multi-scan experiments, the COOP approach can be viewed as complementing and/or generalizing phase cycling [45–48] and difference spectroscopy. In conventional phase cycling, identical pulses are applied in each scan, up to an overall phase shift. In section 2.3.1, the optimal COOP cycle also consisted of pulses that were identical up to an overall phase shift. Hence, it is possible to automatically generate phase cycles using the COOP approach. However, it is important to point out that here it was not possible to achieve the target of the optimization by considering coherence order pathways alone. Hence, the COOP solution relied on the simultaneous optimization of specific pulse shapes (saturation pulses) in combination with the resulting simple phase cycle. As demonstrated in sections 2.3.2 – 2.3.5, COOP pulses are in general not simply related by overall phase shifts. In the presented COOP examples, a constant receiver phase was assumed. However, it is straightforward to lift this restriction by adding one additional control for the receiver phase for increased flexibility as in conventional phase cycles or in difference spectroscopy. In conventional difference spectroscopy, often different pulses are applied in successive scans. However, these pulses are typically either simple rectangular pulses or are optimized for each individual scan, not taking advantage of the full flexibility of the COOP approach introduced here. For example, this was illustrated in section 2.3.5 for the problem of solvent suppression.

Optimal control based techniques for the efficient optimization of complex COOP pulses open new avenues for pulse sequence optimization.

The goal of the presented examples was to illustrate the basic concept and to point out potential applications of COOP pulses. For example, in section 2.3.5 it was demonstrated that the approach may be useful for water suppression techniques such as WET. However, for practical solvent suppression, it is necessary to adjust the design criteria for the optimized COOP pulses, which is beyond the scope of the present thesis. It is also important to point out that the presented algorithm for the optimization of COOP pulses can be generalized in a straightforward way to include relaxation effects [11, 22]. We hope that the presented COOP approach will find practical applications in NMR spectroscopy and imaging.

# 3 Single-scan cooperative pulses

In this chapter, we present the concept of single-scan cooperative ($S^2$-COOP) pulses. In contrast to multi-scan COOP pulses that are applied at the same position in different scans, $S^2$-COOP pulses act in a single scan and at different positions of a pulse sequence. $S^2$-COOP pulses can be efficiently optimized using an extended version of the gradient ascent pulse engineering (GRAPE) algorithm. The advantage of the $S^2$-COOP approach is demonstrated in theory and experiment for NOESY-type frequency-labeling blocks.

## 3.1 Introduction

In the previous chapter, we have shown that the physical limits of pulse performance can be extended using the concept of cooperative (COOP) pulses that complements and generalizes phase-cycles [49]. In multi-scan experiments, COOP pulses can cancel undesired signal contributions: At the same position of a pulse sequence, a different pulse is applied in each scan so that the constituents of a so-called COOP cycle can cancel each other's imperfections. By taking advantage of the possibility of error cancelation between several scans the optimization enhances the overall fidelity of a selected transfer step in a pulse sequence. However, most NMR experiments rely on pulse sequences with several different transfer steps. Although it is possible to independently optimize different pulses before combining them to a pulse sequence [43] these pulses will only cancel each other's errors by chance or will even accumulate each other's errors in the course of a pulse sequence. Therefore, the demand on the fidelity of individually optimized pulses that are grouped together to a pulse sequence is extraordinarily high. It has been shown before how undesired effects of a precedent pulse can in part be canceled out by a subsequent pulse [5, 56, 60]. There, in contrast to the more flexible COOP approach, the precedent pulse remains unchanged so that the subsequent pulse alone has to compensate the errors of the precedent pulse. Another approach to avoid error accumulation is optimal tracking [44] which has so far only been applied to generate heteronuclear decoupling pulses. Here, we show that in contrast to our earlier COOP approach where a *single transfer* is optimized by taking advantage of error cancelation between *several scans*, it is possible to optimize *several transfers* in a *single scan*. We dub this modified COOP approach single-scan COOP ($S^2$-COOP) which makes it possible to further improve the performance of pulse sequences.

## 3.2 Theory

As a simple and illustrative example, we consider the frequency-labeling block in a standard 2D NOESY experiment. Building-blocks of this kind are routinely used in multidimensional NMR experiments in order to create offset-frequency labelled $z$ magnetization [50, 51]. In addition, they can be used as initial and final pulses in a modified INEPT block where instead of the central 180° universal rotation (UR) pulses two pairs of PP inversion pulses are applied on both nuclei [61, 62]. Here, we will focus on the frequency-labeling block of a 2D NOESY experiment. In Fig. 3.1 (top) the pulse sequence of a 2D NOESY experiment is drawn schematically.

### 3.2.1 Frequency-labeling of $z$ magnetization

The consecutive steps of an ideal conventional (i.e. using perfect 90° UR pulses [11, 23]) 2D NOESY frequency-labeling block are shown in the upper panel of Fig. 3.2. Two exemplary magnetization vectors with two different offset frequencies are drawn as solid and dashed arrows. The successive UR rotations are indicated by red arrows around the corresponding rotation axis. (PP and $S^2$-COOP transformations are indicated by segments of meridians on the Bloch sphere.) The theoretical effects of the first pulse (left), the $t_1$ evolution delay (center) and last pulse (right) are shown. Brighter arrows correspond to the magnetizations before a pulse or delay, darker arrows show the situation afterwards. In an ideal version of the 2D NOESY experiment based on UR pulses (top panel of Fig. 3.2), an initial $90^\circ_y$ pulse (left) uniformly and independently of $\omega$ creates $x$ magnetization, i.e.

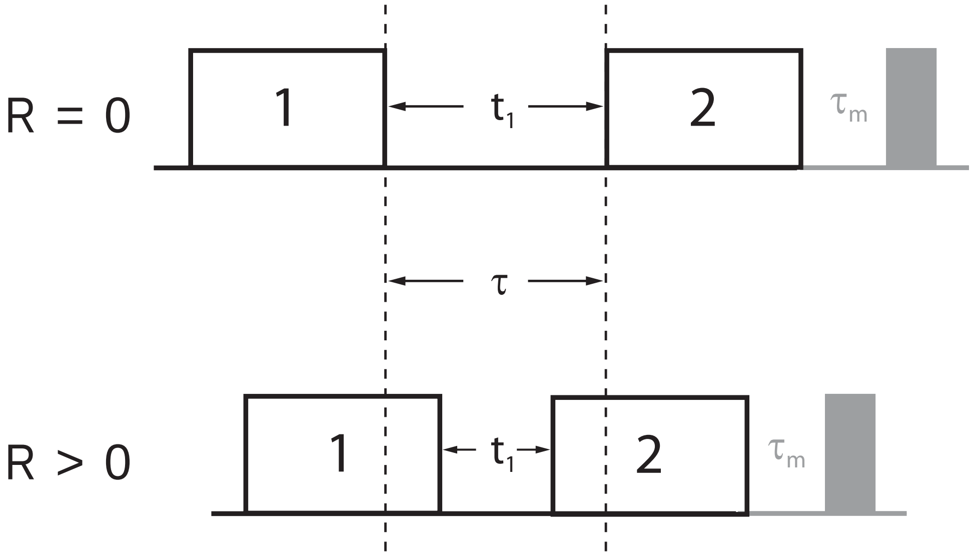

Figure 3.1: Schematic representations of 2D NOESY pulse sequences are shown. If pulses with $R = 0$ are employed, the delay $t_1$ is equal to the effective free evolution time $\tau$. However, if $R \neq 0$ and both pulses have the same value of $R$ the effective free evolution time is $\tau = t_1 + 2RT$. Thus, for same pulse lengths, the overall duration of a sequence with $R > 0$ is reduced by $2RT$. Simultaneously, there is a minimal value for $t_1$: $t_1^{min} = 2RT$ (see text).

$\boldsymbol{M}(\omega) = (M_x(\omega),\ M_y(\omega),\ M_z(\omega))^\top = (1,0,0)^\top$. During $t_1$ (center) $\boldsymbol{M}(\omega)$ evolves according to its offset frequency $\nu_{off} = \omega/(2\pi)$, resulting in $\boldsymbol{M}(\omega) = (\cos(\omega t),\ \sin(\omega t),\ 0)^\top$. Then the $x$ component of $\boldsymbol{M}(\omega)$ is rotated back to the $z$ axis by a $90^\circ_{-y}$ pulse (right), resulting in $\boldsymbol{M}(\omega) = (0,\ \sin(\omega t),\ \cos(\omega t))^\top$. The remaining transverse magnetization is removed by coherence pathway selection techniques [45–47] and the important result of this preparation sequence is the modulated $z$ magnetization given by $M_z(\omega) = \cos(\omega t)$. (Polarization transfer takes place during the mixing period $\tau_m$ (cf. Fig. 3.1). The remaining original $z$ magnetization and the $z$ magnetization having been transferred to other spins by NOE are finally transferred to observable magnetization by the last pulse which in the final 2D-spectrum results in diagonal and cross-peaks, respectively.)

Since rectangular pulses are not ideal hard pulses, their behavior is close to that of ideal pulses only within a narrow offset range. If a wider offset range has to be covered, one could replace rectangular pulses by optimized UR pulses [11, 23]. However, in this setting it is not necessary to employ two UR pulses, a transformation series $z \longrightarrow x$ followed by $x \longrightarrow z$ is sufficient. This can also be performed by two PP transformations. Replacing UR by PP pulses confers an additional degree of freedom to the optimization (cf. Fig. 3.3 and table 3.1). Therefore, for the same experimental parameters and constraints, a higher fidelity is expected when using PP instead of UR pulses. Alternatively, shorter pulse sequences with the same fidelity can be obtained when replacing UR by PP pulses.

As shown in Fig. 3.2, a UR $90^\circ_y$ and a $\mathrm{PP}_{z\rightarrow x}$ pulse on $\boldsymbol{M}_z$ will both create $\boldsymbol{M}_x$. However, there is an important difference: For a UR $90^\circ_y$ pulse there is for all offset frequencies $\nu_{off} = \omega/2\pi$ only one solution for the effective rotation matrix $\boldsymbol{S}(\omega)$ that describes the effect of a pulse on a magnetization vector $\boldsymbol{M}$ (cf. appendix 3.5.1) which is in our case

$$\boldsymbol{S}_{UR}(\omega) = \boldsymbol{R}_y(\pi/2) \tag{3.1}$$

where $\boldsymbol{R}_l(\eta)$ rotates by $\eta$ about the $l$ axis and $l = x, y, z$. (In addition, a rotation matrix can be represented by a rotation vector $\boldsymbol{r} = \eta\ \boldsymbol{e}$ describing a rotation by $\eta$ about the axis $\boldsymbol{e}$.) Therefore, the optimization of a UR pulse has no degrees of freedom with respect to the target effective rotation matrix. In contrast, the effective rotation matrix of a $\mathrm{PP}_{z\rightarrow x}$

pulse can be written as

$$\boldsymbol{S}_{PP}(\omega) = \boldsymbol{R}_y(\pi/2)\boldsymbol{R}_z(\alpha). \tag{3.2}$$

Here, we wrote $\boldsymbol{S}_{PP}(\omega)$ in a fixed-frame Euler angle decomposition using the $zyz$-convention (Eq. 3.30 in appendix 3.5.1): Any rotation $\boldsymbol{S}$ can be completely described by three successive rotations: (1) by $\alpha$ about $z$, (2) by $\beta$ about $y$ and (3) by $\gamma$ about $z$, i.e. $\boldsymbol{S} = \boldsymbol{R}_z(\gamma)\boldsymbol{R}_y(\beta)\boldsymbol{R}_z(\alpha)$. Since for the $\text{PP}_{z\to x}$ pulse we start at $\boldsymbol{M}_z$, an arbitrary $z$-rotation $\boldsymbol{R}_z(\alpha)$ is allowed since it will not affect the initial magnetization. The following rotations transform $\boldsymbol{M}_z$ to $\boldsymbol{M}_x$, therefore $\beta = \pi/2$ and $\gamma = 0$. Because $\alpha$ may take any value, replacing the initial UR by a PP pulse provides one additional degree of freedom. The set of all admissible rotation vectors $\boldsymbol{r}$ for a $\text{PP}_{z\to x}$ pulse is displayed in Fig. 3.3 as a black line (cf. Fig 2 in [23]). The only solution for the UR $90^\circ_y$ pulse is $\boldsymbol{r} = (0\ \pi/2\ 0)^\top$, indicated by a black circle in Fig. 3.3, which is only one of an infinite number of solutions for the PP problem.

Another difference between the UR and PP sequences from Fig. 3.2 is observed in the last step of the sequence: The final $90^\circ_{-y}$ UR pulse rotates all $x$ components back to the $z$ axis and all $y$ components remain along the $y$ axis. Also in the case of the PP sequence, all $x$ components are brought back to the $z$ axis, however, $y$ components do not in general stay along the $y$ axis. Nevertheless, all $y$ magnetization that is present at the beginning of the $\text{PP}_{x\to z}$ pulse, is still in the transverse plane at its end (cf. appendix 3.5.5 Eq. 3.35). However, the phase of the transverse magnetization component is undefined which reflects the additional degree of freedom with respect to the UR sequence. Here, the set of allowed final states is formed by a cone with its apex being identical to the origin, its axis being collinear with the $z$ axis and its aperture being defined by $\theta = 2\omega t_1$ (cf. Fig. 3.2). In the course of a 2D experiment, the transverse components will be removed by techniques of coherence pathway selection [45–47]. Thus, a frequency-labeling block using PP pulses has the same net effect as the sequence employing UR pulses. For both the UR as well as the PP sequences it is sufficient to only optimize one single pulse. For the UR sequence a simple phase shift of $\pi$ is sufficient to create the $90^\circ_{-y}$-rotation. The conversion of a $\text{PP}_{z\to x}$ to a $\text{PP}_{x\to z}$ pulse is shown in appendix 3.5.1. Entire frequency-labeling sequences using UR and PP pulses are described in theory in sections 3.5.4 and 3.5.5 of the appendix, respectively.

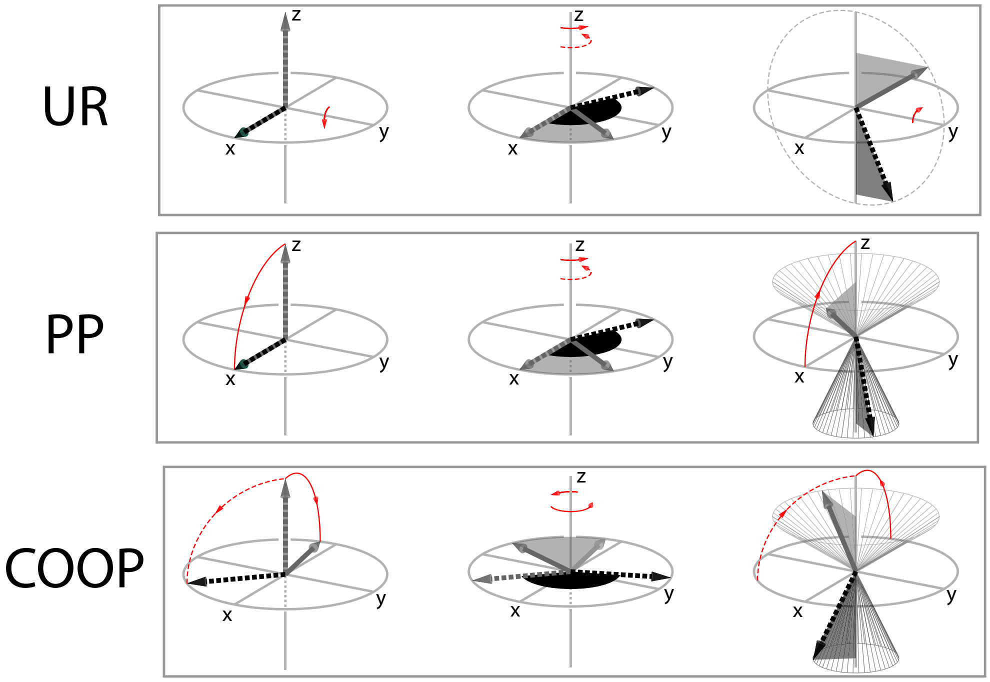

Figure 3.2: The effects of the first pulse (left), the $t_1$-evolution delay (center) and of the second pulse (right) of a frequency-labeling sequence (cf. Fig. 3.1) with $R = 0$ are shown for universal rotation (UR), point-to-point (PP) and single-scan COOP ($S^2$-COOP) pulses. In the left and center graphs, bright and dark arrows represent the situation before and after the pulse or delay, respectively. The straight arrow stands for a spin with smaller, the dashed arrow stands for a spin with a larger offset frequency.

### 3.2.2 Frequency-labeling with S$^2$-COOP pulses

In the conventional implementations of the NOESY experiment which we discussed so far, a first pulse transforms $\boldsymbol{M}_z$ to $\boldsymbol{M}_x$, i.e. magnetization with uniform phase for all offsets $\omega$, and the second pulse rotates $\boldsymbol{M}_x$ back to $\boldsymbol{M}_z$. For $t_1 > 0$ only the remaining $x$ component is rotated back to $z$ and retained whereas all other components are discarded (Fig. 3.2 PP and UR). However, it is not necessary that all magnetization vectors are oriented along the same axis after the first pulse. In principle, the first pulse can rotate the initial $z$ magnetization to *any* position in the transverse plane. However, the second pulse of the sequence then has to pick up the magnetization at the same place where it was placed by the first pulse. Due to the chemical shift evolution during $t_1$ the magnetization will be rotated by $\omega t_1$ and only the $\cos(\omega t_1)$-modulated component of $\boldsymbol{M}$ will be rotated back to $z$ wheras the $\sin(\omega t_1)$-component will remain in the transverse plane. The overall result of such a sequence is equivalent to the results of the UR and PP sequences (Fig. 3.2).

This results in the problem to find a pair of pulses of which the first, starting from $\boldsymbol{M}_z$, creates transverse magnetization with arbitrary phase and the second brings back this magnetization to the initial $z$ magnetization. This problem can be solved by a new approach which we call single-scan cooperative (S$^2$-COOP) pulses. The S$^2$-COOP approach represents a modification of our previously presented multi-scan COOP pulses (cf. chapter 2 and [49]).

#### General description of the S$^2$-COOP approach

The S$^2$-COOP pulse approach comprises two steps: The first step is the optimization of a pulse pair A and B that starting from $\boldsymbol{M}_z$ creates transverse magnetization with opposite phase $\varphi$, i.e.

$$\varphi^{(A)} = -\varphi^{(B)}. \tag{3.3}$$

In other words, starting from $z$ magnetization for each pulse, the two final magnetization vectors created by the pulses must be symmetric with respect to the $x$ axis (Fig. 3.4). Representing the effective rotation matrices of the pulses A and B, $\boldsymbol{S}^{(A)}(\omega)$ and $\boldsymbol{S}^{(B)}(\omega)$, in the $zyz$ Euler angle base (appendix 3.5.1 Eq. 3.30) yields

$$\boldsymbol{S}^{(A)}(\omega) = \boldsymbol{R}_z(\gamma)\boldsymbol{R}_y(\pi/2)\boldsymbol{R}_z(\alpha^{(A)})$$

and

$$\boldsymbol{S}^{(B)}(\omega) = \boldsymbol{R}_z(-\gamma)\boldsymbol{R}_y(\pi/2)\boldsymbol{R}_z(\alpha^{(B)})$$

where, in this case, $\gamma = \varphi^{(A)}$ and $-\gamma = \varphi^{(B)}$.

One of these pulses, e.g. pulse A, can directly be employed as pulse 1 in a frequency-labeling sequence (Fig. 3.1). Pulse 2 of the sequence is obtained in the second step of the S$^2$-COOP pulse approach. In this step, the other pulse, e.g. pulse B, is phase-inverted and time-reversed to yield the second pulse (2) of the sequence. For example, when using Eq. 3.31 from appendix 3.5.1 and using A as the first pulse the effective rotation matrix of pulse 2 can be written as [23]

$$\boldsymbol{S}^{(2)}(\omega) = \overline{\boldsymbol{S}^{(B)}}^{tr}(\omega) = \boldsymbol{R}_z(\alpha^{(B)})\boldsymbol{R}_y(-\pi/2)\boldsymbol{R}_z(-\gamma).$$

The consecutive steps of the sequence are
(1) rotation of $\boldsymbol{M}_z$ to the transverse plane ($\boldsymbol{S}^{(A)}(\omega)$)
(2) chemical shift evolution ($\boldsymbol{R}_z(\omega t_1)$) and
(3) backrotation of the $\cos(\omega t_1)$-modulated part of the transverse magnetization to the $z$ axis ($\overline{\boldsymbol{S}^{(B)}}^{tr}(\omega)$):

$$\begin{aligned}\overline{\boldsymbol{S}^{(B)}}^{tr}(\omega)\boldsymbol{R}_z(\omega t_1)\boldsymbol{S}^{(A)}(\omega) =&\boldsymbol{R}_z(\alpha^{(B)})\boldsymbol{R}_y(-\pi/2)\boldsymbol{R}_z(-\gamma)\\ &\times \boldsymbol{R}_z(\omega t_1)\boldsymbol{R}_z(\gamma)\boldsymbol{R}_y(\pi/2)\boldsymbol{R}_z(\alpha^{(A)})\\ =&\boldsymbol{R}_z(\alpha^{(B)})\boldsymbol{R}_y(-\pi/2)\\ &\times \boldsymbol{R}_z(\omega t_1)\boldsymbol{R}_y(\pi/2)\boldsymbol{R}_z(\alpha^{(A)}).\end{aligned} \tag{3.4}$$

In the above equation, $\boldsymbol{R}_z(\gamma)$ and $\boldsymbol{R}_z(-\gamma)$ cancel. Apart from two different values for $\alpha^{(A)}$ and $\alpha^{(B)}$, the final line is equivalent to the effect of a corresponding PP sequence (cf. appendix 3.5.5). However, $\boldsymbol{R}_z(\alpha^{(A)})$ does not have any effect in the experiment because it is applied to $z$ magnetization. Then, multiplication with $\boldsymbol{R}_y(\pi/2)$ yields $\boldsymbol{M}_x$ which evolves chemical shift according to $\boldsymbol{R}_z(\omega t_1)$. The resulting $x$ component $\boldsymbol{M}_x\cos(\omega t_1)$ is then rotated back to the $z$ axis by $\boldsymbol{R}_y(-\pi/2)$. The same rotation keeps the $y$ component $\boldsymbol{M}_y \sin(\omega t_1)$ untouched. The final rotation $\boldsymbol{R}_z(\alpha^{(B)})$ has no effect on the desired $\cos(\omega t_1)$-modulated $z$ magnetization. The same rotation causes a phase-shift by $\alpha^{(B)}$ of the $y$ component which will however stay in the transverse plane. All transverse components will be canceled using coherence transfer pathway selection [45–47]. Thus, the same overall effect as for UR or PP sequences is obtained although we allowed the magnetization phase after the first pulse to take an arbitrary value. This is only possible if the transverse magnetization phases created by A and B are related by $\varphi^{(A)} = -\varphi^{(B)}$: Two S$^2$-COOP pulses transform the magnetization vectors not in a uniform (UR and PP) but yet in a concerted fashion. The fact that the phase of $\boldsymbol{M}$ may be undefined after the first pulse opens up another degree of freedom to the frequency-labeling sequence which in turn paves the way for improved frequency-labeling sequences.

Fig. 3.3 illustrates the gain in degrees of freedom for UR, PP and S$^2$-COOP pulses. The admissible sets of effective rotation vectors $\boldsymbol{r}$ (see also above and [23]) for a PP pulse (black line) and S$^2$-COOP pulses (gray surface) are displayed. For a UR pulse the effective rotation angles in the $zyz$ Euler base (Eq. 3.30) are all defined, i.e. $\alpha = 0$, $\beta = \pi/2$ and $\gamma = 0$. There is no degree of freedom and the only solution is $\boldsymbol{r} = (0\ \pi/2\ 0)^\top$ (black circle in Fig. 3.3). Since for a PP pulse we initially start at $\boldsymbol{M}_z$, $\alpha$ can be of any value because $\boldsymbol{R}_z(\alpha)$ does not have an effect on $\boldsymbol{M}_z$. However, $\beta$ and $\gamma$ are fixed: $\beta = \pi/2$ and $\gamma = 0$. The admissible effective rotation vectors for a PP$_{z\rightarrow x}$ pulse are defined by the set of all effective rotation matrices $\boldsymbol{S}(\omega) = \boldsymbol{R}_y(\pi/2)\boldsymbol{R}_z(\alpha)$ where $\alpha$ may take any value (Eq. 3.2). In Fig. 3.3 the tips of these vectors are displayed as a black *line* reflecting the single degree of freedom. The admissible set of S$^2$-COOP pulses is defined by $\boldsymbol{S}(\omega) = \boldsymbol{R}_z(\gamma)\boldsymbol{R}_y(\pi/2)\boldsymbol{R}_z(\alpha)$ where now both $\alpha$ and $\gamma$ may take any value as long as $\gamma^{(A)} = -\gamma^{(B)}$. There are two degrees of freedom for a S$^2$-COOP pulse. Thus, the admissible rotation vectors form a two-dimensional *surface* of revolution. However, the effective number of degrees of freedom for a pair of S$^2$-COOP pulses is restricted: When an effective rotation vector for A is chosen from the two-dimensional surface, it will lie on a line of an equivalent PP pulse that transforms $\boldsymbol{M}_z$ to $\boldsymbol{M}_x \cos(\varphi) + \boldsymbol{M}_y \sin(\varphi)$. Then the admissible set of effective rotation vectors for B collapses to a line corresponding to a PP pulse that transforms $\boldsymbol{M}_z$ to $\boldsymbol{M}_x \cos(-\varphi) + M_y \sin(-\varphi)$. Thus, the overall number of degrees of freedom for a S$^2$-COOP pulse pair is equal to three. The results are summarized in table 3.1.

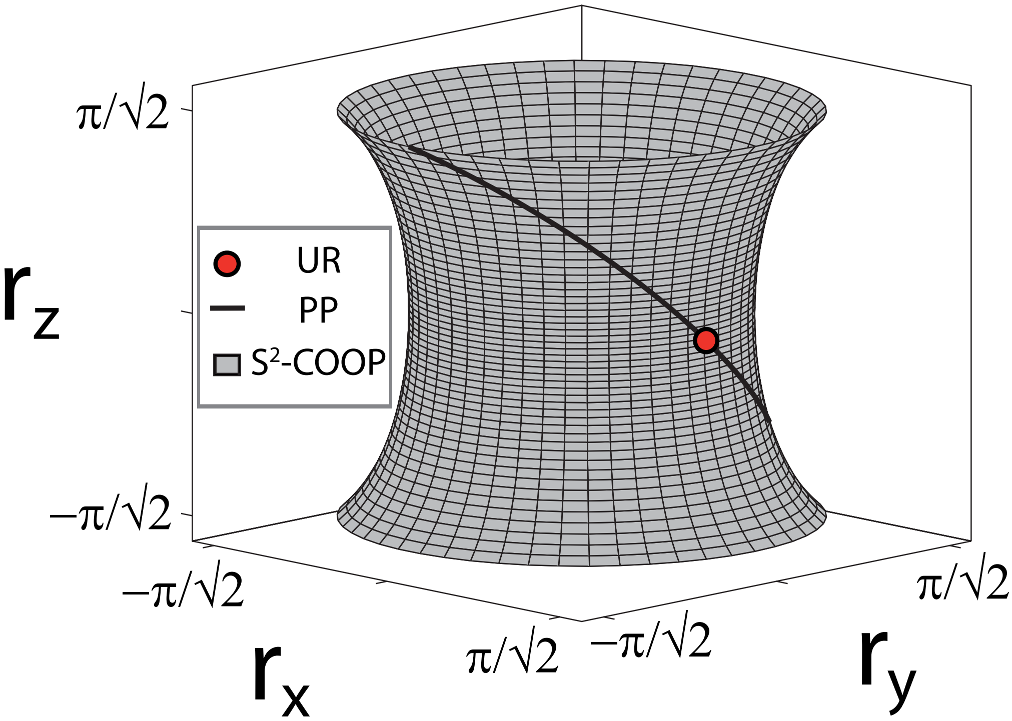

Figure 3.3: The sets of all admissible rotation vectors for a S$^2$-COOP (or saturation) pulse and a PP pulse are displayed as a gray surface and a black curve, respectively. For a UR pulse the admissible set is restricted to a single point, e.g. $\beta = (0,\ \pi/2,\ 0)^\top$ for a $\pi/2$-rotation about $y$ (black circle).

### Quality factor

The first step of the S$^2$-COOP approach comprises the optimization of a cooperative pulse pair A and B that both starting from $\boldsymbol{M}_z$ create transverse magnetization with opposite phases $\varphi^{(A)} = -\varphi^{(B)}$ (cf. Eq. 3.3 and Fig. 3.4). In other words, at the end of each pulse with pulse duration $T^{(A)} = T^{(B)} = T$, both $\boldsymbol{M}^{(A)}(T)$ and $\boldsymbol{M}^{(B)}(T)$ (1) should lie in the transverse plane and (2) should be of opposite phase, corresponding

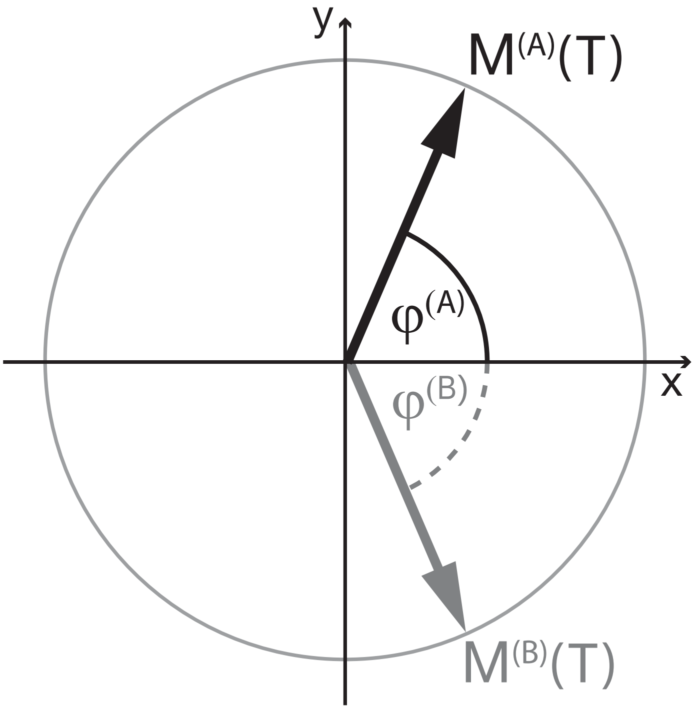

Figure 3.4: The first step of the construction procedure of two S$^2$-COOP pulses comprises the optimization of a pulse pair A and B that starting from $z$ magnetization create transverse magnetization $M^{(A)}(T)$ and $M^{(B)}(T)$ with opposite phase: $\varphi^{(A)} = -\varphi^{(B)}$.

Table 3.1: **Euler rotation angles for different frequency-labeling sequences.**

| | **UR** | **PP** | **pseudo-S$^2$-COOP** | **S$^2$-COOP** |
|---|---|---|---|---|
| $\alpha^{(1)}$ | 0 | undefined[I] | $\alpha^{(1)}(\omega) = -\gamma^{(2)}(-\omega)$ | undefined |
| $\beta^{(1)}$ | $\pi/2$ | $\pi/2$ | $\pi/2$ | $\pi/2$ |
| $\gamma^{(1)}$ | 0 | 0 | $\gamma^{(1)} = -\alpha^{(2)}$ | $\gamma^{(1)} = -\alpha^{(2)}$ |
| $\alpha^{(2)}$ | 0 | 0 | $\alpha^{(2)} = -\gamma^{(1)}$ | $\alpha^{(2)} = -\gamma^{(1)}$ |
| $\beta^{(2)}$ | $\pi/2$ | $-\pi/2$ | $-\pi/2$ | $-\pi/2$ |
| $\gamma^{(2)}$ | 0 | undefined[I] | $\gamma^{(2)}(\omega) = -\alpha^{(1)}(-\omega)$ | undefined |
| degrees of freedom | 0 | 1 | 2 | 3 |

The effective rotation matrices of pulses 1 and 2 of the frequency-labeling sequences can be written as $\boldsymbol{S}^{(1)}(\omega) = \boldsymbol{R}_z(\gamma^{(1)})\boldsymbol{R}_y(\beta^{(1)})\boldsymbol{R}_z(\alpha^{(1)})$ and $\boldsymbol{S}^{(2)}(\omega) = \boldsymbol{R}_z(\gamma^{(2)})\boldsymbol{R}_y(\beta^{(2)})\boldsymbol{R}_z(\alpha^{(2)})$. For (pseudo-)S$^2$-COOP pulse pairs (p. 54) $\alpha^{(2)} = -\gamma^{(1)}$ (Eq. 3.3). For pseudo-S$^2$-COOP pulses (and symmetric S$^2$-COOP pulse pairs, cf. Eq. 3.16): $\boldsymbol{S}^{(2)}(\omega) = (\boldsymbol{S}^{(1)}(-\omega))^{-1}$ (Eq. 3.22), e.g. $\alpha^{(1)}(\omega) = -\gamma^{(2)}(-\omega)$. In addition, for ideal S$^2$-COOP pulses that act symmetrically with respect to $\omega$ (Eqs. 3.19 and 3.20) pulse 2 is the inverse of pulse 1: $\boldsymbol{S}^{(2)} = (\boldsymbol{S}^{(1)})^{-1}$ (Eq. 3.23), e.g. $\alpha^{(1)} = -\gamma^{(2)}$.

(I) If the conversion principle from appendix 3.5.1 is used, then $\alpha^{(1)} = \gamma^{(2)}$ (Eq. 3.30).

to a $\pi$-rotation about the $x$ axis (cf. Fig. 3.4):

$$\boldsymbol{M}^{(A)}(T) = \begin{pmatrix} M_x^{(A)}(T) \\ M_y^{(A)}(T) \\ 0 \end{pmatrix} = \begin{pmatrix} M_x^{(B)}(T) \\ -M_y^{(B)}(T) \\ 0 \end{pmatrix} = \boldsymbol{R}_x(\pi)\boldsymbol{M}^{(B)}(T). \quad (3.5)$$

(S$^2$-COOP pulses can in principle have different pulse durations. For simplicity reasons, here, we only consider the case where both pulses $A$ and $B$ have the same duration $T$.) One way to achieve this is to maximize the scalar product of $\boldsymbol{M}^{(A)}(T)$ and the image of $\boldsymbol{M}^{(B)}(T)$ rotated by $\pi$ about the $x$ axis:

$$\Phi_a = M_x^{(A)}(T) \cdot M_x^{(B)}(T) - M_y^{(A)}(T) \cdot M_y^{(B)}(T) \quad (3.6)$$

Here, the pulse performance $\Phi_a$ only depends on the final magnetization vectors $\mathbf{M}^{(k)}(T)$ ($k$ =A,B) after each pulse of duration $T^{(A)} = T^{(B)} = T$ so that the costate vectors $\lambda^{(k)}(T)$ of the GRAPE procedure are given by $\partial\Phi/\partial\mathbf{M}^{(k)}(T)$ [16,49]. For $\Phi_a$ the costate vectors are

$$\boldsymbol{\lambda}^{(A)}(T) = \begin{pmatrix} M_x^{(B)}(T) \\ -M_y^{(B)}(T) \\ 0 \end{pmatrix} \quad (3.7)$$

and

$$\boldsymbol{\lambda}^{(B)}(T) = \begin{pmatrix} M_x^{(A)}(T) \\ -M_y^{(A)}(T) \\ 0 \end{pmatrix}. \quad (3.8)$$

The costate $\boldsymbol{\lambda}^{(k)}(T)$ of *one* pulse exclusively depends on the final transverse magnetization vectors generated by the *other* pulse. This reflects that, although two different pulses are optimized, they are tightly intertwined. The gradient of the quality factor with respect to the controls $\nu_x^{(k)}(t) = \omega_x^{(k)}(t)/2\pi$ and $\nu_y^{(k)}(t) = \omega_y^{(k)}(t)/2\pi$ is given by the $x$ and $y$ components of the vectors $\boldsymbol{M}^{(k)}(t) \times \boldsymbol{\lambda}^{(k)}(t)$ [16,49]:

$$\frac{\delta\Phi}{\delta\nu_x^{(k)}} = M_y^{(k)}(t)\lambda_z^{(k)}(t) - M_z^{(k)}(t)\lambda_y^{(k)}(t) \quad (3.9)$$

and

$$\frac{\delta\Phi}{\delta v_y^{(k)}} = M_z^{(k)}(t)\lambda_x^{(k)}(t) - M_x^{(k)}(t)\lambda_z^{(k)}(t) \tag{3.10}$$

A schematic overview of the gradient calculation is shown in Fig. 3.5.

### 3.2.3 S$^2$-COOP pulses with linear phase slope

There are many practical applications where an excitation pulse is followed by a free-evolution delay. This is also the case for the present NOESY frequency-labeling block. We have shown before that in such cases excitation pulses with uniform phase can be replaced by so-called ICEBERG pulses that create transverse magnetization with linear phase slope [21].

The phase slope of ICEBERG pulses can be characterized by the ratio $R$ of a virtual time $T'$ – during which chemical shift (and coupling) evolution is active – and the pulse duration $T$: $R = T'/T$. A value of $R = 0$ denotes an excitation pulse with uniform phase, whereas $R = 1$ indicates that the corresponding pulse creates a magnetization profile as if magnetization with uniform phase had been present at $t = 0$ and free evolution took place during the entire duration of the pulse $T$. Pulses with good performance can be optimized even if $R < 0$. It has been shown that in many cases ICEBERG pulses perform better than comparable uniform phase excitation pulses.

When a pulse that is applied before a free-evolution delay is to be replaced by an ICEBERG pulse one has to consider that for $R > 0$ chemical shift and coupling already start to be effective during the pulse at $1 - RT$. Therefore, the pulse has to be shifted by $RT$ [21] which shortens the total duration of the entire excitation-delay sequence (cf. Fig. 3.1).

In analogy to the ICEBERG formalism, we derived a quality factor (appendix 3.5.8) that allows to shift both pulses of a S$^2$-COOP frequency-labeling sequence towards $t_1$ (Fig. 3.1). Therefore, the duration of the whole frequency-labeling block is shortened by $2RT$. When the actual delay between the two pulses is set to zero, the minimal effective free-evolution time $t_1^{min}$ is $2RT$. The consequence on a 2D NOESY spectrum that has been recorded with S$^2$-COOP pulses with $R \neq 0$ is a linear phase error in $t_1$ which can be removed by first-order phase correction. For larger values of $RT$ first-order phase correction will lead to a rolling

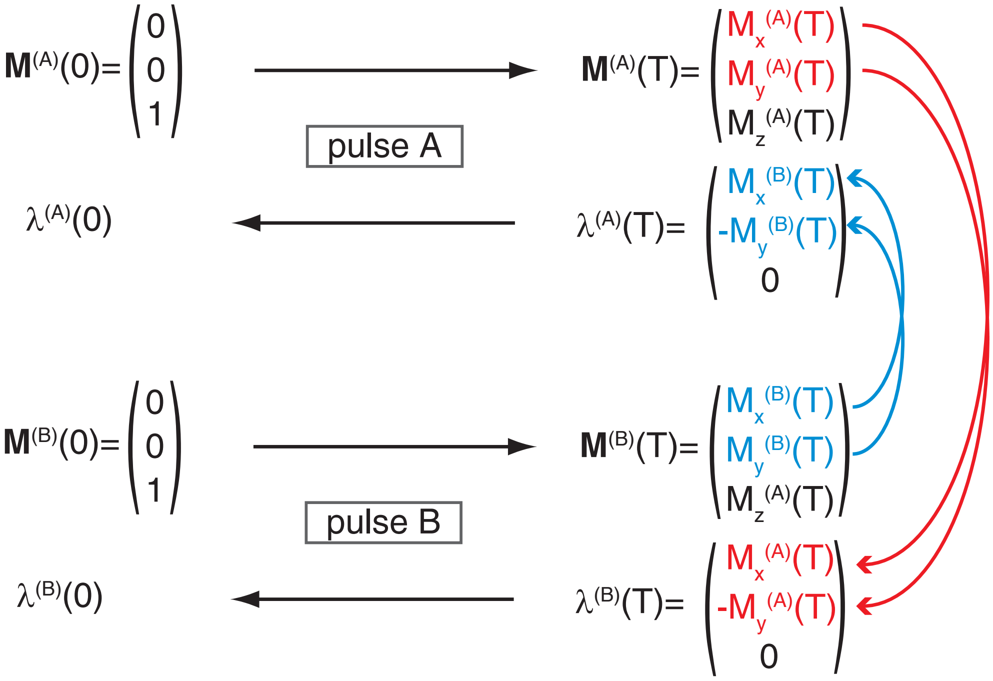

Figure 3.5: The gradient calculation during the optimization of a pair of S$^2$-COOP pulses A and B is drawn schematically. First, the trajectories of both magnetization vectors $\boldsymbol{M}^{(A)}(t)$ and $\boldsymbol{M}^{(B)}(t)$ are calculated. Then, the final costate vectors $\boldsymbol{\lambda}^{(k)}(T)$ are calculated: The final costate vector of one pulse entirely depends on the final state of the other pulse (red and blue arrows). Then, the trajectories of the costates $\boldsymbol{\lambda}^{(k)}(t)$ are calculated backward in time upon which the gradients of all controls $\delta\Phi/\delta v_x^{(k)}(t)$ and $\delta\Phi/\delta v_y^{(k)}(t)$ are calculated according to Eqs. 3.9 and 3.10. Either pulse A or B can be used as the first pulse of a frequency-labeling sequence. Its counterpart (B or A) is then time-reversed and phase-inverted to yield the second pulse of the sequence (see text).

base-line. This problem can be alleviated by applying backward linear prediction instead of large first-order phase correction.

In terms of the Euler angle decomposition from appendix 3.5.1 (Eq. 3.30), the effective rotation matrices of the pulses A and B become

$$\begin{aligned} \boldsymbol{S}^{(A)}(\omega) &= \boldsymbol{R}_z(\gamma^{(A)})\boldsymbol{R}_y(\pi/2)\boldsymbol{R}_z(\alpha^{(A)}) \\ &= \boldsymbol{R}_z(\gamma'^{(A)})\boldsymbol{R}_z(RT\omega)\boldsymbol{R}_y(\pi/2)\boldsymbol{R}_z(\alpha^{(A)}) \end{aligned} \tag{3.11}$$

and

$$\begin{aligned} \boldsymbol{S}^{(B)}(\omega) &= \boldsymbol{R}_z(\gamma^{(B)})\boldsymbol{R}_y(\pi/2)\boldsymbol{R}_z(\alpha^{(B)}) \\ &= \boldsymbol{R}_z(\gamma'^{(B)})\boldsymbol{R}_z(RT\omega)\boldsymbol{R}_y(\pi/2)\boldsymbol{R}_z(\alpha^{(B)}) \end{aligned} \tag{3.12}$$

For conventional ICEBERG pulses $\gamma'^{(A)} = \gamma'^{(B)} = 0$. For S$^2$-COOP pulses with linear phase slope Eq. 3.3 still holds in a modified version:

$$\gamma'^{(A)} = -\gamma'^{(B)}. \tag{3.13}$$

For $R = 0$, A and B ideally create transverse magnetization vectors that are symmetric with respect to a $\pi$-rotation about the $x$ axis (Eq. 3.5). Due to the additional $z$-rotation $\boldsymbol{R}_z(RT\omega)$ this rotation symmetry axis becomes offset-dependent:

$$\boldsymbol{M}^{(A)}(T) = \boldsymbol{R}_{(RT\omega)}(\pi)\boldsymbol{M}^{(B)}(T) \tag{3.14}$$

In the above equation, $\boldsymbol{R}_{(RT\omega)}(\pi)$ corresponds to a $\pi$-rotation about an axis in the transverse plane that forms an angle of $RT\omega$ with respect to the $x$ axis. Since for conventional ICEBERG pulses $\gamma'^{(k)} = 0$, the magnetization then lies *on* this symmetry axis.

## 3.3 Examples

As an illustrative example, we developed S$^2$-COOP pulses for 2D $^{13}$C–$^{13}$C NOESY experiments [63, 64] for a potential 30.5 T (1.3 GHz proton resonance frequency) spectrometer. The pulses have to cover an offset frequency range of 70 kHz corresponding to a chemical shift range of 215 ppm. The maximum allowed rf field amplitude was set to 10 kHz and an rf field inhomogeneity of ±5% was considered. The pulse lengths for all optimized pulses was set to $T = 75\ \mu$s which is only three times the duration of a rectangular $\pi/2$ pulse at the same rf amplitude. Pulse pairs for $R$ ranging from 0 to 0.9 were optimized. Conventional ICEBERG pulses and a PP$_{z\rightarrow x}$ pulse were optimized using the fidelity function

$$\Phi_0 = 1 - (T_x - M_x(T))^2 - (T_y - M_y(T))^2 - M_z(T)^2 \tag{3.15}$$

where $T_x = \cos(RT\omega)$ and $T_y = \sin(RT\omega)$ and the second pulse of the sequence was created by phase-inversion and time-reversal of the original pulse. The pulses were evaluated using $\Phi_a$ (Eq. 3.6) and $\Phi_b$ (Eq. 3.43), respectively . The results are displayed in Fig. 3.6.

For all considered values of $R$, S$^2$-COOP pulse pairs perform better than PP or ICEBERG pulses. The performance of S$^2$-COOP pulses is optimal for $R$ being close to 0.5. The best ICEBERG pulse was found for $R = 0.6$. For $R > 0.7$ the difference in performance of S$^2$-COOP and ICEBERG pulses becomes smaller with increasing $R$. For $R = 0.9$ the performances only differ by 0.0163 and the pulse shapes of ICEBERG and S$^2$-COOP pulses show large resemblance (Fig. 3.7). If $R$ is close to 1 the effective chemical shift evolution time $T' = RT$ (Eq. [21]) is close to the physical maximum $T$ of a free evolution delay without any pulse. Then, the freedom of the S$^2$-COOP approach is reduced, since it has to assure that chemical shift evolution takes place during almost the entire pulse duration. As a consequence, the difference between the optimal solutions for S$^2$-COOP and ICEBERG pulses becomes small for values of $R$ that are only slightly smaller than one.

The phases of the S$^2$-COOP pulses for $R = 0.9$ shown in Fig. 3.7 alternate between the values $\pm\pi/2+\delta$ for pulse A and $\pm\pi/2-\delta$ for pulse B. The value for $\delta$ is constant and has no effect on the performance of this pulse pair. In fact, the latter is true for any S$^2$-COOP pulse pair. If a constant value $\delta$ is added to the phase of pulse A and subtracted of the phase of pulse B the same is true for the phases of the final magnetization vectors $\varphi^{(A)}$ and $\varphi^{(B)}$. In Eq. 3.3, addition of $\varphi^{(B)}$ to both sides yields

$$\varphi^{(A)} + \varphi^{(B)} = 0.$$

If a constant value $\delta$ is added to $\varphi^{(A)}$ and subtracted of $\varphi^{(B)}$ we get

$$(\varphi^{(A)} + \delta) + (\varphi^{(B)} - \delta) = 0,$$

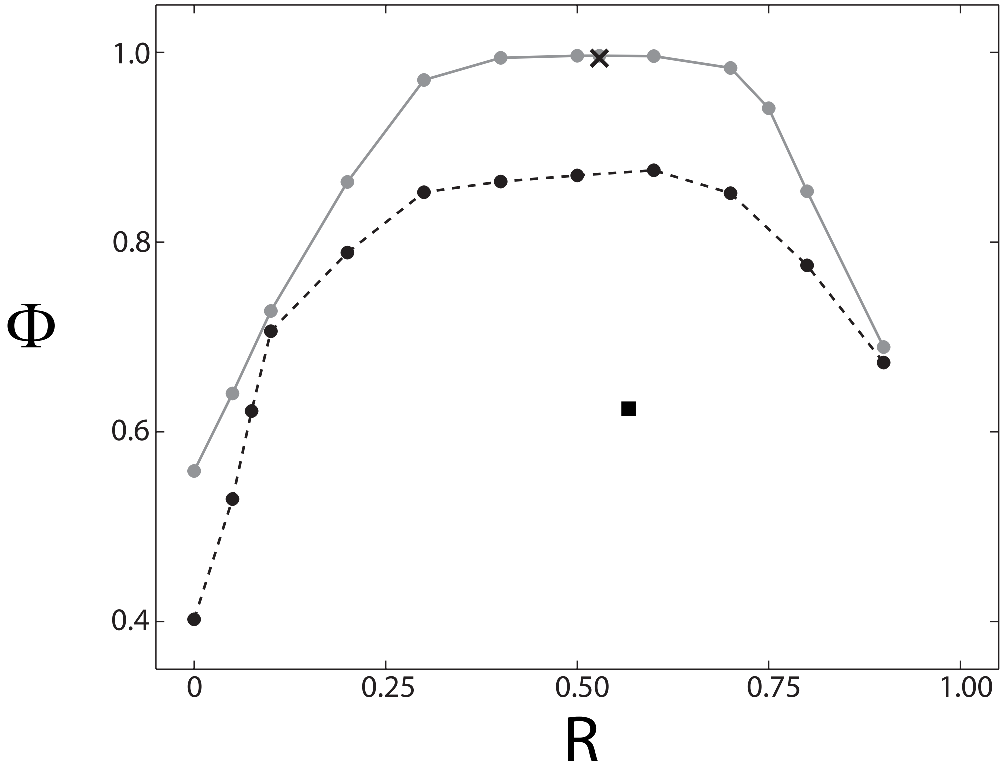

Figure 3.6: The quality functions $\Phi_a$ and $\Phi_b$, respectively, are plotted versus $R$ for $S^2$-COOP pulses (solid gray line and gray discs) and for ICEBERG pulses (dashed black line and black discs). The quality of a rectangular pulse is displayed as a square. The performance of the pulse pair that was constructed using a saturation pulse and Eq. 3.16 is displayed as a black cross. However, this construction principle does not work for saturation pulses in general (see text).

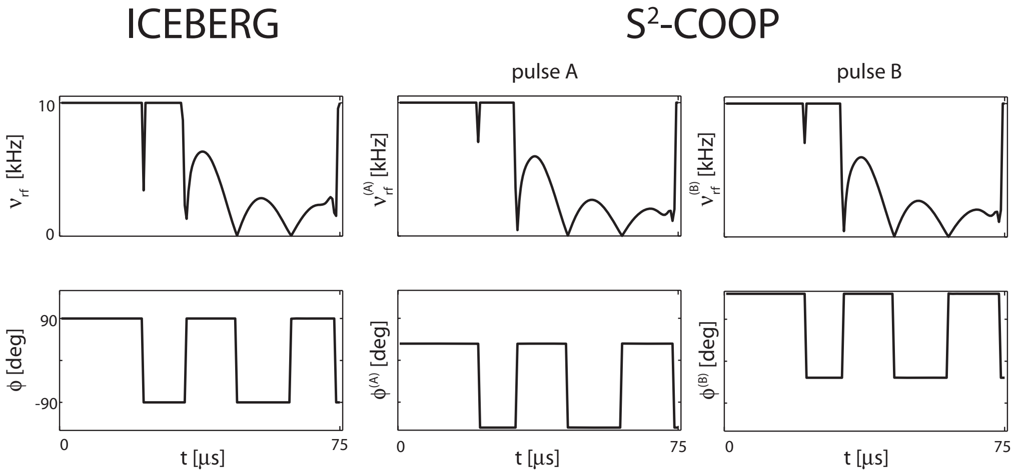

Figure 3.7: Pulse shapes of an ICEBERG pulse and a S$^2$-COOP pulse pair for $R = 0.9$. The time-dependent pulse amplitudes $\nu_{rf} = \sqrt{(\nu_x^2 + \nu_y^2)}$ (top) and phases $\phi = \text{atan}(\nu_y/\nu_x)$ (bottom) are shown. Note the large resemblance of the ICEBERG and S$^2$-COOP pulse shapes. The S$^2$-COOP pulses obey Eq. 3.16. In addition, the phases of both S$^2$-COOP pulses alternate between the values $\pm\pi/2 + \delta$ for pulse A and $\pm\pi/2 - \delta$ for pulse B. The value for $\delta$ is constant and has no effect on the performance of this pulse pair (see text).

where $\delta$ cancels and Eq. 3.3 still holds.

The performance of a rectangular excitation pulse is indicated in Fig. 3.6 as a black square. The same rf amplitude as for the optimized pulses ($\nu_{rf}^{max} = 10$ kHz) was chosen. Here, the optimal value for $R$ was found to be $R_{opt} = 0.567$ ($\Phi_b = 0.62445$). Close to resonance, the pulse performs well, but for increasing offset the performance decreases and almost reaches zero at the edges of the offset range (cf. Fig. 3.11 and Fig. 3.9).

All S$^2$-COOP pulses with $R \leq 0.6$ are almost perfect constant amplitude pulses completely exploiting the allowed maximum rf amplitude of 10 kHz. The amplitude profiles of all other S$^2$-COOP pulse pairs that were optimized are, for each pulse pair, almost identical. For all S$^2$-COOP pulse shapes with $R > 0.1$ as well as for the S$^2$-COOP pulse pair with $R = 0.05$ we find that the phases of the individual COOP pulses are related by phase inversion and an additional phase shift by $\pi$:

$$\varphi^{(B)} = -\varphi^{(A)} + \pi, \tag{3.16}$$

which is equivalent to a reflection of the phase around $\pi/2$. In chapter 2, where the COOP approach for several scans was presented, we observed exactly the same symmetry for the case of multi-scan COOP pulses for broadband excitation of $x$ magnetization with minimum phase error [49]. Although it seems counterintuitive that the S$^2$-COOP pulses A and B, generating magnetization with *arbitrary* phase, share symmetry properties with excitation pulses that generate magnetization with *exact* phase, what these different types of COOP pulses have in common, however, is that $y$ magnetization that is present for an offset $\omega$ at the end of one pulse has preferably the same magnitude but an opposite sign than its counterpart, i.e. $M_y^{(B)}(\omega) = -M_y^{(A)}(\omega)$. (The difference between the two COOP pulse types is that a small $|M_y^{(k)}(\omega)|$ is favorable for excitation with minimum phase error whereas $|M_y^{(k)}(\omega)|$ can be of any value for the present S$^2$-COOP pulses.)

The relations we deduced for excitation pulses with minimum phase error in [49] are also valid here. Thus for any pulse pair fulfilling Eq. 3.16 we can write

$$\begin{aligned} M_x^{(A)}(\omega) &= M_x^{(B)}(-\omega) \\ M_y^{(A)}(\omega) &= -M_y^{(B)}(-\omega), \end{aligned} \tag{3.17}$$

and $\Phi_a$ simultaneously maximizes the amount of transverse magnetization at the end of A and B with the condition that $\boldsymbol{M}^{(A)}(T)$ be symmetric to $\boldsymbol{M}^{(B)}(T)$ with respect to a $\pi$-rotation about the $x$ axis. Thus, for an ideal S$^2$-COOP pulse pair A and B we find

$$\begin{aligned} M_x^{(A)}(\omega) &= M_x^{(B)}(\omega) \\ M_y^{(A)}(\omega) &= -M_y^{(B)}(\omega). \end{aligned} \tag{3.18}$$

Upon combination of the two above equations we obtain

$$\begin{aligned} M_x^{(A)}(\omega) &= M_x^{(A)}(-\omega) \\ M_y^{(A)}(\omega) &= M_y^{(A)}(-\omega), \end{aligned} \tag{3.19}$$

and

$$\begin{aligned} M_x^{(B)}(\omega) &= M_x^{(B)}(-\omega) \\ M_y^{(B)}(\omega) &= M_y^{(B)}(-\omega), \end{aligned} \tag{3.20}$$

i.e. each pulse acts symmetrically with respect to $\omega$. For the case where $R \neq 0$, a linear, offset-dependent component $RT\omega$ is added. Then the offset profile of the magnetization phase can be described as the sum of a linear ($RT\omega$) and a symmetric component.

The pulse shapes are symmetric with respect to a $\pi$-rotation about the $y$ axis, so that the corresponding effective rotation matrices $\boldsymbol{S}^{(A)}(\omega)$ and $\boldsymbol{S}^{(B)}(-\omega)$ are related by (appendix 3.5.2):

$$\boldsymbol{S}^{(A)}(\omega) = \boldsymbol{R}_y(\pi)\ \boldsymbol{S}^{(B)}(-\omega)\ \boldsymbol{R}_y^{-1}(\pi) \tag{3.21}$$

Because Eq. 3.21 also holds for the inverse elements of $\boldsymbol{S}^{(A)}(\omega)$ and $\boldsymbol{S}^{(B)}(-\omega)$, using Eq. 3.31 we can write

$$\overline{\boldsymbol{S}^{(B)}}^{tr}(-\omega) = \boldsymbol{R}_y(\pi)\ (\boldsymbol{S}^{(B)}(-\omega))^{-1}\ \boldsymbol{R}_y^{-1}(\pi) = (\boldsymbol{S}^{(A)}(\omega))^{-1}. \tag{3.22}$$

For an ideal S$^2$-COOP pulse which acts symmetric with respect to $\omega$ (Eqs. 3.19 and 3.20) the above relation becomes

$$\overline{\boldsymbol{S}^{(B)}}^{tr}(\omega) = (\boldsymbol{S}^{(A)}(\omega))^{-1}, \tag{3.23}$$

A direct consequence of Eq. 3.23 is that in Eq. 3.4 $\alpha^{(A)} = -\alpha^{(B)}$. Therefore, for the cases where the pulse shapes of A and B obey the symmetry rule of Eq. 3.16 and Eqs. 3.19 and 3.20, the optimization algorithm converges to pulses where pulse 2 is the inverse of pulse 1, which is, however, not a necessary condition for S$^2$-COOP pulses.

### Pseudo-S$^2$-COOP pulses

The pulse symmetry we observed for some of our optimized pulses (cf. Eq. 3.16) can be used to construct symmetric pseudo-S$^2$-COOP pulses from a single optimized pulse (appendix 3.5.9). The symmetry construction of pseudo-S$^2$-COOP pulses A and B can be summarized as follows:

- Optimize a pulse A that starting from $M_z$ maximizes transverse magnetization. The magnetization phase $\varphi(\omega)$ must be the sum of a symmetric term $s(\omega)$ and a linear term $RT\omega$

  $$\varphi(\omega) = s(\omega) + RT\omega, \tag{3.24}$$

  where $s(\omega) = s(-\omega)$.
- Create pulse B by inverting the $x$ control of pulse A.

Like for the original S$^2$-COOP approach any pulse A or B can be used as the first pulse of the sequence whereas the counterpart of this first pulse (B or A) has to be time-reversed and phase-inverted to yield the second pulse of the frequency-labeling sequence.

In order to find a pulse with optimal $R$, we implemented a dynamic target optimization scheme where $R$ is variable (cf. appendix 3.5.9). We were able to obtain a pulse with $R = 0.531$ and $\Phi_b = 0.99633$. A corresponding optimization of an S$^2$-COOP pulse with equal $R$ gave a pulse pair with $\Phi_b = 0.99643$ which is slightly better than the single pulse. The S$^2$-COOP pulse pair approximately obeys the symmetry relation of Eq. 3.16. The transverse magnetization profile at the end of each pulse is almost identical and has values above 0.9975 for the entire offset range of 70 kHz. The difference in quality mainly translates to a difference in phase errors: The $S^2$-COOP pulse pair keeps the phase error smaller then 1° whereas the single pulse produces phase errors up to slightly less than 2°. Here, we demonstrated that it is possible to construct pseudo-$S^2$-COOP pulses where the optimization of only a single pulse is necessary. However, the imposed symmetry represents an unnecessary restriction which might in turn lead to reduced fidelity with respect to the more general $S^2$-COOP pulses.

Earlier, we had optimized a saturation pulse using the performance function

$$\Phi_{sat} = 1 - M_z^2(T) \tag{3.25}$$

with the same specification as for the $S^2$-COOP pulses. The optimization produced a high-quality pulse with $\Phi_{sat} = 0.99670$. We noticed the striking similarity of the pulse shape of the conventional saturation pulse and the $S^2$-COOP pulses with $R = 0.5$. Upon application of the symmetry rule defined in Eq. 3.16, a second pulse could be constructed so that two pulses A and B were obtained similar to the $S^2$-COOP procedure. This pulse pair was also evaluated for various values of $R$ using $\Phi_b$ as a quality measure. For $R = 0.529$ this constructed pulse pair performed almost as well as the equivalent $S^2$-COOP analogues. (The values of $\Phi_b$ were 0.99373 (saturation, black cross in Fig. 3.6) vs. 0.99645 ($S^2$-COOP).) We found that this pulse approximately fulfills Eq. 3.24: By optimizing a saturation pulse we found a pseudo-$S^2$-COOP pulse by chance. We optimized a further saturation pulse using $\Phi_{sat}$ for different parameters. Although this pulse is a high-quality saturation pulse ($\Phi_{sat} = 0.99682$) it does not obey Eq. 3.24 and we were not able to generate a $S^2$-COOP pulse pair with acceptable performance. This confirms our finding that conventional saturation pulses cannot in general be used as an alternative to $S^2$-COOP pulses.

In Fig. 3.3 we show the set of admissible effective rotation vectors $\boldsymbol{r}$ of an ideal $S^2$-COOP pulse pair which forms a two-dimensional plane of revolution. In Fig. 3.8 we compare this set of admissible effective rotation vectors with the calculated effective rotation vectors of an optimized $S^2$-COOP pulse ($R = 0.529$). For better clarity, in Fig. 3.8 we do not show the three-dimensional information (like in Fig. 3.3) but merged the $r_x$ and $r_y$ components of $\boldsymbol{r}$ to a single transverse component $r_\perp = \sqrt{r_x^2 + r_y^2}$. As we expected, the effective rotation vectors of this high-quality pulse lie on or very close to the predicted curve.

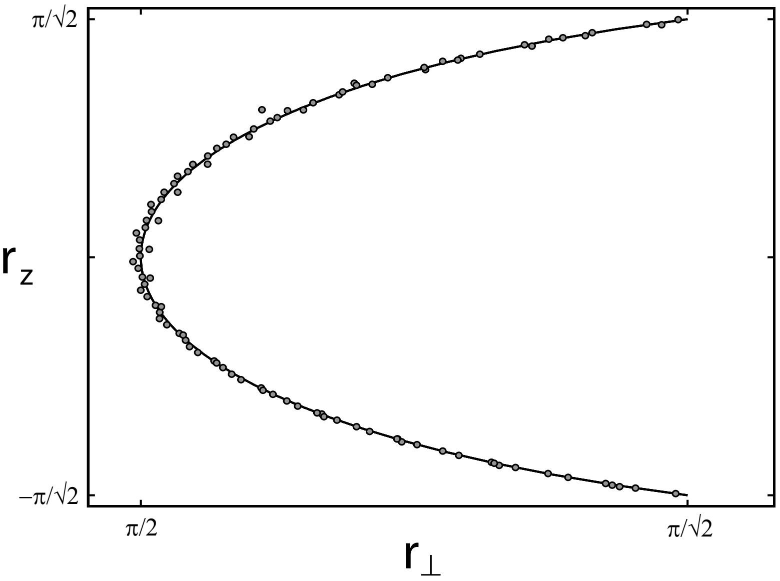

Figure 3.8: In Fig. 3.3 we showed the set of all admissible rotation vectors for a S$^2$-COOP (or saturation) pulse as a gray surface. Here, the generatrix of this surface of revolution is displayed as a black curve. Projections of the effective rotation vectors $\boldsymbol{r}(\omega)$ on a plane are shown as black circles ($r_\perp = \sqrt{(r_x^2 + r_y^2)}$). We used the S$^2$-COOP pulse with $R = 0.529$ (cf. Fig. 3.6) and calculated 101 equally distributed points for the entire considered offset range of 70 kHz.

### $^{13}$C–$^{13}$C NOESY experiments using S$^2$-COOP pulses

The quality factor $\Phi_b$ for the ICEBERG pulses was best at $R = 0.6$ ($\Phi_b = 0.87572$). For the corresponding S$^2$-COOP pulse pair ($R = 0.6$) the quality factor is still – although slightly smaller – very close to the optimum value at $R = 0.529$ (0.99598 vs. 0.99645). We selected these pulses at $R = 0.6$ and a pair of rectangular pulses for a comparison of the conventional approach and the new S$^2$-COOP pulses in order to illustrate that even where the performance of conventional ICEBERG pulses is best, the S$^2$-COOP approach is far superior to the classical method.

Two-dimensional $^{13}$C–$^{13}$C NOESY experiments were performed on a Bruker AV III 600 spectrometer using a sample of $^{13}$C-labelled $\alpha$-D-glucose in DMSO which was chosen as a solvent in order to avoid mutarotation [65]. We used the $^{13}$C–$^{13}$C NOESY pulse sequence from [64] where the unnecessary $^{15}$N-decoupling pulses were omitted. Due to large undesired contributions originating from zero-quantum coherences we added a swept pulse/gradient pair for zero-quantum suppression [66]. A schematic drawing of the pulse sequence is displayed in Fig. 3.12 . The original pulse durations and maximum rf amplitudes were changed from their original values 25 $\mu$s (rectangular pulses), 75 $\mu$s (ICEBERG and S$^2$-COOP pulses) and 10 kHz to 289.8 $\mu$s, 869.4 $\mu$s and 862.7 Hz in order to reduce the original bandwidth of the optimized pulse (70 kHz) to match the spectral width (6.04 kHz corresponding to 40 ppm). The last pulse of the sequence was a conventional rectangular 90° pulse ($T = 20.5\ \mu s$) which was sufficient for the present experimental conditions. For larger bandwidths, this pulse could be replaced by an optimized broadband excitation pulse [14,16,19,20,22]. The mixing time and recycle delay were set to 50 ms and 280 ms, respectively. The spectra were recorded on a TXI probe at 293 K with 8192 × 512 data points and 16 scans for each increment. Due to the considerable phase slope in F1 the spectra were processed using backward linear prediction (12 data points in $t_1$) in order to reduce base-line roll caused by large first-order phase correction. Processing parameters for both spectra were identical. Selected slices of the $^{13}$C–$^{13}$C NOESY spectra for rectangular, ICEBERG and S$^2$-COOP pulses are shown in Fig. 3.9.

Close to the edges of the considered offset range, the ICEBERG pulse pair produces phase errors larger than 50° in F1. However, for a large portion of the considered offset range, the phase error does not excess an absolute value of 13°. The absolute phase error of the S$^2$-COOP pulses remains below 1.33° for the entire offset range of 70 kHz. This phase error is due to imperfections of the pulse performance: The first pulse of a frequency-labeling sequence excites magnetization with phase $\varphi^{(A)} = \gamma'^{(A)} + RT\omega$. Pulse B, in turn, creates transverse magnetization with phase $\varphi^{(B)} = \gamma'^{(B)} + RT\omega$. Ideally, for S$^2$-COOP pulses with linear phase slope, Eq. 3.3 is fulfilled: $-\gamma'^{(B)} = \gamma'^{(A)}$. However, for non-ideal pulses, the second pulse might pick up the magnetization at the wrong phase so that $-\gamma'^{(B)} = \gamma'^{(A)} + \Delta\varphi$. Thus,

$$\Delta\varphi = -(\gamma'^{(A)} + \gamma'^{(B)}) \tag{3.26}$$

is the phase error we observe in F1. For both ICEBERG and S$^2$-COOP pulses $\Delta\varphi$ is plotted as black curves in Fig. 3.10. One-dimensional slices at constant F1 were extracted from the spectra and phase-corrected manually using zero-order phase correction. The corresponding values for the phase errors are represented as squares in Fig. 3.10. There is a reasonable match of calculated and experimental values. A synopsis of the performances of UR, PP, ICEBERG and S$^2$-COOP pulses for $R = 0$ and $R \neq 0$ is shown in Fig. 3.11. The results shown in the figures 3.9, 3.10 and 3.11 clearly demonstrate the superiority of the S$^2$-COOP approach compared to the conventional method of pulse optimization.

## 3.4 Discussion and conclusion

Here, we introduced the concept of S$^2$-COOP pulses that are optimized simultaneously and act in a cooperative way at different positions in a single scan. The S$^2$-COOP approach is a modification of the cooperative pulse concept for several scans presented in chapter 2 and in [49]. With the help of generalized optimal control based algorithms, such as the presented variant of the GRAPE (gradient ascent pulse engineering) algorithm, S$^2$-COOP pulses can be efficiently optimized.

For simplicity, here, we focused on the example of a frequency-labeling sequence for NOESY-type experiments which is an important building block of many multi-dimensional NMR experiments. Frequency-labeling sequences can be designed using standard stand-alone PP$_{z\rightarrow x}$ and ICEBERG pulses. The goal of such pulses is to steer initial $z$ magnetization to one defined final state where this final state can be constant (PP) or offset-dependent (ICEBERG). However, between the first and second pulses of a frequency-labeling sequence the magnetization may be located anywhere in the transverse plane. Here, we showed how this additional degree of freedom can be exploited in order to design improved frequency-labeling sequences. In addition, we were

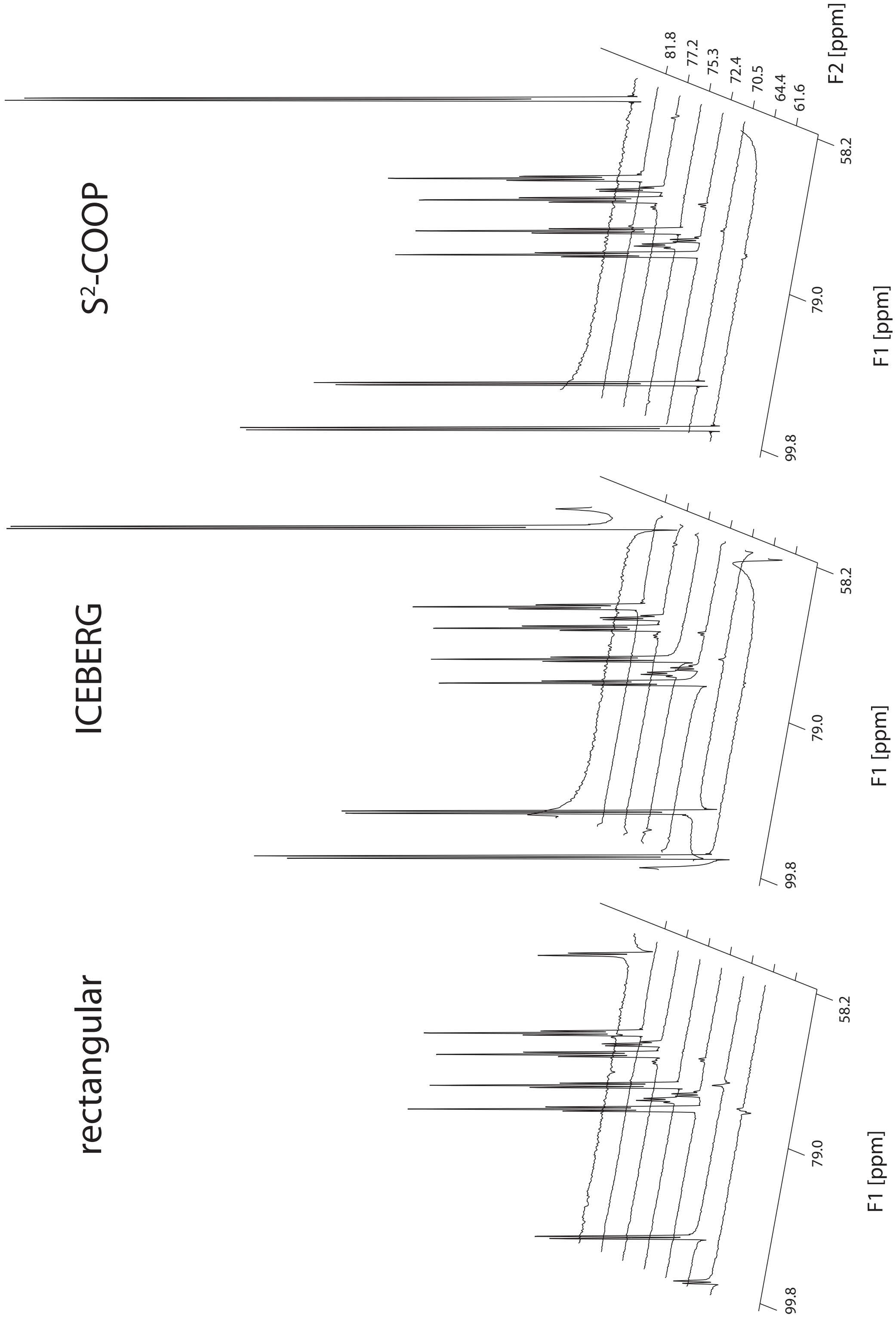

Figure 3.9: Selected slices from 2D NOESY spectra of $^{13}$C-labelled $\alpha$-D-glucose in DMSO.

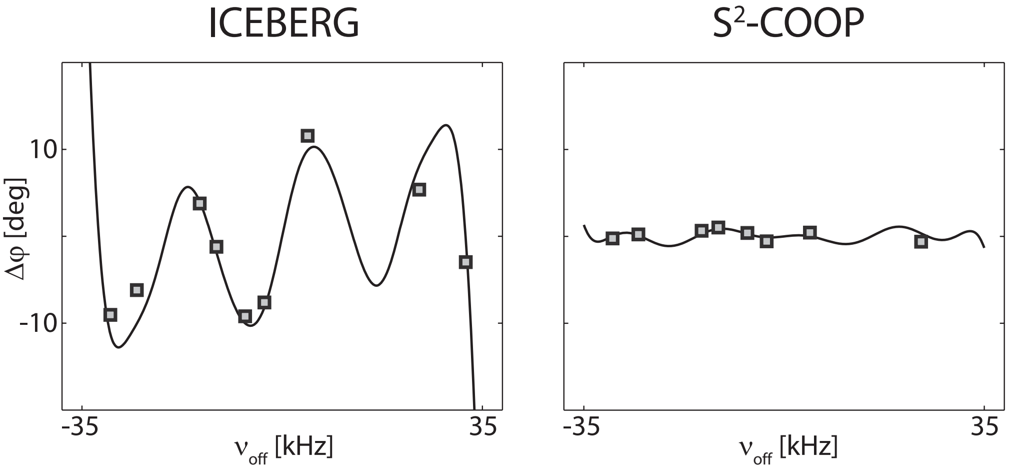

Figure 3.10: Calculated (straight line) and experimental (squares) phase errors $\Delta\varphi$ vs. $\nu_{off} = \omega/2\pi$ of ICEBERG and S$^2$-COOP pulses with $R = 0.6$ are shown. Experimental values were taken from a 2D NOESY spectrum of $^{13}$C-labelled $\alpha$-D-glucose in DMSO. This figure represents an enlarged view of the plots in Fig. 3.11 marked with an asterisk.

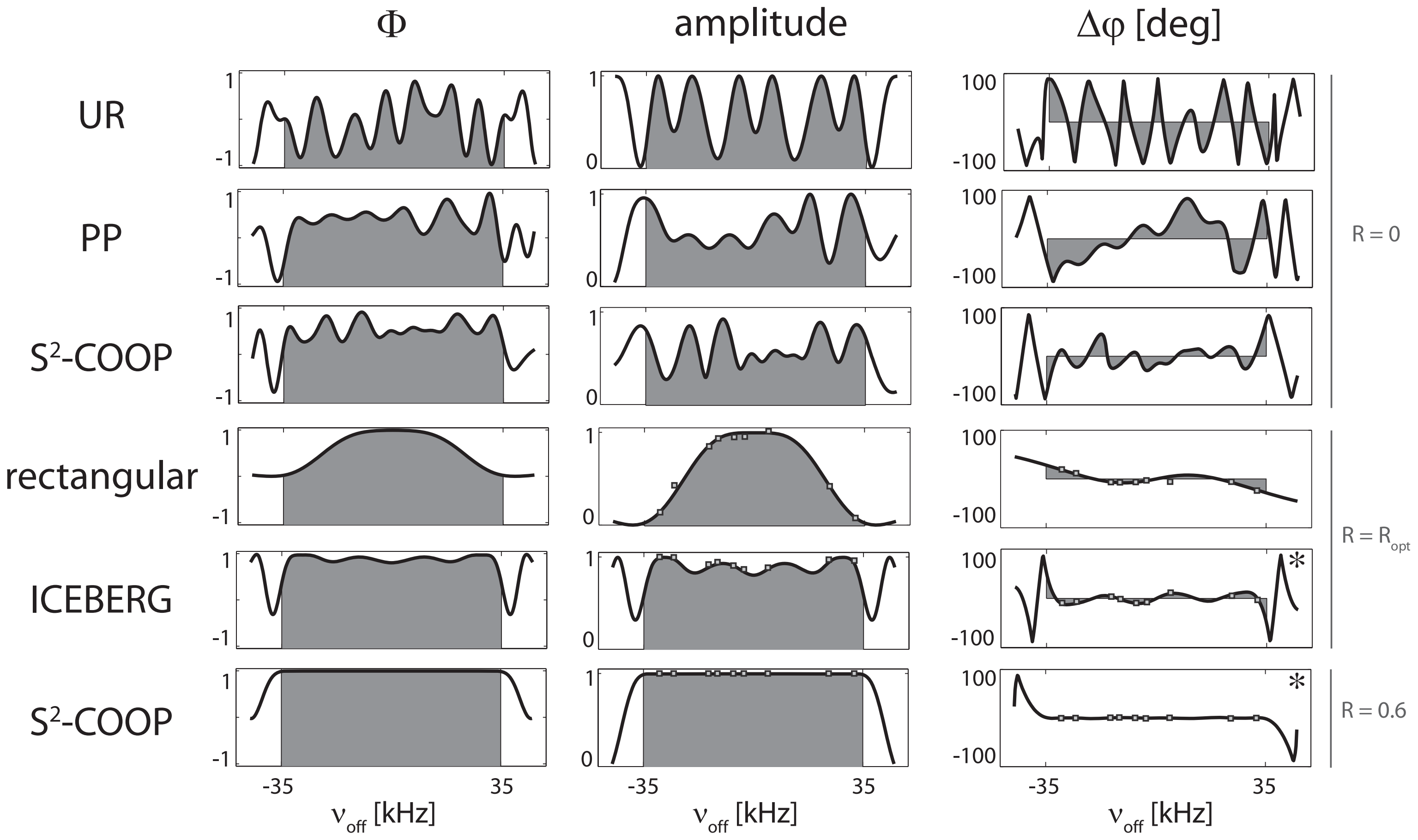

Figure 3.11: Comparison of the quality factors $\Phi_a$ and $\Phi_b$ (left), the signal amplitude (center) and the phase error in F1, $\Delta\varphi$ (right) for different frequency-labeling sequences using 75 $\mu$s pulses. Optimized universal rotation (UR), point-to-point (PP) and S$^2$-COOP pulses are compared in the upper half, where for each case $R = 0$. In the lower half, we show the results of a rectangular pulse ($R_{opt} = 0.567$), an ICEBERG pulse ($R_{opt} = 0.6$) and a S$^2$-COOP pulse pair ($R = 0.6$). The phase errors in F1 are shown after linear phase correction corresponding to the respective values for $R$. The offset range of 70 kHz that was considered in the optimization is indicated by a gray shading. Experimental values are displayed as squares and were extracted from the 2D NOESY spectra which are in part shown in Fig. 3.11. An enlarged view of the plots marked with asterisks is shown in Fig. 3.10.

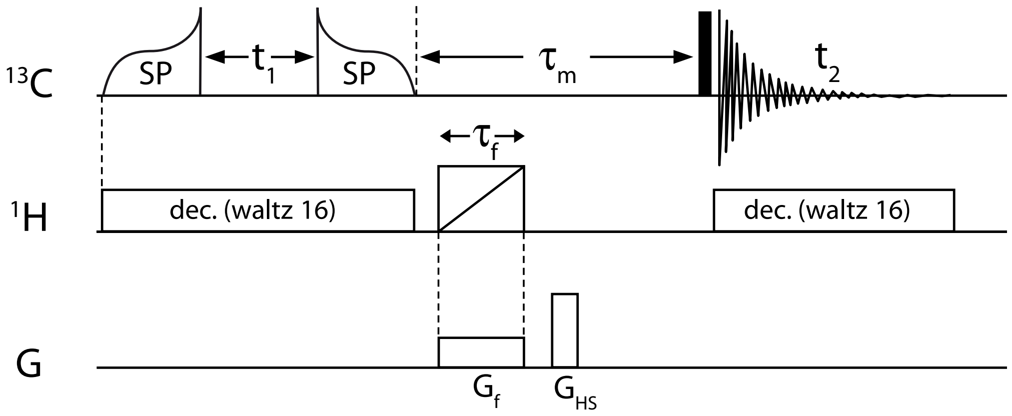

Figure 3.12: Pulse sequence for the zero-quantum filtered $^{13}$C–$^{13}$C NOESY experiment. Radio-frequency pulses are shown on the lines marked $^{13}$C and $^{1}$H. The filled-in rectangle specifies a rectangular 90° pulse. Shaped pulses are indicated by a smooth curve and the letters SP. The chirped inversion pulse is indicated by an open box containing a diagonal line. Gradient pulses are shown on the line marked G. $G_{HS}$ denotes a homospoil gradient pulse, $G_f$ the weak gradient of the zero-quantum filter [66].

able to derive an alternative method for the optimization of pulses for frequency-labeling sequences that involves the optimization of only a single pulse. However, this method imposes unnecessary restrictions to the optimization which might impair the pulse performance. In both simulations and experiments $S^2$-COOP pulse pairs achieve improved results with respect to conventional pulses (section 3.3). However, it is important to note that, apart from frequency-labeling, the $S^2$-COOP approach can also be applied to other problems, like INEPT-steps [52, 62] and Ramsey experiments [53]. In principle, the very $S^2$-COOP pulses presented in this chapter could be employed for such experiments.

So far, optimal control based techniques for the efficient optimization of rf pulses were restricted to single steps. The $S^2$-COOP approach lifts this restriction to single transfers and thus opens up new avenues on the way to global pulse sequence optimizations. We hope that the presented $S^2$-COOP approach will find practical applications in NMR spectroscopy and imaging.

## 3.5 Appendix

### 3.5.1 Conversion of a PP$_{z\to x}$ to a PP$_{x\to z}$ pulse

We consider an ensemble of uncoupled spin ½ particles without relaxation which can be described by the Bloch equations:

$$\dot{\boldsymbol{M}}(t) = \boldsymbol{A}\ \boldsymbol{M}(t) = \begin{pmatrix} 0 & -\omega & \omega_y \\ \omega & 0 & -\omega_x \\ -\omega_y & \omega_x & 0 \end{pmatrix} \boldsymbol{M}(t). \tag{3.27}$$

If $\boldsymbol{\omega} = (\omega_x,\ \omega_y,\ \omega)^\top$ is constant during $\Delta t$ the solution is

$$\boldsymbol{M}(t+\Delta t) = \mathrm{e}^{\Delta t \boldsymbol{A}}\ \boldsymbol{M}(t) = \boldsymbol{R}\ \boldsymbol{M}(t). \tag{3.28}$$

$\boldsymbol{R}$ is a rotation matrix acting on $\boldsymbol{M}(t)$. Shaped pulses are in practice realized as a sequence of $N$ piecewise-constant rectangular pulses with duration $\Delta t$. Therefore, the effect of a shaped pulse on a magnetization vector can be described by sequentially rotating the initial magnetization vector $\boldsymbol{M}(0)$ for all $\boldsymbol{\omega}_j$ with $j$ ranging from 1 to $N$. The sequence of rotation matrices can be grouped together to yield an effective rotation matrix $\boldsymbol{S}(\omega)$:

$$\boldsymbol{M}(T) = (\boldsymbol{R}_N \boldsymbol{R}_{N-1}\ ...\ \boldsymbol{R}_j\ ...\ \boldsymbol{R}_2 \boldsymbol{R}_1)\ \boldsymbol{M}(0) = \boldsymbol{S}(\omega)\boldsymbol{M}(0). \tag{3.29}$$

$\boldsymbol{S}(\omega)$ can be described by a Euler angle decomposition in the $zyz$ fixed-frame convention:

$$\boldsymbol{S}(\omega) = \boldsymbol{R}_z(\gamma)\boldsymbol{R}_y(\beta)\boldsymbol{R}_z(\alpha), \tag{3.30}$$

It has been shown before that the transformation performed by a phase inverted ($\overline{\boldsymbol{S}}$) and time reversed ($\boldsymbol{S}^{tr}$) pulse is the inverse of the original transformation rotated by $\pi$ about the $y$ axis (Eq. 6 from [23]):

$$\begin{aligned} \overline{\boldsymbol{S}}^{tr}(\omega) &= \boldsymbol{R}_y(\pi)\ \boldsymbol{S}^{-1}(\omega)\ \boldsymbol{R}_y^{-1}(\pi) \\ &= \boldsymbol{R}_y(\pi)\ \left[\boldsymbol{R}_z(\gamma)\ \boldsymbol{R}_y(\beta)\ \boldsymbol{R}_z(\alpha)\right]^{-1}\ \boldsymbol{R}_y^{-1}(\pi) \\ &= \boldsymbol{R}_y(\pi)\ \boldsymbol{R}_z^{-1}(\alpha)\ \boldsymbol{R}_y^{-1}(\beta)\ \boldsymbol{R}_z^{-1}(\gamma)\ \boldsymbol{R}_y^{-1}(\pi) \\ &= \left[\boldsymbol{R}_y(\pi)\boldsymbol{R}_z^{-1}(\alpha)\boldsymbol{R}_y^{-1}(\pi)\right]\ \boldsymbol{R}_y^{-1}(\beta)\ \left[\boldsymbol{R}_y(\pi)\boldsymbol{R}_z^{-1}(\gamma)\boldsymbol{R}_y^{-1}(\pi)\right] \\ &= \boldsymbol{R}_z(\alpha)\ \boldsymbol{R}_y(-\beta)\ \boldsymbol{R}_z(\gamma) \end{aligned} \tag{3.31}$$

In the second line $\boldsymbol{S}^{-1}(\omega)$ was replaced using Eq. 3.30. In the third line, simple matrix algebra was used: $(\boldsymbol{ABC})^{-1} = \boldsymbol{C}^{-1}\boldsymbol{B}^{-1}\boldsymbol{A}^{-1}$. Then we multiplied with a unity matrix $\mathbb{1} = \boldsymbol{R}_y^{-1}(\pi)\ \boldsymbol{R}_y(\pi)$ in the fourth line and exchanged the commuting operators $\boldsymbol{R}_y^{-1}(\beta)$ and $\boldsymbol{R}_y^{-1}(\pi)$. In the last line we applied the resulting $\pi_y$-rotation on $\boldsymbol{R}_z^{-1}(\alpha)$ and $\boldsymbol{R}_z^{-1}(\gamma)$ yielding $\boldsymbol{R}_z(\alpha)$ and $\boldsymbol{R}_z(\gamma)$, respectively. Thus, we obtained the same result as in Eq. 3.30 with the difference that $\beta$ has changed sign and $\alpha$ and $\gamma$ have changed places.

For an ideal $\mathrm{PP}_{z\to x}$ pulse $\beta = \pi/2$ and $\gamma = 0$ so that upon time-reversal and phase-inversion we obtain

$$\begin{aligned} \overline{\boldsymbol{S}}^{tr}_{z\to x}(\omega) &= \boldsymbol{R}_z(\alpha)\ \boldsymbol{R}_y(-\pi/2) \\ &= \boldsymbol{S}_{x\to z}(\omega). \end{aligned}$$

The $(-\pi/2)_y$-rotation transforms $\boldsymbol{M}_x$ to $\boldsymbol{M}_z$ upon which the $\alpha_z$-rotation has no effect. Thus we have obtained the desired transformation from $x$ to $z$.

### 3.5.2 Relations between the effective rotation matrices of symmetric S$^2$-COOP and pseudo-S$^2$-COOP pulse pairs

The controls of some S$^2$-COOP and all pseudo-S$^2$-COOP pulse pairs A and B fulfill Eq. 3.16:

$$\varphi^{(B)} = -\varphi^{(A)} + \pi,$$

which is equivalent to a rotation of the controls by $\pi$ about the $y$ axis. In terms of the $x$ and $y$ components of $\boldsymbol{\omega}$, this relation corresponds to $\omega_x^{(A)} = -\omega_x^{(B)}$ and $\omega_y^{(A)} = \omega_y^{(B)}$. Then, the rotation matrix at the $j$-th increment of pulse A can be written as

$$\begin{aligned} \boldsymbol{R}_j^{(A)}(\omega) = &\quad \exp\left\{ \Delta t \begin{pmatrix} 0 & -\omega & \omega_y^{(A)} \\ \omega & 0 & -\omega_x^{(A)} \\ -\omega_y^{(A)} & \omega_x^{(A)} & 0 \end{pmatrix} \right\} \\ = &\quad \exp\left\{ \Delta t \begin{pmatrix} 0 & -\omega & \omega_y^{(B)} \\ \omega & 0 & \omega_x^{(B)} \\ -\omega_y^{(B)} & -\omega_x^{(B)} & 0 \end{pmatrix} \right\} \end{aligned}$$

$$
\begin{aligned}
&= \exp\left\{\Delta t\ \boldsymbol{R}_y(\pi) \begin{pmatrix} 0 & \omega & \omega_y^{(B)} \\ -\omega & 0 & -\omega_x^{(B)} \\ -\omega_y^{(B)} & \omega_x^{(B)} & 0 \end{pmatrix} \boldsymbol{R}_y^{-1}(\pi)\right\} \\
&= \boldsymbol{R}_y(\pi)\ \boldsymbol{R}_j^{(B)}(-\omega)\ \boldsymbol{R}_y^{-1}(\pi), \qquad (3.32)
\end{aligned}
$$

where in the last line we used the fact that $R_y(\pi)$ is orthogonal: For any orthogonal (or unitary) matrix $\boldsymbol{V}$ we can write $\exp\{\boldsymbol{V}\boldsymbol{A}\boldsymbol{V}^{-1}\} = \boldsymbol{V}\ \exp\{\boldsymbol{A}\}\ \boldsymbol{V}^{-1}$,which is a general result from matrix algebra.
The effective rotation matrix of pulse A is

$$
\begin{aligned}
\boldsymbol{S}^{(A)}(\omega) =& \boldsymbol{R}_N^{(A)}(\omega)\ldots\boldsymbol{R}_j^{(A)}(\omega)\ldots\boldsymbol{R}_1^{(A)}(\omega) \\
=& \boldsymbol{R}_y(\pi)\boldsymbol{R}_N^{(B)}(-\omega)\boldsymbol{R}_y^{-1}(\pi)\ldots\boldsymbol{R}_y(\pi)\boldsymbol{R}_j^{(B)}(-\omega)\boldsymbol{R}_y^{-1}(\pi)\ldots \\
& \times \boldsymbol{R}_y(\pi)\boldsymbol{R}_1^{(B)}(-\omega)\boldsymbol{R}_y^{-1}(\pi) \qquad (3.33) \\
=& \boldsymbol{R}_y(\pi)\ \left[\boldsymbol{R}_N^{(B)}(-\omega)\ldots\boldsymbol{R}_j^{(B)}(-\omega)\ldots\boldsymbol{R}_1^{(B)}(-\omega)\right]\ \boldsymbol{R}_y^{-1}(\pi) \\
=& \boldsymbol{R}_y(\pi)\ \left[\boldsymbol{S}^{(B)}(-\omega)\right]\ \boldsymbol{R}_y^{-1}(\pi),
\end{aligned}
$$

which is the relation we used in Eq. 3.21.

### 3.5.3 Theoretical description of selected frequency-labeling sequences

Here, we describe the effect of various frequency-labeling sequences using the *zyz*-Euler angle decomposition of the effective rotation matrices of the pulses (Eq. 3.30). Corresponding drawings are given in Fig. 3.2.

### 3.5.4 Universal rotations

The UR pulses of this sequence perform rotations about the $y$ axis:

$$90^\circ_y:\ \boldsymbol{S}(\omega) = \boldsymbol{R}_y(\pi/2) \qquad -90^\circ_y:\ \boldsymbol{S}(\omega) = \boldsymbol{R}_y(-\pi/2).$$

Chemical shift evolution during $t_1$ corresponds to a $z$-rotation by an angle $\omega t_1$:

$$\begin{aligned} &\boldsymbol{R}_y(-\pi/2)\ \boldsymbol{R}_z(\omega t_1)\ \boldsymbol{R}_y(\pi/2)\ \boldsymbol{M}_z = \\ &\quad = \boldsymbol{R}_y(-\pi/2)\ \boldsymbol{R}_z(\omega t_1)\ \boldsymbol{M}_x \\ &\quad = \boldsymbol{R}_y(-\pi/2)\ \big(\boldsymbol{M}_x \cos(\omega t_1) + \boldsymbol{M}_y \sin(\omega t_1)\big) \\ &\quad = \boldsymbol{M}_z \cos(\omega t_1) + \boldsymbol{M}_y \sin(\omega t_1). \end{aligned} \tag{3.34}$$

### 3.5.5 Point-to-point transformations

Now we consider the case where the two UR pulses are replaced by PP pulses.

$$\begin{aligned} &\overline{\boldsymbol{S}}^{tr}_{z\to x}(\omega)\ \boldsymbol{R}_z(\omega t_1)\ \boldsymbol{S}_{z\to x}(\omega)\boldsymbol{M}_z = \\ &\quad = \boldsymbol{R}_z(\alpha)\boldsymbol{R}_y(-\pi/2)\boldsymbol{R}_z(\omega t_1)\boldsymbol{R}_y(\pi/2)\boldsymbol{R}_z(\alpha)\ \boldsymbol{M}_z \\ &\quad = \boldsymbol{R}_z(\alpha)\boldsymbol{R}_y(-\pi/2)\boldsymbol{R}_z(\omega t_1)\ \boldsymbol{M}_x \\ &\quad = \boldsymbol{R}_z(\alpha)\boldsymbol{R}_y(-\pi/2)\ \big(\boldsymbol{M}_x \cos(\omega t_1) + \boldsymbol{M}_y \sin(\omega t_1)\big) \\ &\quad = \boldsymbol{M}_z \cos(\omega t_1) + \boldsymbol{R}_z(\alpha)\ \big(\boldsymbol{M}_y \sin(\omega t_1)\big) \end{aligned} \tag{3.35}$$

After the PP$_{x\to z}$ pulse we obtain the desired $\cos(\omega t_1)$-modulated $z$ magnetization plus a term $\boldsymbol{R}_z(\alpha)\ \big(\boldsymbol{M}_y \sin(\omega t_1)\big) = \big(\boldsymbol{M}_y \sin(\omega t_1)\big)\cos(\alpha) - (\boldsymbol{M}_x \sin(\omega t_1))\sin(\alpha)$ which represents transverse magnetization being removed by coherence transfer pathway selection [45–47]. Because $\alpha$ may take any value, the last line of Eq. 3.35 defines the set of admissible magnetization vectors which is drawn as a cone on the rightmost drawing of the PP-sequence in Fig. 3.2

### 3.5.6 Point-to-point transformations with linear phase slope

Now we consider the case of an excitation pulse with linear phase slope [21]. Using the Euler angle decomposition from Eq. 3.30 we can write $\gamma = RT\omega$ where $R$ is the fraction of the pulse duration $T$ during which chemical shift is active. In the frequency-labeling sequence, the first pulse creates transverse magnetization with linear phase slope, i.e. $\boldsymbol{M}_x \cos(RT\omega) + \boldsymbol{M}_y \sin(RT\omega) = \boldsymbol{R}_z(RT\omega)\ \boldsymbol{M}_x$. At $t_1 = 0$ the time-reversed and phase-inverted pulse performs the rotation sequence

$\boldsymbol{R}_z(\alpha)\boldsymbol{R}_y(-\pi/2)\ \boldsymbol{R}_z(RT\omega)$ (Eq. 3.31) and we obtain:

$$\begin{aligned} \boldsymbol{R}_z(\alpha)\boldsymbol{R}_y(-\pi/2)\boldsymbol{R}_z(RT\omega)\ \boldsymbol{R}_z(RT\omega)\boldsymbol{M}_x &= \\ \boldsymbol{R}_z(\alpha)\boldsymbol{R}_y(-\pi/2)\ \boldsymbol{R}_z(\underbrace{2RT}_{t_1^{min}}\omega)\boldsymbol{M}_x & \end{aligned} \tag{3.36}$$

which corresponds to the above result for $\mathrm{PP}_{z\rightarrow x}$ pulses with the difference that $t_1$ has been replaced by $2RT$. Therefore, when a frequency-labeling sequence consisting of an excitation pulse with linear phase slope followed by its time-reversed and phase-inverted counterpart is applied, the effective evolution time $\tau$ does not correspond to the inter-pulse delay $t_1$ (cf. Fig. 3.1):

$$\tau = t_1 + 2RT \tag{3.37}$$

In a two-dimensional Fourier-transformed NOESY spectrum this results in a linear phase error with respect to F1 which can be phase-corrected by first-order phase correction. For larger values of $RT$ first-order phase correction will lead to a rolling base-line. This problem can be alleviated by applying backward linear prediction.

### 3.5.7 Single-scan cooperative pulses

Single-scan cooperative pulses create transverse magnetization with opposite phase, i.e. $\varphi^{(A)} = -\varphi^{(B)}$. In other words, the final Euler rotation angles ($\gamma$ in Eq. 3.30) about $z$ are of opposite sign:

$$\begin{aligned} \boldsymbol{S}^{(A)}(\omega) &= \boldsymbol{R}_z(\gamma)\boldsymbol{R}_y(\pi/2)\boldsymbol{R}_z(\alpha^{(A)}) \\ &\text{and} \\ \boldsymbol{S}^{(B)}(\omega) &= \boldsymbol{R}_z(-\gamma)\boldsymbol{R}_y(\pi/2)\boldsymbol{R}_z(\alpha^{(B)}). \end{aligned} \tag{3.38}$$

In the above equation, $\boldsymbol{S}^{(A)}(\omega)$ and $\boldsymbol{S}^{(B)}(\omega)$ are the effective rotation matrices of two $\mathrm{S}^2$-COOP pulse A and B, respectively. In a frequency-labeling sequence we can directly use one of these pulses as first pulse and its time-reversed and phase-inverted counterpart as second pulse. Here, we use A as the first pulse. The effective rotation matrix of the entire sequence is

$$
\begin{aligned}
&\overline{S^{(B)}}^{tr}(\omega)\boldsymbol{R}_z(\omega t_1)\boldsymbol{S}^{(A)}(\omega) = \\
&= \boldsymbol{R}_z(\alpha^{(B)})\boldsymbol{R}_y(-\pi/2)\boldsymbol{R}_z(-\gamma)\boldsymbol{R}_z(\omega t_1)\boldsymbol{R}_z(\gamma)\boldsymbol{R}_y(\pi/2)\boldsymbol{R}_z(\alpha^{(A)}) \\
&= \boldsymbol{R}_z(\alpha^{(B)})\boldsymbol{R}_y(-\pi/2)\boldsymbol{R}_z(\omega t_1)\boldsymbol{R}_y(\pi/2)\boldsymbol{R}_z(\alpha^{(A)}).
\end{aligned}
\tag{3.39}
$$

The rotations $\boldsymbol{R}_z(\gamma)$ and $\boldsymbol{R}_z(-\gamma)$ cancel: The pair of S$^2$-COOP pulses acts in a cooperative way such that the two pulses cancel each other's imperfections. The above result is equivalent to the result for PP pulses (appendix 3.5.5). However, allowing an additional arbitrary rotation $\boldsymbol{R}(\gamma)$ adds an additional degree of freedom to S$^2$-COOP pulses with respect to PP pulses.

When using S$^2$-COOP pulses with linear phase slope the effective rotation matrices are

$$
\begin{aligned}
\boldsymbol{S}^{(A)}(\omega) &= \boldsymbol{R}_z(\gamma^{(A)})\boldsymbol{R}_y(\pi/2)\boldsymbol{R}_z(\alpha^{(A)}) \\
&= \boldsymbol{R}_z(\gamma' + RT\omega)\boldsymbol{R}_y(\pi/2)\boldsymbol{R}_z(\alpha^{(A)}) \\
&= \boldsymbol{R}_z(\gamma')\boldsymbol{R}_z(RT\omega)\boldsymbol{R}_y(\pi/2)\boldsymbol{R}_z(\alpha^{(A)})
\end{aligned}
\tag{3.40}
$$

and

$$
\begin{aligned}
\boldsymbol{S}^{(B)}(\omega) &= \boldsymbol{R}_z(\gamma^{(B)})\boldsymbol{R}_y(\pi/2)\boldsymbol{R}_z(\alpha^{(A)}) \\
&= \boldsymbol{R}_z(-\gamma' + RT\omega)\boldsymbol{R}_y(\pi/2)\boldsymbol{R}_z(\alpha^{(A)}) \\
&= \boldsymbol{R}_z(-\gamma')\boldsymbol{R}_z(RT\omega)\boldsymbol{R}_y(\pi/2)\boldsymbol{R}_z(\alpha^{(A)}).
\end{aligned}
\tag{3.41}
$$

Again, in a frequency-labeling sequence $\gamma'$ and $-\gamma'$ cancel yielding a result equivalent to excitation pulses with linear phase slope (appendix 3.5.6).

### 3.5.8 Quality factor for S$^2$-COOP pulses with linear phase slope

The first step of the S$^2$-COOP approach comprises the optimization of two pulses that rotate initial $z$ magnetization to the transverse plane. For the case of zero phase slope ($R = 0$), the two resulting transverse magnetization vectors have to be related by a $\pi$-rotation about the $x$ axis (Eq. 3.5):

$$\boldsymbol{M}^{(A)}(T) = \boldsymbol{R}_x(\pi)\boldsymbol{M}^{(B)}(T)$$

If $R \neq 0$ $\boldsymbol{R}_x$ is rotated by $RT\omega$ about $z$ corresponding to a linear phase slope of $RT$. Thus we can write Eq. 3.5 in a generalized form that allows nonzero values for the phase slope:

$$\begin{aligned} \boldsymbol{M}^{(A)}(T) &= \boldsymbol{R}_{RT\omega}(\pi)\boldsymbol{M}^{(B)}(T) \\ &= \left[\boldsymbol{R}_z(RT\omega)\boldsymbol{R}_x(\pi)\boldsymbol{R}_z^{-1}(RT\omega)\right]\ \boldsymbol{M}^{(B)}(T) \end{aligned} \tag{3.42}$$

The quality factor then becomes

$$\begin{aligned} \Phi_b = &\left(M_x^{(A)}(T)M_x^{(B)}(T) - M_y^{(A)}(T)M_y^{(B)}(T)\right) \cdot (C^2 - S^2) \\ &+ 2\left(M_x^{(A)}(T)M_y^{(B)}(T) + M_y^{(A)}(T)M_x^{(B)}(T)\right) \cdot (CS). \end{aligned} \tag{3.43}$$

where we used $C = \cos(RT\omega)$ and $S = \sin(RT\omega)$. Using the relation $\boldsymbol{\lambda}^{(k)}(T) = \partial\Phi/\partial\mathbf{M}^{(k)}(T)$ [16] we obtain the following costate vectors:

$$\boldsymbol{\lambda}^{(A)}(T) \quad = \quad \begin{pmatrix} (C^2 - S^2) \cdot M_x^{(B)}(T) + 2CS \cdot M_y^{(B)}(T) \\ -(C^2 - S^2) \cdot M_y^{(B)}(T) + 2CS \cdot M_x^{(B)}(T) \\ 0 \end{pmatrix} \tag{3.44}$$

and

$$\boldsymbol{\lambda}^{(B)}(T) \quad = \quad \begin{pmatrix} (C^2 - S^2) \cdot M_x^{(A)}(T) + 2CS \cdot M_y^{(A)}(T) \\ -(C^2 - S^2) \cdot M_y^{(A)}(T) + 2CS \cdot M_x^{(A)}(T) \\ 0 \end{pmatrix} \tag{3.45}$$

### 3.5.9 Dynamic target optimization of pseudo-$S^2$-COOP pulses

The offset-profile of the magnetization phase $\varphi(\omega)$ of any pulse can be decomposed into a symmetric part $s(\omega)$ and an antisymmetric part $a(\omega)$:

$$\varphi(\omega) = s(\omega) + a(\omega) = s(\omega) + RT\omega + a'(\omega) \tag{3.46}$$

with $s(\omega) = \frac{1}{2}(\varphi(\omega) + \varphi(-\omega))$ and $a(\omega) = \frac{1}{2}(\varphi(\omega) - \varphi(-\omega))$. The antisymmetric part $a(\omega)$, in turn, can be decomposed to a linear component $RT\omega$ and an antisymmetric, non-linear component $a'(\omega)$. In order to fulfill Eq. 3.24, $a'(\omega)$ has to vanish. Therefore, the goal of the optimization is to minimize $a'(\omega)$.

In a practical optimization, we choose a random pulse shape for which, starting from $z$ magnetization, the offset-profile of the phase of the final magnetization at the end of the pulse $\varphi(\omega)$ is computed. Using the above equations, we derive $s(\omega)$ (which is stored for a step later in the optimization) and $a(\omega)$. Then the radian phase of $a(\omega)$ is unwrapped by subtracting (adding) $2\pi$ from (to) $a(\omega_j + 1)$ if $\big(a(\omega_j + 1) - a(\omega_j)\big)$ is larger (smaller) than $(-)\pi$. Then the slope of the linear, antisymmetric component $RT\omega$ can be extracted by linear regression:

$$RT = \frac{\sum_{j=1}^{n} a(\omega_j)\ \omega_j}{\sum_{j=1}^{n} \omega_j^2} \tag{3.47}$$

Now the target phase $\varphi_t(\omega)$ is constructed according to Eq. 3.24:

$$\varphi_t(\omega) = s(\omega) + RT\omega. \tag{3.48}$$

The quality function we use is $\Phi_0 = 1 - (T_x - M_x(T))^2 - (T_y - M_y(T))^2 - M_z(T)^2$ (Eq. 3.15) where the target magnetization vector is $\boldsymbol{T} = (\cos(\varphi_t)\ \sin(\varphi_t)\ 0)^\top$. The gradients are calculated accordingly and added to the pulse shape. This updated pulse is then used in the next iteration to re-calculate $\varphi_t(\omega)$ in the manner we described above upon which new gradients are added to the pulse shapes. This process is repeated iteratively until a convergence criterion is fulfilled.

The symmetric component of the phase profile $s(\omega)$ may be of any shape (cf. Fig. 3.13). In addition, the value for $R$ is not fixed at the beginning of the optimization and its optimal value is updated in each iteration. Therefore, the dynamic target optimization of pseudo-S$^2$-COOP pulses also optimizes the phase slope $R$.

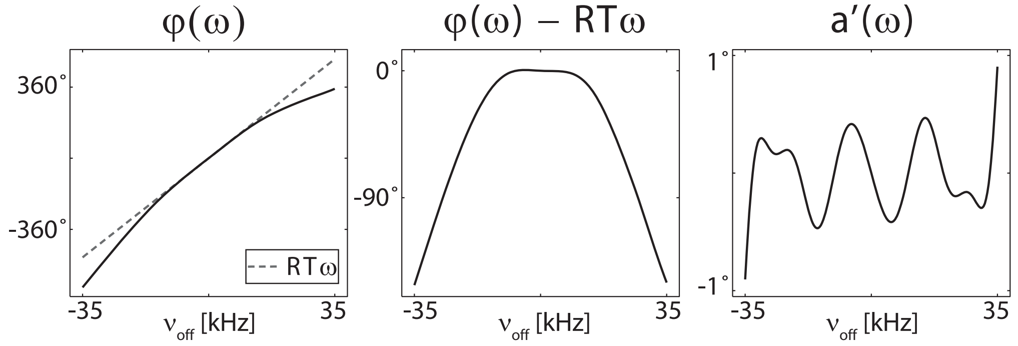

Figure 3.13: The pseudo-$S^2$-COOP pulse with $R = 0.531$ (cf. section 3.3) creates transverse magnetization with phase $\varphi(\omega)$ (left, black curve). For comparison, the linear phase slope $RT\omega$ is plotted as a dashed gray line. The transverse magnetization $M_{\perp} = \sqrt{M_x^2 + M_y^2}$ created by this pulse is larger than 0.9975 for the entire offset range of 70 kHz (data not shown). If the linear component $RT\omega$ is subtracted of $\varphi(\omega)$ the result is approximately symmetric with respect to $\omega$ (center). The antisymmetric, non-linear component $a'(\omega)$ is minimized by the optimization (right).

# 4 Theory of cooperative tracking

In the previous chapters 2 and 3, we showed how COOP pulses can be designed either as COOP cycles which are used for a single transfer in several scans or as $S^2$-COOP pulses which perform different transfers in a single scan. For each case, COOP pulses cancel each other's imperfections and act in a cooperative manner which enables enhanced pulse sequence performances with respect to classical methods of pulse sequence design.

Another method for the design of successive transvers in a single scan is optimal tracking: A desired trajectory of the density matrix (or magnetization vector) at specified points in time is tracked as closely as possible. Optimal tracking has been used for the development of novel low-power heteronuclear decoupling sequences in the liquid state for *in vivo* applications [44]. However, optimal tracking is not limited to the design of decoupling sequences but could in principle be used for the development of various pulse sequences.

In the present chapter, we discuss the theoretical framework of an algorithm which combines the COOP pulse approach with optimal tracking for the design of novel heteronuclear decoupling sequences: During the optimization, we keep track of the density operator at all acquisition points [44] and at the same time we allow for the signal to be the average of several scans [49], i.e. we optimize a set of cooperative heteronuclear decoupling pulses which are in general not identical. We hope that this novel algorithm which we call cooperative tracking will result in improved decoupling sequences, creating spectra with large and uniform signal amplitudes as well as reduced intensities of the decoupling sidebands. In our description of the cooperative tracking algorithm we will redraw the theory of optimal tracking as it is presented in [44].

### Heteronuclear decoupling of two spins ½

Consider the case of a heteronuclear two-spin system with two spins ½ labeled $I$ and $S$. We assume that spin $I$ is observed while spin $S$ is irradiated with a decoupling sequence. The overall Hamiltonian in a doubly rotating frame [67] takes the form

$$\mathcal{H}(t) = \mathcal{H}^{I}_{off} + \mathcal{H}^{S}_{off} + \mathcal{H}^{IS}_{J} + \mathcal{H}^{S}_{rf}(t) \tag{4.1}$$

where

$$\mathcal{H}^{I}_{off} = 2\pi\nu_I I_z \tag{4.2}$$

and

$$\mathcal{H}^{S}_{off} = 2\pi\nu_S S_z \tag{4.3}$$

are the offset terms of spin $I$ and spin $S$, respectively. The heteronuclear $J$ coupling term is

$$\mathcal{H}^{IS}_{J} = 2\pi J S_z I_z. \tag{4.4}$$

The remaining term represents the irradiated decoupling sequence:

$$\mathcal{H}^{S}_{rf}(t) = 2\pi\epsilon\{u_x(t)S_x + u_y(t)S_y\}, \tag{4.5}$$

where the controls $u_x(t)$ and $u_y(t)$ represent the $x$ and $y$ components of the rf field and $\epsilon$ is an rf scaling factor taking rf inhomogeneity and miscalibration into account. Since $\mathcal{H}^{I}_{off}$ commutes with the terms $\mathcal{H}^{S}_{off}$, $\mathcal{H}^{IS}_{J}$ and $\mathcal{H}^{S}_{rf}(t)$ it is sufficient to consider the simplified Hamiltonian

$$\mathcal{H}'(t) = \mathcal{H}^{S}_{off} + \mathcal{H}^{IS}_{J} + \mathcal{H}^{S}_{rf}(t). \tag{4.6}$$

If no decoupling sequence is applied, i.e. $\mathcal{H}^{S}_{rf}(t) = 0$, then the evolution of an initial density operator $\rho(t_0) = I_x$ is only governed by $\mathcal{H}^{IS}_{J}$ because $\mathcal{H}^{S}_{off}$ and $I_x$ commute:

$$\rho(t) = I_x \cos(\pi J t) + 2 I_y S_z \sin(\pi J t). \tag{4.7}$$

Due to the $\cos(\pi J t)$-modulation of the detectable operator $I_x$, the Fourier transformation of the time-domain signal that represents the expectation value $\langle I_x \rangle$ yields a spectrum consisting of a doublet with splitting $J$. The $J$ coupling can be used for different types of experiments, e.g. $J$-resolved spectroscopy [68, 69] and for heteronuclear coherence transfer [52]. However, in many cases it is advantageous to suppress the $J$-coupling evolution. In general, decoupled spectra show fewer peaks than spectra that have been recorded without decoupling which facilitates the analysis of the spectrum [67]. The task of a heteronuclear decoupling sequence is to suppress the effects of $\mathcal{H}_J^{IS}$ so that the doublet collapses to a single line and, in the absence of relaxation effects, $\rho(t) = I_x$ throughout the decoupling sequence. Typically, the time-domain signal is not recorded continuously but only at discrete points in time $T_k$. Therefore, for decoupling it is sufficient that $\rho(t)$ is equal to $I_x$ at the $N_{aq}+1$ acquisition points $T_k$ $(0 \leq k \leq N_{aq})$ which are typically evenly spaced over the acquisition time $T_{aq}$. For the case of non-uniform sampling the position in time of the acquisition points can be adjusted accordingly. So we can write

$$\rho(T_k) = I_x. \tag{4.8}$$

Typically, the dwell-time $\Delta T = T_k - T_{k-1}$ between two acquisition points is longer than the duration $\Delta t = t_m - t_{m-1}$ of an increment of the decoupling sequence, i.e. the discretization of the decoupling sequence is typically finer than the digitization of the detected signal. (Here, $M = \Delta T/\Delta t$ is the number of pulse increments per interval $\Delta T$. The values of $\Delta T$ and $\Delta t$ are chosen such that $M$ is an integer.)

In analogy to COOP pulses in several scans (Chapter 2), we try to optimize a set of $N$ decoupling pulses that are in general not identical. Hence, the entire COOP decoupling cycle consists of $N$ pulse sequences. Each of the latter consists of $N_{aq}M$ pulse increments and is characterized by control amplitudes $u_x^{(n)}(j)$ and $u_y^{(n)}(j)$ with $1 \leq j \leq N_{aq}M$ and $1 \leq n \leq N$. The overall signal $\overline{s_k}$ is obtained by averaging the $N$ signals $s_k^{(n)}$ that are obtained in $N$ scans where we cycle through the entire set of $N$ COOP decoupling sequences:

$$\begin{aligned}\overline{s_k} &= \frac{1}{N}\sum_{n=1}^{N} s_k^{(n)} \\ &= \frac{1}{N}\sum_{n=1}^{N} \langle I_x|\rho^{(n)}(T_k)\rangle \\ &= \langle I_x|\frac{1}{N}\sum_{n=1}^{N} \rho^{(n)}(T_k)\rangle \\ &= \langle I_x|\overline{\rho}(T_k)\rangle\end{aligned} \tag{4.9}$$

with

$$\langle I_x\,|\,\overline{\rho}(T_k)\rangle = \mathrm{tr}\{I_x^{\dagger}\,\overline{\rho}(T_k)\}. \tag{4.10}$$

Although signal averaging cannot increase the amplitude of a decoupled resonance line, it allows for cancelation of undesired signal contributions such as decoupling sidebands and deviations from a desired offset profile. Thus, even if the individual members of a COOP decoupling cycle show imperfections in terms of undesired signal contributions, the COOP tracking algorithm is given the possibility to find solutions where these undesired signals cancel upon signal averaging. A desired offset profile in the context of heteronuclear decoupling can be a maximum and uniform amplitude of the decoupled signal over the entire considered offset range which is of special interest for decoupling sequences in quantitative NMR experiments [70]. Other desired offset profiles can be band-selective decoupling profiles where the decoupling sequence only affects a certain offset range and has no effect for the remaining considered offset frequencies [71,72]. Yet another desired offset profile is a defined, offset-dependent scaling of the coupling constant $J$ as it has been shown in [73].

One method for the reduction of decoupling sidebands in several scans, DESIRE [74], is a two-dimensional NMR technique where the decoupled spectrum corresponds to the slice of the 2D spectrum at $\mathrm{F1} = 0$. The decoupling sidebands appear at $\mathrm{F1} \neq 0$ where the value of F1 corresponds to the splitting of the decoupling sidebands. With DESIRE an up to 100-fold reduction of the decoupling sideband intensities can be achieved. However, in order to obtain a decoupled spectrum with DESIRE, a considerable number of scans in order to sufficiently resolve the spectrum in the indirect dimension is necessary. (In [74] the shown decoupled spectra were recorded with 64 and 128 $t_1$-increments, respectively.) Another method for the reduction of decoupling sidebands in several scans is bi-level decoupling [75]. In bi-level decoupling, several different decoupling sequences are applied in different scans so that decoupling sidebands are cancelled in part upon signal averaging. In the first scan of a bi-level decoupling cycle decoupling is performed with a low rf amplitude (“low-level decoupling”). In all successive scans, a decoupling sequence with high rf amplitude (“high-level decoupling”) is applied at the beginning of the sequence which is followed by a low-level decoupling sequence. The duration of the high-level sequence is increased with each scan. The total signal is obtained by averaging the individual signals from each scan. Thus, it is possible to reduce the intensities of the decoupling sidebands. Bi-level decoupling has been applied to the chemical analysis of polymer compounds [76]. However, the necessary rf amplitudes for high-level decoupling are considerably large. Another disadvantage of bi-level decoupling, especially with respect to quantitative NMR, are the large deviations from a uniform offset profile of the amplitudes of the decoupled signal. A uniform decoupling profile can be obtained when decoupling sequences based on adapted adiabatic pulses are applied [70]. However, in [70] the problem of decoupling sidebands is not addressed and the possibilities that the latter can be reduced by signal averaging is not taken into account. Here, we present the theory of cooperative tracking which is in principle able to find decoupling sequence cycles that create both uniform and maximum decoupled signal amplitudes for the considered offset range and minimize decoupling sidebands.

The amplitude of a decoupled on-resonance signal in the spin $I$ spectrum for a given rf scaling factor $\epsilon$ and offset $\nu_S$ is given by

$$\begin{aligned}\phi(\epsilon,\nu_S) &= \frac{1}{N_{aq}+1}\sum_{k=0}^{N_{aq}} \overline{s_k}(\epsilon,\nu_S) \\ &= \frac{1}{N_{aq}+1}\sum_{k=0}^{N_{aq}} \langle I_x|\overline{\rho}(\epsilon,\nu_S,T_k)\rangle\end{aligned} \tag{4.11}$$

where in the first line we replaced $s_k(\epsilon,\nu_S)$ in Eq. 13 from [44] with $\overline{s_k}(\epsilon,\nu_S)$. In the second line we used the identity from Eq. 4.9.

Here, instead of using the signal amplitude $\phi(\epsilon,\nu_S)$ as the quality factor of a decoupling sequence at a specific rf scaling factor $\epsilon$ and a specific offset frequency $\nu_S$, we choose $\phi'(\epsilon,\nu_S)$ which is

$$\begin{aligned}\phi'(\epsilon,\nu_S) &= \frac{1}{N_{aq}+1}\sum_{k=0}^{N_{aq}} \Big(1-(1-\overline{s_k}(\epsilon,\nu_S))^2\Big) \\ &= \frac{1}{N_{aq}+1}\sum_{k=0}^{N_{aq}} \Big(1-(1-\langle I_x\,|\,\overline{\rho}(\epsilon,\nu_S,T_k)\rangle)^2\Big)\,.\end{aligned} \tag{4.12}$$

This choice assures that full advantage is taken of the COOP pulse principle (cf. Eq. 4.36). We define the overall performance function $\Phi$ of a decoupling sequence as the average of all quality factors $\phi'(\epsilon,\nu_S)$ for all $N_\epsilon$ rf scaling factors and all $N_\nu$ offsets of interest [44]:

$$\Phi = \frac{1}{N_\epsilon N_\nu} \sum_{p=1}^{N_\epsilon} \sum_{q=1}^{N_\nu} \phi' \left( \epsilon^{(p)}, \nu_S^{(q)} \right). \tag{4.13}$$

### Simplified relaxation model

The general analytical expressions for the gradients $\delta\Phi/\delta u_\alpha^{(n)}(j)$ (for $u_\alpha^{(n)}(j) = \epsilon u_x^{(n)}(j)$ and $\epsilon u_y^{(n)}(j)$) can be derived for the case of an arbitrary relaxation matrix. However, a simplified relaxation model where the relevant terms of the density operator relax with the similar rate $\kappa$ reflecting $T_2$ (or $T_2^*$) allows a tremendous simplification of the tracking algorithm. For many cases, this is a reasonable approximation. In the simplified relaxation model, the density operator at time $t_m$ of the $n$th scan is given by

$$\rho^{(n)}(t_m) = \exp\{-\kappa t_m\}\, \widetilde{\rho}^{\,(n)}(t_m) \tag{4.14}$$

and

$$\widetilde{\rho}^{\,(n)}(t_m) = U_m^{(n)} \dots U_1^{(n)}\ \ \rho^{(n)}(t_0)\ \ U_1^{(n)\dagger} \dots U_m^{(n)\dagger}. \tag{4.15}$$

The propagator $U_\mu$ for the $\mu$th time slice of the $n$th scan is given by

$$U_\mu^{(n)} = \exp\{-i\Delta t \mathcal{H}_\mu'^{(n)}\} \tag{4.16}$$

where

$$\mathcal{H}_\mu'^{(n)} = \mathcal{H}_{off}^S + \mathcal{H}_J^{IS} + 2\pi\epsilon \left( u_x^{(n)}(\mu)\, S_x + u_y^{(n)}(\mu)\, S_y \right) \tag{4.17}$$

with $u_x^{(n)}(\mu)$ and $u_y^{(n)}(\mu)$ being the constant control amplitudes during this time slice. Hence, using this simplified relaxation model we can write for the signal amplitude $\overline{s_k}$:

$$\overline{s_k} = \exp\{-\kappa T_k\} \langle I_x | \overline{\rho}(T_k) \rangle. \tag{4.18}$$

where in the context of the simplified relaxation model (Eq. 4.14)

$$\overline{\rho}(T_k) = \frac{1}{N} \sum_{n=1}^{N} \widetilde{\rho}^{\,(n)}(T_k). \tag{4.19}$$

### Derivation of the gradient $\delta\Phi/\delta u_\alpha^{(n)}(j)$

The gradient $\delta\Phi/\delta u_\alpha^{(n)}(j)$ is given by

$$\begin{aligned}\frac{\delta\Phi}{\delta u_\alpha^{(n)}(j)} &= \frac{\delta}{\delta u_\alpha^{(n)}(j)}\left(\frac{1}{N_\epsilon N_\nu}\sum_{p=1}^{N_\epsilon}\sum_{q=1}^{N_\nu}\phi'\left(\epsilon^{(p)},\nu_S^{(q)}\right)\right)\\ &= \frac{1}{N_\epsilon N_\nu}\sum_{p=1}^{N_\epsilon}\sum_{q=1}^{N_\nu}\frac{\delta\phi'\left(\epsilon^{(p)},\nu_S^{(q)}\right)}{\delta u_\alpha^{(n)}(j)}.\end{aligned} \tag{4.20}$$

Thus we need to average all gradients for all rf scaling factors $\epsilon^{(p)}$ and all offset frequencies $\nu_S^{(q)}$ of interests. The gradient $\delta\phi'(\epsilon,\nu_S)/\delta u_\alpha^{(n)}(j)$ for a specific scaling factor $\epsilon$ and a specific offset frequency $\nu_S$ is

$$\frac{\delta\phi'(\epsilon,\nu_S)}{\delta u_\alpha^{(n)}(j)} = \frac{\delta}{\delta u_\alpha^{(n)}(j)}\left(\frac{1}{N_{aq}+1}\sum_{k=0}^{N_{aq}}\left(1-(1-\overline{s_k}(\epsilon,\nu_S))^2\right)\right). \tag{4.21}$$

Now we are interested in the effect on the quality factor $\phi'(\epsilon,\nu_S)$ if the control amplitude $u_x^{(n)}(j)$ or $u_y^{(n)}(j)$ is varied in the $j$th time slice, i.e. between the time points $t_{j-1}$ and $t_j$. This time slice lies between the acquisition points $T_l$ and $T_{l+1}$, where $\lfloor j/M \rfloor$ is the truncated value (also called floor function) of the ratio $j/M$, i.e. the number of complete intervals $\Delta T$ between the time points $t_0$ and $t_j$. The controls $u_x^{(n)}(j)$ and $u_y^{(n)}(j)$ only have an effect on the detected signal $s_k$ for $k > l = \lfloor j/M \rfloor$. Hence we find

$$\begin{aligned}\frac{\delta\phi'(\epsilon,\nu_S)}{\delta u_\alpha^{(n)}(j)} &= \frac{\delta}{\delta u_\alpha^{(n)}(j)}\left(\frac{1}{N_{aq}+1}\sum_{k>l}\left(1-(1-\overline{s_k}(\epsilon,\nu_S))^2\right)\right)\\ &= \frac{-2}{N_{aq}+1}\sum_{k>l}(1-\overline{s_k}(\epsilon,\nu_S))\left(\frac{\delta\,\overline{s_k}(\epsilon,\nu_S)}{\delta u_\alpha^{(n)}(j)}\right).\end{aligned} \tag{4.22}$$

Using our simplified relaxation model (Eq. 4.14) for $\delta\,\overline{s_k}(\epsilon,\nu_S)/\delta u_\alpha^{(n)}(j)$ we find

$$\begin{aligned}\frac{\delta\,\overline{s_k}(\epsilon,\nu_S)}{\delta u_\alpha^{(n)}(j)} &= \exp\{-\kappa T_k\}\,\frac{\delta\langle I_x|\overline{\rho}\,(T_k)\rangle}{\delta u_\alpha^{(n)}(j)}\\ &= \frac{1}{N}\exp\{-\kappa T_k\}\,\frac{\delta\langle I_x|\widetilde{\rho}^{\,(n)}(T_k)\rangle}{\delta u_\alpha^{(n)}(j)}.\end{aligned} \tag{4.23}$$

The density operator at the acquisition time $T_k$ of the $n$th scan can be calculated by propagation of the initial density operator which is $\rho^{(n)}(t_0) = I_x$ for all $N$ COOP decoupling sequences. Thus we can write

$$\begin{aligned}
\frac{\delta\langle I_x|\widetilde{\rho}^{(n)}(T_k)\rangle}{\delta u_\alpha^{(n)}(j)} &= \frac{\delta}{\delta u_\alpha^{(n)}(j)}\langle I_x|U_k^{(n)}...\,U_j^{(n)}...\,U_1^{(n)}\rho(t_0)U_1^{(n)\dagger}...\,U_j^{(n)\dagger}...\,U_k^{(n)\dagger}\rangle \\
&= \frac{\delta}{\delta u_\alpha^{(n)}(j)}\mathrm{tr}\left\{I_x U_k^{(n)}...\,U_j^{(n)}...\,U_1^{(n)}\rho(t_0)U_1^{(n)\dagger}...\,U_j^{(n)\dagger}...\,U_k^{(n)\dagger}\right\} \\
&= \mathrm{tr}\{I_x U_k^{(n)}...\,\frac{\delta U_j^{(n)}}{\delta u_\alpha^{(n)}(j)}...\,U_1^{(n)}\rho(t_0)U_1^{(n)\dagger}...\,U_j^{(n)\dagger}...\,U_k^{(n)\dagger} \\
&\qquad + I_x U_k^{(n)}...\,U_j^{(n)}...\,U_1^{(n)}\rho(t_0)U_1^{(n)\dagger}...\,\frac{\delta U_j^{(n)\dagger}}{\delta u_\alpha^{(n)}(j)}...\,U_k^{(n)\dagger}\}.
\end{aligned} \tag{4.24}$$

where we used Eq. 4.10 and took advantage of $I_x$ being Hermitian (i.e. $I_x = I_x^\dagger$) in the second line and in the third line we applied the product rule. Using Eq. 4.16 the propagator $U_j^{(n)}$ can be written as

$$U_j^{(n)} = \exp\{-i\Delta t\,\mathcal{H}'^{(n)}(t_j)\} \tag{4.25}$$

with

$$\mathcal{H}'^{(n)}(t_j) = \mathcal{H}'(t) = \mathcal{H}^S_{off} + \mathcal{H}^{IS}_J + 2\pi\epsilon\,\{u_x^{(n)}(j)\,S_x + u_y^{(n)}(j)\,S_y\} \tag{4.26}$$

where $u_x^{(n)}(j)$ and $u_y^{(n)}(j)$ are the controls of the $n$th COOP decoupling sequence at the $j$th time slice. In the limit where $\Delta t \ll ||\mathcal{H}'^{(n)}(t_j)||^{-1}$ [11,77] we obtain to first order in $t$

$$\frac{\delta U_j^{(n)}}{\delta u_\alpha^{(n)}(j)} = -i\,2\pi\Delta t\;S_\alpha\,U_j^{(n)} \tag{4.27}$$

and

$$\frac{\delta U_j^{(n)\dagger}}{\delta u_\alpha^{(n)}(j)} = i\,2\pi\Delta t\;U_j^{(n)\dagger}\,S_\alpha. \tag{4.28}$$

Plugging this result into equation 4.24 we can write

$$
\begin{aligned}
&\frac{\delta\langle I_x|\widetilde{\rho}^{\,(n)}(T_k)\rangle}{\delta u_\alpha^{(n)}(j)} = \\
&= \quad -i\,2\pi\Delta t\ \mathrm{tr}\{I_x U_k^{(n)} ...\ S_\alpha\ U_j^{(n)} ...\ U_1^{(n)} \rho(t_0)\, U_1^{(n)\dagger} ...\ U_k^{(n)\dagger} \\
&\qquad -I_x U_k^{(n)} ...\ U_1^{(n)} \rho(t_0)\, U_1^{(n)\dagger} ...\ U_j^{(n)\dagger}\ S_\alpha\ ...\ U_k^{(n)\dagger}\} \\
&= \quad -i\,2\pi\Delta t \\
&\qquad \times \mathrm{tr}\{\underbrace{U_{j+1}^{(n)\dagger} ...\ U_k^{(n)\dagger} I_x U_k^{(n)} ...\ U_{j+1}^{(n)}}_{\widetilde{\lambda}_k^{(n)}(t_j)}\ S_\alpha\ \underbrace{U_j^{(n)} ...\ U_1^{(n)} \rho(t_0) U_1^{(n)\dagger} ...\ U_j^{(n)\dagger}}_{\widetilde{\rho}^{\,(n)}(t_j)} \\
&\qquad - \underbrace{U_{j+1}^{(n)\dagger}\ ...\ U_k^{(n)\dagger} I_x U_k^{(n)}\ ...\ U_{j+1}^{(n)}}_{\widetilde{\lambda}_k^{(n)}(t_j)} \underbrace{U_j^{(n)} ...\ U_1^{(n)} \rho(t_0) U_1^{(n)\dagger} ...\ U_j^{(n)\dagger}}_{\widetilde{\rho}^{\,(n)}(t_j)}\ S_\alpha\} \\
&= \quad -i\,2\pi\Delta t\ \mathrm{tr}\{\widetilde{\lambda}_k^{(n)}(t_j)\ S_\alpha\ \widetilde{\rho}^{\,(n)}(t_j) - \widetilde{\rho}^{\,(n)}(t_j)\ S_\alpha\ \widetilde{\lambda}_k^{(n)}(t_j)\} \\
&= \quad -i\,2\pi\Delta t\ \langle S_\alpha\,|\,[\widetilde{\rho}^{\,(n)}(t_j),\ \widetilde{\lambda}_k^{(n)}(t_j)]\rangle. \qquad (4.29)
\end{aligned}
$$

Hence we can write the gradient of the quality function $\delta\phi'(\epsilon,\nu_S)/\delta u_\alpha^{(n)}(j)$ to first order in $\Delta t$ as

$$
\begin{aligned}
\frac{\delta\phi'(\epsilon,\nu_S)}{\delta u_\alpha^{(n)}(j)} &= i\,2\pi\Delta t\ \frac{1}{N_{aq}+1}\ \frac{2}{N}\ \sum_{k>l} \exp\{-\kappa T_k\} \\
&\qquad \times (1-\overline{s_k}(\epsilon,\nu_S))\ \langle S_\alpha\,|\,[\,\widetilde{\rho}^{\,(n)}(t_j),\ \widetilde{\lambda}_k^{(n)}(t_j)\,]\rangle
\end{aligned} \qquad (4.30)
$$

We can refine this result by replacing $\widetilde{\lambda}_k^{(n)}(t_j)$ with $\lambda'^{(n)}_k(t_j)$ which is

$$
\lambda'^{(n)}_k(t_j) = \frac{2}{N}\,(1-\overline{s_k}(\epsilon,\nu_S))\,\widetilde{\lambda}_k^{(n)}(t_j) \qquad (4.31)
$$

and we obtain

$$
\begin{aligned}
\frac{\delta\phi'(\epsilon,\nu_S)}{\delta u_\alpha^{(n)}(j)} &= i\,2\pi\Delta t\ \frac{1}{N_{aq}+1} \\
&\qquad \times \sum_{k>l} \exp\{-\kappa T_k\}\ \langle\, S_\alpha\,|\,[\,\widetilde{\rho}^{\,(n)}(t_j),\ \lambda'^{(n)}_k(t_j)\,]\,\rangle \qquad (4.32) \\
&= i\,2\pi\Delta t\ \frac{1}{N_{aq}+1}\ \langle\, S_\alpha\,|\,[\,\widetilde{\rho}^{\,(n)}(t_j),\ \Lambda_k^{(n)}(t_j)\,]\,\rangle
\end{aligned}
$$

so that we are now able to calculate the gradients $\delta\Phi/\delta u_\alpha^{(n)}(j)$ (Eq. 4.13). The operator $\Lambda^{(n)}(t_j)$ is defined as

$$\Lambda^{(n)}(t_j) = \sum_{k>l} \exp\{-\kappa T_k\}\ \lambda_k'^{(n)}(t_j) \tag{4.33}$$

and can efficiently be calculated in complete analogy to the method presented in Appendix 3 of [44]. For each of the $N$ members of the COOP cycle, the density operator at time point $t_j$ is obtained by unitarily evolving the initial density operator $\rho^{(1)}(t_0) = \rho^{(2)}(t_0) = \ldots = \rho^{(N)}(t_0) = I_x$ forward in time (Eq. 4.15). We call

$$\lambda_k'^{(n)}(t_j) = U_{j+1}^{(n)\dagger} \ldots U_{kM}^{(n)\dagger}\ \lambda'(T_k)\ U_{km}^{(n)} \ldots U_{k+1}^{(n)} \tag{4.34}$$

the $k$th costate of the $n$th COOP decoupling sequence at time point $t_j$ that is obtained by unitarily evolving $\lambda'^{(n)}(T_k)$ backward in time where $\lambda'^{(n)}(T_k)$ is defined as

$$\lambda_k'^{(n)}(T_k) = \frac{2}{N}\left(1 - \langle I_x|\overline{\rho}(\epsilon, \nu_S, T_k)\rangle\right) I_x, \tag{4.35}$$

which is independent of $n$, i.e. at the same acquisition time $T_k$ all $N$ costates are identical ($\lambda'^{(1)}(T_k) = \lambda'^{(2)}(T_k) = \ldots = \lambda^{(N)}(T_k)$) and depend on the average expectation value $\overline{\langle I_x\rangle} = \langle I_x|\overline{\rho}(\epsilon, \nu_S, T_k)\rangle$. However, the back propagation of the costates under the different decoupling sequences results in different trajectories $\lambda_k'^{(n)}(t_j)$ for $1 \le j \le N_{aq}M$. If, instead of $\phi'(\epsilon, \nu_S)$, we choose $\phi(\epsilon, \nu_S)$ (Eq. 4.11) as a quality factor the corresponding costate is

$$\lambda_k^{(n)}(T_k) = \frac{1}{N}\ I_x. \tag{4.36}$$

The costate $\lambda_k^{(n)}(T_k)$ is independent of the average expectation value $\overline{\langle I_x\rangle} = \langle I_x|\overline{\rho}(\epsilon, \nu_S, T_k)\rangle$ and does not contain any information from the other members of the COOP decoupling sequence cycle. Hence, an optimization where $\phi(\epsilon, \nu_S)$ is employed as the quality factor, can not take advantage from the COOP pulse principle and equals to a parallel optimization of $N$ stand-alone decoupling sequences.

By following the gradients $\delta\Phi/\delta u_\alpha^{(n)}(j)$, i.e.

$$u_\alpha^{(n)}(j) \rightarrow u_\alpha^{(n)}(j) + \varepsilon\ \frac{\delta\Phi}{\delta u_\alpha^{(n)}} \tag{4.37}$$

where $\varepsilon$ is a variable step size, we are able to create a set of controls with improved performance $\Phi$. This is taken as the basis of a generalized version of the GRAPE algorithm [11] which combines the advantages of both optimal tracking [44] and the cooperative pulse approach (cf. Chapter 2 and [49]) which can be applied to the problem of efficient heteronuclear decoupling with minimized side-bands and uniform amplitude of the decoupled signal.

### Summary of the cooperative tracking algorithm

For the case of uniform relaxation rates $\kappa$ considered here, the basic cooperative GRAPE tracking algorithm can be summarized as follows:

1. Guess initial controls $u_x^{(n)}(j)$ and $u_y^{(n)}(j)$ for $1 \leq j \leq N_{aq}M$ and $1 \leq n \leq N$.
2. Starting from $\rho^{(1)}(t_0) = \rho^{(2)}(t_0) = \ldots = \rho^{(N)}(t_0) = I_x$ calculate all $\widetilde{\rho}^{(n)}(t_j)$ for $1 \leq j \leq N_{aq}M$ and $1 \leq n \leq N$ using Eq. 4.15.
3. Starting from $\Lambda^{(1)}(T_{N_{aq}}) = \Lambda^{(2)}(T_{N_{aq}}) = \ldots = \Lambda^{(N)}(T_{N_{aq}}) = (2/N) \times (1 - \langle I_x|\overline{\rho}(\epsilon, \nu_S, T_k)\rangle)\, I_x$ calculate all $\Lambda^{(n)}(t_j)$ for $1 \leq j \leq N_{aq}M$ and $1 \leq n \leq N$ using Eqs. 4.33–4.35.
4. Calculate $\delta\phi(\epsilon^{(p)}, \nu_S^{(q)})/\delta u_\alpha^{(n)}(j)$ for $1 \leq j \leq N_{aq}M$ and $1 \leq n \leq N$ using Eq. 4.32.
5. Repeat steps 2–4 for all rf scaling factors $\epsilon^{(p)}$ and offsets $\nu_S^{(q)}$ and calculate $\delta\Phi/\delta u_x^{(n)}(j)$ and $\delta\Phi/\delta u_y^{(n)}(j)$ for $0 \leq j \leq N_{aq}M$ and $0 \leq n \leq N$ using Eq. 4.20.
6. Update the $2N_{aq}MN$ control amplitudes $u_x^{(n)}(j)$ and $u_y^{(n)}(j)$ according to Eq. 4.37.
7. With these as the new controls, go to step 2.

The algorithm is terminated if a certain convergence criterion is fulfilled. For faster convergence, the gradient information (Eq. 4.20) can be used in more general optimizing algorithms such as conjugate gradients or quasi-Newton methods like limited-memory BFGS [35,54]. The rf power of the decoupling sequence can be minimized or fixed as described in [11, 14]. The maximum rf amplitude $u_{max}$ can be limited by resetting the amplitude to the maximum amplitude if it is exceeded after step 6 [11, 19].

In addition, it is possible to describe the system with a reduced four-dimensional state vector [44,78–80] which minimizes the computational effort. Cooperative tracking is not limited to the simplified relaxation model which we used here. For example, the system of interest can also be described using a full relaxation matrix approach. In addition, cooperative tracking is not restricted to the optimization of decoupling sequences but the present algorithm could in principle be used for the optimization of various pulse sequences.

In order to be able to take rf field inhomogeneity and miscalibration into account, we derived gradients for the scaled controls $u_\alpha^{(n)}(j) = \epsilon u_x^{(n)}(j)$ and $\epsilon u_y^{(n)}(j)$. Thus, we do not optimize a single set of controls $u_x^{(n)}(j)$ and $u_y^{(n)}(j)$ but a distribution of control sets discretized by $\epsilon$. In [44] the gradients were derived for $u'^{(n)}_\alpha(j) = u_x^{(n)}(j)$ and $u_y^{(n)}(j)$ no matter which value is taken by $\epsilon$. In the context of cooperative tracking an according derivation would lead to the modified gradient

$$\frac{\delta\phi''(\epsilon,\nu_S)}{\delta u_\alpha^{(n)}(j)} = i\,2\pi\epsilon\Delta t\,\frac{1}{N_{aq}+1}\,\langle\, S_\alpha\,|\,[\,\widetilde{\rho}^{\,(n)}(t_j),\;\Lambda_k^{(n)}(t_j)\,]\,\rangle, \tag{4.38}$$

which differs from Eq. 4.32 by a factor $\epsilon$. By the principle of reciprocity [81] the detection sensitivity is proportional to $\epsilon$ which represents a physical justification for a scaling of the gradients according to Eq. 4.38. However, the transmitter and receiver coils are not identical in general and especially not for the case of heteronuclear decoupling. If the deviations of $\epsilon$ from 1 are small the difference between the gradients from Eqs. 4.32 and 4.38 are probably negligible. However, for larger inhomogeneities [17] different convergence properties might be observable for the two different gradients. All pulses presented in this thesis where rf inhomogeneity was taken into account, were optimized using gradients in analogy to Eq. 4.32 where the gradient is not scaled by $\epsilon$. It remains an open question if one of the two methods is to be preferred in general.

We expect our new algorithm to be especially interesting for $^{13}$C-detected quantitative NMR where uniform signal amplitudes and minimized sidebands are desired for the considered offset frequency range [70]. Existing decoupling techniques either reduce decoupling sidebands in several scans or create a uniform decoupling profile in a single scan. Optimal tracking [44] has lead to excellent low-power decoupling sequences. With cooperative tracking, where we applied the cooperative pulse approach to optimal tracking, we provide a method that is in principle capable of creating decoupling sequence cycles that both have a highly uniform offset profile and, at a time, minimize decoupling sidebands.

# References

[1] R. R. Ernst, Application of Fourier transform spectroscopy to magnetic resonance, Rev. Sci. Instrum. 37 (1966) 93–102.

[2] M. H. Levitt, R. Freeman, NMR population inversion using a composite pulse, J. Magn. Reson. 33 (1979) 473–476.

[3] R. Freeman, S. Kempsell, M. Levitt, Radiofrequency pulse sequences which compensate their own imperfections, J. Magn. Reson 38 (1980) 453–479.

[4] M. H. Levitt, Composite pulses, Prog. Nucl. Magn. Reson. Spectrosc. 18 (1986) 61–122.

[5] M. H. Levitt, Encyclopedia of Nuclear Magnetic Resonance, Wiley, 1996, Ch. Composite pulses, pp. 1396–1411.

[6] W. S. Warren, M. S. Silver, The art of pulse crafting: applications to magnetic resonance and laser spectroscopy, Adv. Magn. Reson. 12 (1988) 247–384.

[7] R. Freeman, Shaped radiofrequency pulses in high resolution NMR, Prog. Nucl. Magn. Reson. Spectrosc. 32 (1998) 59–106.

[8] J.-M. Bohlen, M. Rey, G. Bodenhausen, Refocusing with chirped pulses for broadband excitation without phase dispersion, J. Magn. Reson. 84 (1989) 191 – 197.

[9] E. Kupče, Applications of adiabatic pulses in biomolecular nuclear magnetic resonance, in: Nuclear magnetic resonance of biological macromolecules, Vol. 338 of Methods in enzymology, Academic Press Inc., 2001, pp. 82–111.

[10] A. Bryson Jr., Y.-C. Ho, Applied optimal control, Hemisphere, Washington, D.C., 1975.

[11] N. Khaneja, T. Reiss, C. T. Kehlet, T. Schulte-Herbrüggen, S. J. Glaser, Optimal control of coupled spin dynamics: Design of NMR pulse sequences by gradient ascent algorithms, J. Magn. Reson. 172 (2005) 296–305.

[12] T. E. Skinner, personal communication.

[13] K. Kobzar, T. E. Skinner, N. Khaneja, S. J. Glaser, B. Luy, Exploring the limits of broadband excitation and inversion pulses, J. Magn. Reson. 170 (2004) 236–243.

[14] K. Kobzar, T. E. Skinner, N. Khaneja, S. J. Glaser, B. Luy, Exploring the limits of excitation and inversion pulses II. RF-power optimized pulses, J. Magn. Reson. 194 (2008) 58–66.

[15] J. L. Neves, B. Heitmann, T. O. Reiss, H. Schor, N. Khaneja, S. J. Glaser, Exploring the limits of polarization transfer efficiency in homonuclear three spin systems, J. Magn. Reson. 181 (2006) 126–134.

[16] T. E. Skinner, T. O. Reiss, B. Luy, N. Khaneja, S. J. Glaser, Application of optimal control theory to the design of broadband excitation pulses for high resolution NMR, J. Magn. Reson. 163 (2003) 8–15.

[17] T. E. Skinner, M. Braun, K. Woelk, N. I. Gershenzon, S. J. Glaser, Design and application of robust rf pulses for toroid cavity NMR spectroscopy, J. Magn. Reson. 209 (2011) 282–290.

[18] T. E. Skinner, K. Kobzar, B. Luy, R. Bendall, W. Bermel, N. Khaneja, S. J. Glaser, Optimal control design of constant amplitude phase-modulated pulses: Application to calibration-free broadband excitation, J. Magn. Reson. 179 (2006) 241–249.

[19] T. E. Skinner, T. O. Reiss, B. Luy, N. Khaneja, S. J. Glaser, Reducing the duration of broadband excitation pulses using optimal control with limited rf amplitude, J. Magn. Reson. 167 (2004) 68–74.

[20] T. E. Skinner, T. O. Reiss, B. Luy, N. Khaneja, S. J. Glaser, Tailoring the optimal control cost function to a desired output: Application to minimizing phase errors in short broadband excitation pulses, J. Magn. Reson. 172 (2005) 17–23.

[21] N. I. Gershenzon, T. E. Skinner, B. Brutscher, N. Khaneja, M. Nimbalkar, B. Luy, S. J. Glaser, Linear phase slope in pulse design: application to coherence transfer, J. Magn. Reson. 192 (2008) 335–343.

[22] N. I. Gershenzon, K. Kobzar, B. Luy, S. J. Glaser, T. E. Skinner, Optimal control design of excitation pulses that accomodate relaxation, J. Magn. Reson. 188 (2007) 330–336.

[23] B. Luy, K. Kobzar, T. E. Skinner, N. Khaneja, S. J. Glaser, Construction of universal rotations from point-to-point transformations, J. Magn. Reson. 176 (2005) 179–186.

[24] K. Kobzar, B. Luy, N. Khaneja, S. J. Glaser, Pattern pulses: Design of arbitrary excitation profiles as a function of pulse amplitude and offset, J. Magn. Reson. 173 (2005) 229–235.

[25] Topspin release January 2010.

[26] K. Kobzar, Optimal control, partial alignment and more: the design of novel tools for NMR spectroscopy of small molecules, Ph.D. thesis, Technische Universität München, Department Chemie (2007).

[27] C. T. Kehlet, A. C. Sivertsen, M. Bjerring, T. O. Reiss, N. Khaneja, S. J. Glaser, N. C. Nielsen, Improving solid-state NMR dipolar recoupling by optimal control, J. Am. Chem. Soc. 126 (2004) 10202–10203.

[28] C. T. Kehlet, T. V. Vosegaard, N. Khaneja, S. J. Glaser, N. C. Nielsen, Low-power homonuclear dipolar recoupling in solid-state NMR developed using optimal control theory, Chem. Phys. Lett. 414 (2005) 204–209.

[29] Z. Tošner, S. J. Glaser, N. Khaneja, N. C. Nielsen, Effective hamiltonians by optimal control: solid-state NMR double-quantum planar and isotropic dipolar recoupling, Chem. Phys. 125 (2006) 184502/1–10.

[30] G. B. Matson, K. Young, L. G. Kaiser, RF pulses for *in vivo* spectroscopy at high field designed under conditions of limited power using optimal control, J. Magn. Reson. 199 (2009) 30–40.

[31] T. Schulte-Herbrüggen, A. K. Spörl, R. Marx, N. Khaneja, J. M. Myers, A. F. Fahmy, S. J. Glaser, Quantum computing implemented via optimal control: theory and application to spin- and pseudo-spin systems, Lectures on quantum information, Wiley-VCH, 2006, pp. 481–501.

[32] M. A. Janich, R. F. Schulte, M. Schwaiger, S. J. Glaser, Robust slice-selective broadband refocusing pulses, submitted to J. Magn. Reson.

[33] P. de Fouquieres, S. Schirmer, S. Glaser, I. Kuprov, Second order gradient ascent pulse engineering, e-print: arXiv:1102.4096v2 [quant-ph].

[34] S. Machnes, U. Sander, S. Glaser, P. de Fouquieres, A. Gruslys, S. Schirmer, T. Schulte-Herbrüggen, Comparing, optimising and benchmarking quantum control algorithms in a unifying programming framework, e-print: arXiv:1011.4874v3 [quant-ph].

[35] R. Fletcher, Practical methods of optimization, Wiley, 1987.

[36] I. I. Maximov, Z. Tošner, N. C. Nielsen, Optimal control design of NMR and dynamic nuclear polarization experiments using monotonically convergent algorithms, J. Chem. Phys. 128 (2008) 184505.

[37] M. Lapert, Y. Zhang, M. Braun, S. J. Glaser, D. Sugny, Singular extremals for the time-optimal control of dissipative spin ½ particles, Phys. Rev. Lett. 104 (2010) 083001.

[38] E. Assémat, M. Lapert, Y. Zhang, M. Braun, S. J. Glaser, D. Sugny, Simultaneous time-optimal control of the inversion of two spin ½ particles, Phys. Rev. A 82 (2010) 013415.

[39] M. Lapert, Y. Zhang, M. Braun, S. J. Glaser, D. Sugny, Geometric versus numerical optimal control of a dissipative spin ½ particle, Phys. Rev. A 82 (2010) 063418.

[40] Y. Zhang, M. Lapert, D. Sugny, M. Braun, S. J. Glaser, Time-optimal control of spin ½ particles in the presence of radiation damping and relaxation, J. Chem. Phys. 134 (2011) 054103.

[41] F. Mintert, M. Lapert, Y. Zhang, S. J. Glaser, D. Sugny, Saturation of a spin ½ particle by generalized local control, J. Chem. Phys. 148 (2011) 073001.

[42] M. Lapert, Y. Zhang, S. J. Glaser, D. Sugny, Towards the time-optimal control of dissipative spin ½ particles in nuclear magnetic resonance, J. Phys. B 44 (2011) 154014.

[43] T. E. Skinner, M. Nimbalkar, S. J. Glaser, Fantastic four: plug and play pulses, under preparation.

[44] J. L. Neves, B. Heitmann, N. Khaneja, S. J. Glaser, Heteronuclear decoupling by optimal tracking, J. Magn. Reson. 201 (2009) 7–17.

[45] J. Keeler, Understanding NMR Spectroscopy, Wiley, Chichester, 200.

[46] G. Bodenhausen, H. Kogler, R. R. Ernst, Selection of coherence-transfer pathways in NMR pulse experiments, J. Magn. Reson. 58 (1984) 370–388.

[47] A. D. Bain, Coherence levels and coherence pathways in NMR, A simple way to design phase cycling procedures, J. Magn. Reson. 56 (1984) 418–427.

[48] M. H. Levitt, P. K. Madhu, C. E. Hughes, Cogwheel phase cycling, J. Magn. Reson. 155 (2002) 300–306.

[49] M. Braun, S. Glaser, Cooperative pulses, J. Magn. Reson. 207 (2010) 114–123.

[50] W. P. Aue, E. Bartholdi, R. R. Ernst, Two-dimensional spectroscopy. Application to nuclear magnetic resonance, J. Chem. Phys 64 (1976) 2229–2246.

[51] J. Jeener, B. H. Meier, P. Bachmann, R. R. Ernst, Investigation of exchange processes by two-dimensional NMR spectroscopy, J. Chem. Phys 71 (1979) 4546–4553.

[52] G. A. Morris, R. Freeman, Enhancement of nuclear magnetic resonance signals by polarization transfer, J. Am. Chem. Soc. 101 (1979) 760–762.

[53] N. F. Ramsey, Molecular beams, Clarendon Press, Oxford, 1956.

[54] A. Wächter, L. T. Biegler, On the implementation of a primal-dual interior point filter line search algorithm for large-scale nonlinear programming, Math. Program. Ser. A 106 (2006) 25–57.

[55] Z. Tošner, T. Vosegaard, C. T. Kehlet, N. Khaneja, S. J. Glaser, N. C. Nielsen, Optimal control in NMR spectroscopy: Numerical implementation in SIMPSON, J. Magn. Reson. 197 (2009) 120–134.

[56] S. Conolly, D. Nishimura, A. Macovski, Optimal control solutions to the magnetic resonance selective excitation problem, IEEE Trans. Med. Imag. MI-5 (1986) 106115.

[57] R. J. Ogg, P. B. Kingsley, J. S. Taylor, WET, a $T_1$- and $B_1$-insensitive water-suppression method for *in vivo* localized $^1$H NMR spectroscopy, J. Magn. Reson. B 104 (1994) 1–10.

[58] S. Zhang, X. Yang, D. G. Gorenstein, Enhanced suppression of residual water in a "270" WET sequence, J. Magn. Reson. 143 (2000) 382–386.

[59] A. Bax, A spatially selective composite 90° radiofrequencey pulse, J. Magn. Reson. 64 (1985) 142–145.

[60] J.-Y. Park, M. Garwood, Spin-echo MRI using $\pi/2$ and $\pi$ hyperbolic secant pulses, Magn. Reson. Med. 61 (2009) 175–187.

[61] T.-L. Hwang, A. J. Shaka, Water suppression that works. Excitation sculpting using arbirtrary waveforms and pulsed field gradients, J. Magn. Reson. A 112 (1995) 275–279.

[62] B. Adams, HSQC pulse sequences for $^{19}$F, Magn. Reson. Chem. 46 (2008) 377–380.

[63] I. Bertini, I. C. Felli, R. Kümmerle, D. Moskau, R. Pietrattelli, $^{13}$C–$^{13}$C NOESY: An attractive alternative for studying large macromolecules, J. Am. Chem. Soc. 126 (2004) 464–465.

[64] W. Bermel, I. Bertini, I. C. Felli, R. Kümmerle, R. Pietrattelli, $^{13}$C direct detection experiments on the paramagnetic oxidized monomeric copper, zinc superoxide dismutase, J. Am. Chem. Soc. 125 (2003) 16423–16429.

[65] P. Qrtiz, E. Reguera, J. Fernández-Bertrán, Study of the interaction of KF with carbohydrates in DMSO-$d_6$ by $^1$H and $^{13}$C NMR spectroscopy, J. Fluorine Chem. 113 (2002) 7–12.

[66] M. J. Thrippleton, J. Keeler, Elimination of zero-quantum interference in two-dimensional NMR spectra, Angew. Chem. Int. Ed. 42 (2003) 3938–3941.

[67] R. R. Ernst, G. Bodenhausen, A. Wokaun, Principles of nuclear magnetic resonance in one and two dimensions, Clarendon Press, Oxford, 1987.

[68] R. Freeman, H. D. W. Hill, High-resolution study of NMR spin echoes: J-spectra, J. Chem. Phys. 54 (1971) 301–313.

[69] G. Bodenhausen, R. Freeman, D. Turner, Two-dimensional J-spectroscopy: proton-coupled carbon-13 NMR, J. Chem. Phys. 65 (1976) 839–840.

[70] E. Tenailleau, S. Akoka, Adiabatic $^1$H decoupling scheme for very accurate intensity measurements in $^{13}$C NMR, J. Magn. Reson. 185 (2007) 50–58.

[71] U. Eggenberger, P. Schmidt, M. Sattler, S. J. Glaser, C. Griesinger, Frequency-selective decoupling with recursively expanded soft pulses in multinuclear NMR, J. Magn. Reson. 100 (1992) 604–610.

[72] E. R. P. Zuiderweg, S. W. Fesik, Band-selective heteronuclear decoupling using shaped pulses as an aid in measuring long-range heteronuclear coupling constants, J. Magn. Reson. 93 (1991) 653–658.

[73] C. R. R. Grace, R. Riek, Pseudomultidimensional NMR by spin-state selective off-resonance decoupling, J. Am. Chem. Soc. 125 (2003) 16104–16113.

[74] E. Kupče, R. Freeman, A two-dimensional experiment that separates decoupling sidebands from the main peaks, J. Magn. Reson. 151 (2001) 142–145.

[75] E. Kupče, R. Freeman, G. Wider, K. Wüthrich, Suppression of cycling sidebands using bi-level adiabatic decoupling, J. Magn. Reson. A 122 (1996) 81–84.

[76] Z. Zhou, R. Kümmerle, X. Qiu, D. Redwine, R. Cong, A. Taha, D. Baugh, B. Winniford, A new decoupling method for accurate quantification of polyethylene copolymer composition and triad sequence distribution with $^{13}$C NMR, J. Magn. Reson. 187 (2007) 225–233.

[77] R. Fisher, Optimal control of multi-level quantum systems, Ph.D. thesis, Technische Universität München, Department Chemie (2010).

[78] T. E. Skinner, M. R. Bendall, Exact product operator evolution of weakly coupled spin ½ $I_mS_n$ systems during arbitrary rf irradiation of the I spins, J. Magn. Reson. 141 (1999) 271–285.

[79] M. R. Bendall, T. E. Skinner, Comparison and use of vector and quantum descriptions of $J$ coupled spin evolution during rf irradiation of one spin in an IS spin system, J. Magn. Reson. 143 (2000) 329–351.

[80] T. E. Skinner, M. R. Bendall, $J$-coupling and chemical shift evolution during I-spin irradiation of $I_mS_n$ spin systems: product operator solutions and applications, Conc. Magn. Reson. 14 (2002) 287–307.

[81] D. I. Hoult, R. E. Richards, The signal-to-noise ratio of the nuclear magnetic resonance experiment, J. Magn. Reson. 24 (1976) 71–85.